10-22-2020 2:00 PM

Analytical and Computational Modelling of the Ranque-Hilsch Vortex Tube

Nolan J. Dyck, *The University of Western Ontario*

Supervisor: Straatman, Anthony G., *The University of Western Ontario*

A thesis submitted in partial fulfillment of the requirements for the Doctor of Philosophy degree in Mechanical and Materials Engineering

Abstract

The Ranque-Hilsch vortex tube (RHVT) is a simple mechanical device with no moving parts capable of separating a supply of compressed fluid into hot and cold streams through a process called temperature separation. The overall aim is to develop models which can be used to assess the temperature separation mechanisms in the RHVT, leading to a better overall understanding of the underlying physics. The introductory chapter contains a thermodynamic analysis and introduction to the flow physics, alongside three miniature literature reviews and critiques identifying research gaps.

The body of the thesis contains three articles. The first article studies the flow of a perfect, inviscid gas through a duct, which rotates about an axis perpendicular to the direction of the duct. The analysis shows that gas flowing towards the center of rotation will cool while delivering energy to increase or maintain the angular momentum of the entire system. The study further generalizes the results to a duct with an arbitrarily varying cross-sectional area and arbitrary path through 3D space, yielding similar results.

In the second article, a new technique for obtaining exact solutions to the Navier-Stokes equations is developed, and many new solutions are presented; most notably, a new solution describing a flow strongly resembling flow inside the RHVT.

The third article contains three computational fluid dynamics studies of the RHVT; (1) testing the influence of different hydrodynamic boundary condition types and boundary condition locations on temperature separation, (2) examining the influence of four different turbulence models on temperature separation and energy transfer modes, and (3) examining the influence of the axisymmetric assumption using a novel method for computing the fluid injection angle. It was found that the assumptions made elsewhere in the literature are validated, although using mass-flow boundary conditions is preferred where possible, the choice of turbulence model strongly influences the temperature separation and the flow structure. The results herein indicate shear work transfer is the dominant energy transfer mechanism in the RHVT.

Keywords: Ranque-Hilsch vortex tube, vortex tube, energy separation, temperature separation, Navier-Stokes exact solutions, computational fluid dynamics, flow structure, vortex

Summary for Lay Audience

The Ranque-Hilsch Vortex Tube (RHVT) is a device that behaves in an unexpected way: if a source of compressed air (such as an air hose used to pressurize tires at a gas station) is attached to the inlet of this tube, the air going through it will swirl and form a vortex. The air exits the tube from two openings: cold air from the center of the vortex exhausts through a small hole at one end, and hot air exhausts from a circular gap at the other end of the tube. This process is called temperature separation. Many researchers have proposed theories explaining why temperature separation happens, but there is no consensus yet. This thesis contains three articles which help predict the flow patterns and temperatures inside the RHVT, which are used to test the popular temperature separation theories.

In the first article, a different, simpler problem is studied: a source of compressed air is attached to one end of a small tube, while the opposite end of the tube rotates about an axis. The analysis reveals the air moving down the tube towards the axis cools along the way, and the energy lost from cooling contributes to spinning the tube faster about its axis of rotation.

In the second article, the mathematical equations that describe fluid motion are solved using a new technique, and in one case, the flow pattern is similar to the flow inside the RHVT.

Finally, the last article describes three studies using computer simulations to model the air flow inside the RHVT. It was found that simulation results matched experimental results well when the amount of air going into and out of the tube was fixed, and that 2D simulation results are accurate when the angle of the flow entering the tube is determined using the results of a 3D simulation. In this last work, evidence is found to support the hypothesis that the cooling happens inside the RHVT because of friction between layers of air spinning at different speeds.

Acknowlegements

I thank God for his steadfastness and providence throughout these five years of work towards the completion of this thesis. It is my hope that this thesis would be a sweet offering to Him.

I want to express my sincere gratitude to my advisor, Dr. Anthony Straatman, for his patience and support throughout this process. Combined with his rich experience in the field of fluid mechanics, he has an invaluable ability to validate a student's ideas and, while treating them with the utmost respect, nudge them towards a realistic, actionable plan.

I want to thank my former and present lab mates, Dr. Furqan Khan, Dr. Mahmoud Elhalwagy, Chris Csernyei, Marc-Andre Brooks, Jeremy Voo, Peter Nielsen, and Rex Sherratt for many fruitful discussions, unfruitful discussions, help troubleshooting computer issues, and proofreading. I'd like to extend a special thank you to my colleague Mark Parker, who, in addition to these things, provided the set of experimental data which my thesis uses as a benchmark, and added his strong practical knowledge of physical experiments, from which my thesis benefits greatly.

I would also like to thank my parents and siblings for their love, encouragement, and support.

Finally, I would like to express my deep appreciation of my wife Beth, with whom I have enjoyed 2 fantastic years of marriage, for patiently listening to my musings on obscure topics in my sub-field, and supporting me in the completion of this journey.

Co-Authorship Statement

Two of the three chapters forming the body of this thesis have been published in peer-reviewed journals, while the third has been submitted for review. Their bibliographic references are provided here:

N. J. Dyck and A. G. Straatman, "Compressible and Choked Flows in Rotating Passages," *Open J. Fluid Dyn.*, vol. 09, no. 01, pp. 1–21, 2019.

N. J. Dyck and A. G. Straatman, "Exact Solutions to the Three-Dimensional Navier–Stokes Equations Using the Extended Beltrami Method," *J. Appl. Mech.*, vol. 87, no. 1, Jan. 2020.

N. J. Dyck, M. J. Parker, and A. G. Straatman, "The Impact of Boundary Condition and Model Parameters on CFD Simulations of the Ranque-Hilsch Vortex Tube," *Int. J. Heat Mass Transf.* Submission No. HMT-S-20-01797

In each case I developed the methodology, carried out the analyses, processed the data, and completed the writing, with the exception of the final work, wherein the description of the experimental procedure in chapter 4.2, the related content within the introduction, figures 4.2, 4.3, and 4.5 were provided by Mr. M. J. Parker. In each work Dr. A. G. Straatman provided guidance and scientific support.
All in all, I estimate that I have completed approximately 85% of the work in this thesis.

Contents

List of Figures

List of Tables

Chapter 1

Introduction

Few devices have generated as much intrigue as the Ranque-Hilsch Vortex Tube (RHVT). A device that requires nothing more than a supply of room-temperature compressed air, producing cold air from one end while exhausting hot air from the other might seem a laughable idea to an astute student of thermodynamics, who might use the Clausius statement[1] to argue that the device violates the second law of thermodynamics, and could not exist. And yet the RHVT *is* that device [2]. In addition to numerous laboratory experiments validating Ranque's nearly-century-old claims, it has been shown that the RHVT is not in violation of the second law of thermodynamics [3]. Somehow, a complete understanding of the phenomenon occurring inside the RHVT, called temperature separation, remains elusive. At the same time, several niche applications for the device have been found; including the cooling of electrical cabinets [4] and natural gas processing [5] among several others [6]. In this thesis I attempt to shed light on this underlying mechanism using a combination of analytical and computational techniques.

[1] Heat can never pass from a colder to a warmer body without some other change, connected therewith, occurring at the same time. [1]

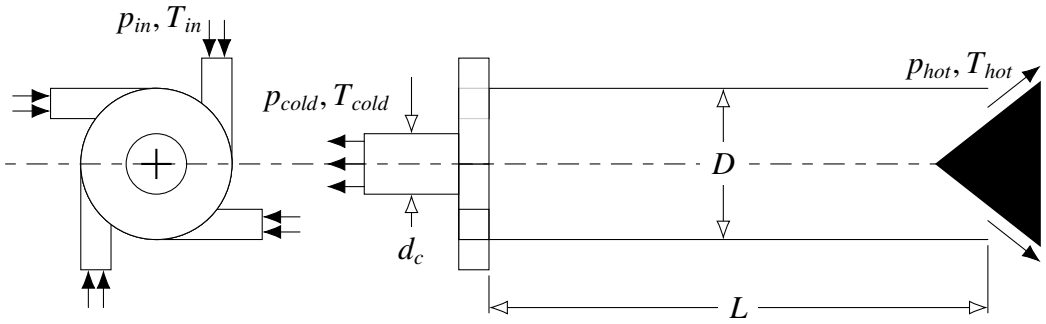

Figure 1.1: A schematic of a typical counter-flow Ranque-Hilsch Vortex Tube with four inlet nozzles. An end view is shown on the left and a cut-away of the tube is shown on the right. The filled triangle is the hot exit plug.

Figure 1.1 depicts a simple schematic of a RHVT (a name that is often shortened to 'Vortex Tube' or VT). A compressed fluid is supplied to the inlet channels, directing it in the circumferential direction. This configuration creates a strong vortex which extends along the length of the tube. The small hole near the inlet exhausts cold fluid, and is referred to as the cold exit, or cold outlet. Conversely, fluid leaving the annular opening at the opposite end of the tube is hot, and the opening is called the hot exit, or hot outlet.

Occasionally, researchers have studied the similar *co-flow* or parallel-flow vortex tube. The structure is similar to the schematic depicted in figure 1.1, except the hot exit plug has a concentric hole drilled which serves as the cold exit and the original cold exit is blocked. Only a handful of researchers have studied this device, including Comassar [7] and Lay [8], however Eiamsa-Ard and Promvonge [9] have noted in their review that temperature separation is much less pronounced than the counter-flow VT.

This chapter contains the necessary background information to understand the scientific contributions of chapters 2, 3, and 4. First, a 'black-box' analysis of the RHVT will be carried out using only a thermodynamic treatment of the tube, then the basic flow structure of the tube will be discussed in conjunction with the simplified models of Ranque-Hilsch flow presented in the literature, followed by a review of the prevalent temperature separation theories.

While the work in this thesis might first appear to be disparate, several different methodologies are used and the overall aim is to answer two central questions:

- What are the dominant mechanism(s) of temperature or energy separation in the RHVT?

- What are the necessary and sufficient conditions for temperature separation to occur?

1.1 Definitions of Temperature Separation and Energy Separation

In this thesis cold and hot exit temperature separation are formally defined as:

$$\Delta T_{0,\mathrm{c}} = T_{0,\mathrm{i}} - T_{0,\mathrm{c}} \tag{1.1}$$

$$\Delta T_{0,\mathrm{h}} = T_{0,\mathrm{h}} - T_{0,\mathrm{i}} \tag{1.2}$$

where the subscripts i, c, and h denote quantities at the inlet(s), cold, and hot boundaries, respectively. The symbol T_0 denotes a total temperature, which is the sum of the thermodynamic (static) temperature T, and another component capturing the local kinetic energy of the flow. This term is formally defined below for a perfect gas. Cold and hot exit energy separations have definitions similar to temperature separation:

$$\Delta E_{\mathrm{c}} = \dot{m}_{\mathrm{c}} \left(h_{0,\mathrm{i}} - h_{0,\mathrm{c}}\right) \tag{1.3}$$

$$\Delta E_{\mathrm{h}} = \dot{m}_{\mathrm{h}} \left(h_{0,\mathrm{h}} - h_{0,\mathrm{i}}\right) \tag{1.4}$$

where h_0 is the total enthalpy. These are the metrics which are most frequently used in evaluating the performance of the RHVT. Occasionally, papers will speak in terms of total temperature separation, defined as $T_{\mathrm{h}} - T_{\mathrm{c}}$ [10]. This characterization will be avoided in this thesis as it creates confusion when discussing the total temperature, and it has limited usefulness. In general, the term *vortex tube performance* refers to the magnitude of the cold exit energy separation, as the most common applications of the VT seek to harness the cold exit stream for cooling purposes.

1.2 A Black-Box Analysis of the Ranque-Hilsch Vortex Tube

In order to obtain an initial sense of the operation of the RHVT and explore possible energy separation mechanisms, it is useful to write shell-balances of mass, energy, and entropy; treating the RHVT as a black-box. The RHVT shown in figure 1.1 has four inlets (although any number is possible), an annular exit, and an axial exit at the opposite end. Typically, the inlet properties are the same across the inlet channels, and in the following analysis they are treated as a single inlet. In this section, the exit flows are assumed to be well-mixed, having uniform properties. The following mathematical derivation is common to many papers such as O'Connell [11], but the commentary is original. A natural starting point is the conservation of mass, which dictates that the in- and out-flow mass flow rates must balance.

$$\dot{m}_\mathrm{i} = \dot{m}_\mathrm{c} + \dot{m}_\mathrm{h} \tag{1.5}$$

Frequently, results are presented as a function of the cold mass fraction, or mass flow split, which is the ratio of the mass flow rate leaving the cold exit to the inlet mass flow rate $\lambda = \dot{m}_\mathrm{c}/\dot{m}_\mathrm{i}$. In experiments, the cold mass fraction has been manipulated by varying the position of the hot exit plug shown in figure 1.1 to change the hot exit area, adjusting valves downstream of either exit, or by adjusting the inlet pressure. In CFD studies, the outlet pressures are specified or a mass flow rate is fixed at one exit.

The energy balance is given by

$$\begin{aligned} \dot{m}_\mathrm{i}\left(h_\mathrm{i} + \frac{v_\mathrm{i}^2}{2}\right) &= \dot{m}_\mathrm{c}\left(h_\mathrm{c} + \frac{v_\mathrm{c}^2}{2}\right) + \dot{m}_\mathrm{h}\left(h_\mathrm{h} + \frac{v_\mathrm{h}^2}{2}\right) \\ \left(h_\mathrm{i} + \frac{v_\mathrm{i}^2}{2}\right) &= \lambda\left(h_\mathrm{c} + \frac{v_\mathrm{c}^2}{2}\right) + (1-\lambda)\left(h_\mathrm{h} + \frac{v_\mathrm{h}^2}{2}\right) \end{aligned} \tag{1.6}$$

where no work is exchanged with the surroundings, gravitational potential effects are neglected, and equation 1.5 has been used. The vortex tube walls are also assumed to be adiabatic, an assumption which must be justified using experimental observations. Thakare and Parekh [12] have run experiments using a commercial vortex tube whose outer wall was exposed to the laboratory environment, and then repeated the study with the same VT wrapped in glass wool

insulation. They found a significant increase in temperature separation when the tube was insulated. Promvonge and Eiamsa-ard [10] have also studied the effects of insulating the RHVT and found similar results. Ramakrishna et al. [13] tested the influence of changing the VT material, using PVC, Perspex®, mild steel, and copper tubes of the same dimensions. They found that the materials having low thermal conductivity (i.e. PVC and Perspex) yielded increased temperature separation. In addition, Ramakrishna et al. applied a layer of wax (low thermal conductivity) to the copper tube, and ran the tests again, finding temperature separations that matched very closely with the results of the PVC tube (without wax). This result suggests that axial conduction along the length of the tube does not influence temperature separation either. Given the evidence, I conclude that heat exchange with the environment degrades temperature separation, and is not necessary for temperature separation to occur.

We can also introduce the total enthalpy definition ($h_0 = h + v^2/2$) and reduce equation 1.6 to

$$\lambda = \frac{h_{0\mathrm{h}} - h_{0\mathrm{i}}}{h_{0\mathrm{h}} - h_{0\mathrm{c}}} \tag{1.7}$$

As indicated by O'Connell [11], equation 1.7 can serve as a check to validate the consistency of experimental measurements; for example, the mass flow split, λ, observed in an experiment can be verified by using known temperatures at the exits to solve the right-hand-side of the equation. However, recall the total enthalpy depends on the mass-flow-averaged kinetic energies at each of the exits ($v^2/2$), which in turn depend on the local densities and relative mass flow rates. An iterative solution is still possible, but some uncertainty is introduced due to local flow measurements which will be discussed in greater detail in chapter 4. Practically, equation 1.7 is best used for verification when the flow is slowed adiabaticly downstream of the vortex tube exits, until the experimenter is confident that the dynamic component may be neglected at the measurement station.

The entropy budget is

$$\begin{aligned} \dot{S}_{\mathrm{gen}} &= \dot{m}_{\mathrm{c}}\,(s_{\mathrm{c}} - s_{\mathrm{i}}) + \dot{m}_{\mathrm{h}}\,(s_{\mathrm{h}} - s_{\mathrm{i}}) \\ s_{\mathrm{gen}} &= \lambda\,(s_{\mathrm{c}} - s_{\mathrm{i}}) + (1-\lambda)\,(s_{\mathrm{h}} - s_{\mathrm{i}}) \end{aligned} \tag{1.8}$$

Under the perfect gas assumptions and their well-known change in entropy relations [1], Silverman [3] has reduced equation 1.8 to the inequality:

$$x^{\lambda}\left(\frac{1-\lambda x}{1-\lambda}\right)^{1-\lambda} \geq \left(\frac{p_{\mathrm{i}}}{p_{\mathrm{c}}}\right)^{\frac{1-\gamma}{\gamma}} \quad ; \quad x = \frac{T_{0\mathrm{c}}}{T_{0\mathrm{i}}} \tag{1.9}$$

where γ is the ratio of specific heats. Silverman uses Hilsch's vortex tube study [2] as an example, demonstrating that the reported measurements satisfy the inequality.

In addition to the shell balances, others have rendered the problem dimensionless using Buckingham-π theorem, including Stephan [14] and Baghdad et al. [15]. The process will be started here to illustrate the considerable barriers to progress in this particular problem. The first step in non-dimensionalization is to list the pertinent physical parameters; this has been done in table 1.1. There are 15 independent variables in total, with 4 primary dimensions, which suggests a maximum of 11 dimensionless π-groups are required to relate a dependent parameter (e.g. T_{c} or $T_{0,\mathrm{c}}$) to the known quantities:

$$\pi_0 = f(\pi_1, \pi_2, \ldots, \pi_{11}) \tag{1.10}$$

where π_0 is a ratio involving T_{c} or $T_{0,\mathrm{c}}$. Whether or not equation 1.10 is considered explicitly, the parameters of the vortex tube, and their influence on temperature separation can be investigated experimentally. In completing this task, it should become clear which parameters are critical to temperature separation in Ranque-Hilsch flow, and whether they can be treated independently or not. Then, the empirically determined form of f can be compared with the theories of sections 1.3.1 and 1.3.3 to see which ones are accurate.

1.2.1 Review of Parametric Studies

A large portion of the literature on the RHVT focuses on characterizing the VT performance as a function of critical input parameters. In this section the influences of VT parameters are reviewed; enough to outline the general trends. Several review papers have collected many more parametric studies than have been mentioned here [16, 17, 18, 19, 20].

Hilsch's study [2] is a natural starting point. In his experiments, four different cold exit diameters $d_{\mathrm{c}} \in \{1.4, 1.8.2.2, 2.6\}$ mm were tested, finding T_{c} is minimized when $\lambda \approx 0.2$ and

Table 1.1: The independent VT parameters affecting temperature separation. The primary dimensions are length L, mass M, time T, and temperature θ

	Variable	Symbol	Dimensions
Geometric Parameters	length	L	L
	diameter	D	L
	number of nozzles	N	1
	inlet area	A_i	L^2
	cold exit diameter	d_c	L
	plug diameter at hot exit	d_h	L
	hot exit cone angle	α	1
Operating Parameters	inlet pressure	p_i	$\mathrm{ML^{-1}T^{-2}}$
	cold exit pressure	p_c	$\mathrm{ML^{-1}T^{-2}}$
	hot exit presssure	p_h	$\mathrm{ML^{-1}T^{-2}}$
	inlet static temperature	T_i	$\mathrm{ML^{-1}T^{-2}}$
	inlet mass flow rate	$\dot{m}_\mathrm{i}$	$\mathrm{MT^{-1}}$
Fluid Properties	molecular viscosity	μ	$\mathrm{ML^{-1}T^{-1}}$
	thermal conductivity	k	$\mathrm{MLT^{-3}\theta^{-1}}$
	specific heat at constant pressure	c_p	$\mathrm{L^2T^{-2}\theta^{-1}}$
	heat capacity ratio	$\gamma = c_p/c_v$	1

$d_\mathrm{c} = 1.4\,\mathrm{mm}$, while the latter three cold exit sizes produce more favourable cooling across the range of λ. The results are shown in in figure 1.2. In addition, Hilsch varied the inlet pressure, and found a positive correlation with VT performance.

Kırmacı [21] carried out an experimental study on a VT having $L/D = 15$ with $N \in \{2, 3, \ldots, 6\}$ and p_i in the range 150 kPa–700 kPa and held $\lambda = 0.5$ fixed. The overall temperature difference $T_\mathrm{h} - T_\mathrm{c}$ was observed to increase with increasing inlet pressure, while increasing the number of nozzles degraded temperature separation, while the overall temperature difference degraded with increasing the number of nozzles.

Skye et al. [22] conducted a series of experiments using a single-nozzle commercial vortex

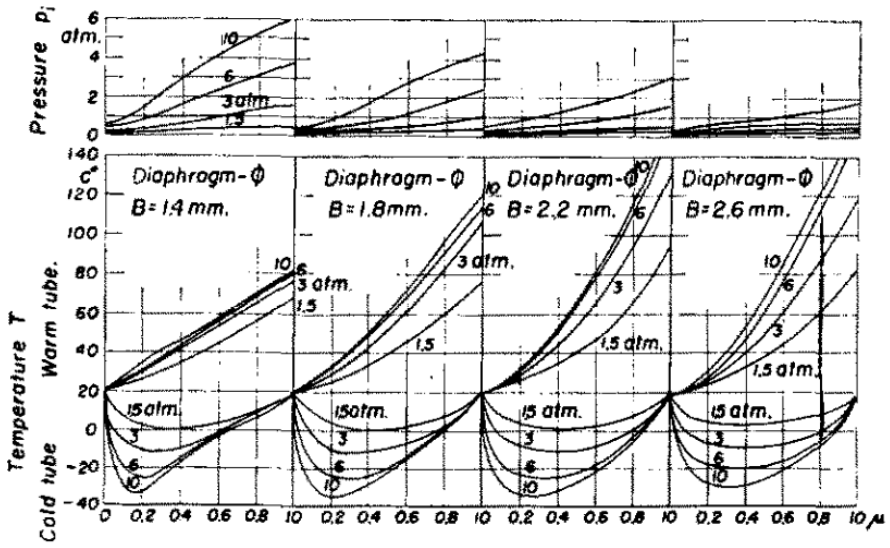

Figure 1.2: Summary of Hilsch's experiments showing performance variation with cold exit diameter and inlet pressure, where p_i is the pressure near the hot exit inside the VT [2]

tube with the dimensions $L = 10.6\,\text{cm}$ $D = 1.14\,\text{cm}$ ($L/D = 9.29$), and $d_c = 0.62\,\text{cm}$. In addition, they compared their results with steady, axisymmetric CFD simulations run using FLUENT software, yielding the plot shown in figure 1.3. In axisymmetric CFD simulations, the inlet flow is given both circumfrential and radial components to mimic experimental setups involving a large number of evenly spaced inlet nozzles.

In the experiments of Dincer et al. [23] ($L/D = 26.6$), the inlet pressure and hot exit plug position have independently varied to separate the influences of the inlet pressure and cold exit mass fraction. The inlet pressure was varied from 200 kPa to 420 kPa in increments of 20 kPa, where the hot end plug position was changed to vary the cold mass fraction at each inlet pressure over the range $0 < \lambda \leq 1$. They observed a modest, decaying, positive correlation between inlet pressure and net temperature separation.

Eiamasa-ard [24] and Li et al. [25] have conducted a similar experimental studies where the inlet pressure and cold mass flow rate were independently varied. They found a similar trends to Dincer et al.

Saidi and Valipour [26] have conducted a series of experiments studying, among other parameters, the effects of changing L/D from 20 to 78, in 5 increments. They showed the cold temperature separation at a cold mass fraction $\lambda = 0.55$ increases with L/D, until $L/D \approx 55.5$,

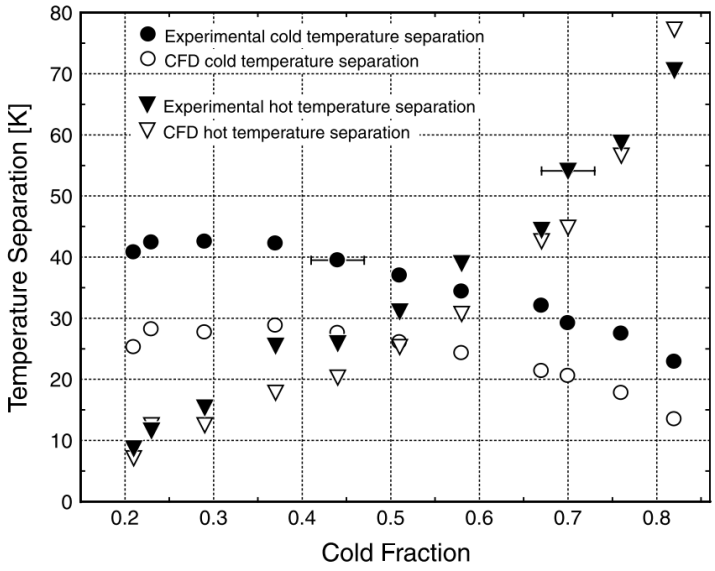

Figure 1.3: Comparison of experimental and CFD results from Skye et al. [22]

after which only modest increases in temperature separation are observed. In addition, they varied the cold orifice diameter to tube diameter ratio (d_c/D) from 0.16 to 0.62 in 5 increments and found a strong positive correlation between the diameter ratio and temperature separation up to $d_c/D = 0.5$, after which the temperature separation decreases.

Aydın and Baki [27] conducted an experimental study wherein the dimensions of the vortex tube were independently varied. To study the effects of vortex tube length variation, dimensions $D = 18\,\text{mm}$, $d_i = 5\,\text{mm}$, and L =250, 350, 550 and 750 mm were selected. The resulting plot shown in figure 1.4a reveals an interesting relationship between tube length and temperature separation at both exits: by and large only modest changes in the temperature separation were observed between the tube lengths of L =250, 550 and 750mm, but for the intermediate length $L = 350\,\text{mm}$, the temperature separation rises appreciably at both exits. Interestingly, the peak in cold exit temperature separation occurs at $\lambda = 0.2$ for all lengths except $L = 250\,\text{mm}$. A similar plot feature can be seen with the variation inlet nozzle diameter. It is curious that Aydın and Baki did not discuss these oddities.

Eiamsa-ard [24] conducted a series of experiments to explore the effects of a 'snail-shaped' entrance shroud with 1, 2, 3, and 4 nozzles pointing towards the tube, and compared this with a tangential inlet configuration with 4 nozzles. Comparing the snail-shaped nozzles, increasing the number of nozzles increase performance, and all snail geometries out-performed the

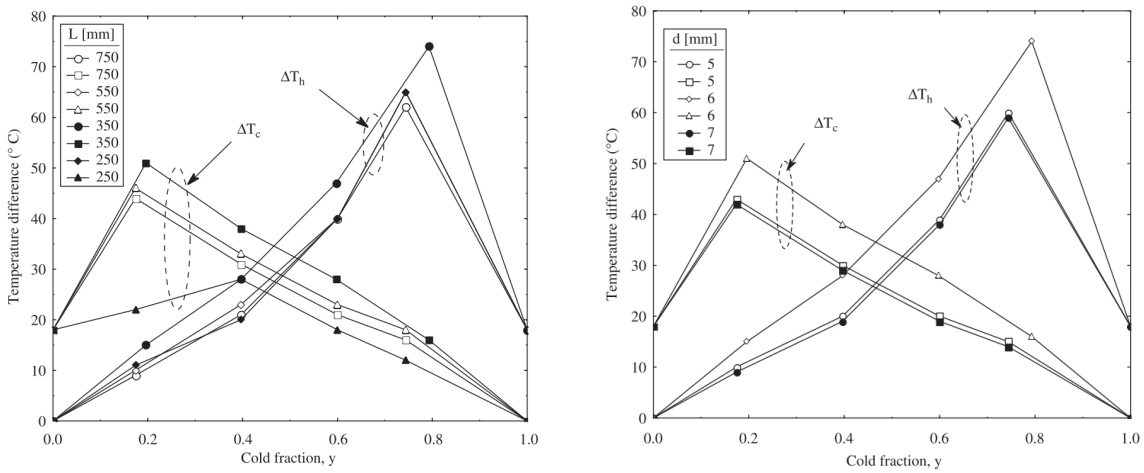

(a) Varying tube length

(b) Varying cold exit diameter

Figure 1.4: Temperature separation variation with geometric parameters from Ref. [27]

tangential-nozzle configuration.

1.2.2 Critical Review of Parametric Studies

Generally, parametric studies effectively characterize vortex tube behaviour over a range of parameters. Some general conclusions can be drawn:

- Temperature separation increases with inlet pressure as shown in many studies including [2, 28]. Importantly, Parker and Straatman [29] have shown in their experiments that temperature separation over a range of mass fractions is invariant with respect to the pressure ratio.

- Cold exit temperature separation is generally minimized in the vicinity of $\lambda \approx 0.2$.

Unfortunately, the literature also disagrees on several points. First, the available studies examining the influence of the length L, and the length-to-diameter ratio L/D offer no consensus. The review papers in the field offer limited guidance; Eiamsa-ard and Promvonge [17] concludes the optimum ratio is $L/D \approx 20$, while Yilmaz et al. [18] acknowledges the disharmony in the literature, simply reporting that L should be "many times" larger than D, but the effects on performance are limited beyond $L/D > 45$. Thakare et al. [19] offered a similarly vague statement. There is similar disagreement on the influence of d_c/D.

In general, progress on this front has been hampered by several interrelated problems. First, there are a large number of independent parameters affecting temperature separation; parameters describing the nozzle geometry and hot exit plug geometry can be added to the list of 15 given in table 1.1. Such a large design-space takes a long time to explore. In addition, there are more options for possible dimensionless π-groups (e.g. is it more pertinent to consider the Reynolds number, Euler number, or Mach number?). Researchers disagree on which groups are important. Moreover, there has been no "standard" VT adopted by the community: two researchers may study L/D effects and come to different conclusions, but comparison between the studies is made impossible because $D, N, A_{\mathrm{i}}, P_{\mathrm{i}}, \ldots$ are all different between the studies.

These issues are made all the more complicated by the interaction of different physical phenomena at different scales, which is best illustrated when discussing the influence of N. Results of some studies claim increasing the number of nozzles degrades performance [21, 30], while other studies claim the opposite [31, 10], and Dincer et al. [28] studied vortex tubes with 2, 4, and 6 nozzles and found 4 nozzles gave the best performance. Even without considering the overall effects on the flow field, the consequences of varying N can be difficult to anticipate. The situation might be complicated by several factors:

- while the upstream pressure was held constant (except for Ref. [31] where the mass flow rate has been fixed), the total mass flow rate through the VT increases as a consequence of providing additional channels, causing the vortex to strengthen.

- At the same time the flow rate through each channel should diminish somewhat, and the flow profile across the channels is subject to change.

- Furthermore, the compressibility of the flow causes the static temperature to drop as it passes through the nozzles; at the nozzle exit, heat transfer plays a significant role (demonstrated in chapter 4) in the local energy transfer, which depends on the local static temperature gradients.

- Each of the above items can be further complicated by the presence of shocks in the vicinity of the nozzles, which are seldom discussed in the literature.

Each of these factors might be significant, but a simple parametric study will not provide these

details. Indeed, Refs. [30, 28] only provide passing comments with respect to the first and second items in the above list.

When studying the functional dependence in parametric form, it is very tempting to assume that the influence of each of the parameters in equation 1.10 can be separated, either by summation, or by multiplicative factors:

$$\pi_0 = \sum_{i=1}^{M} f_i(\pi_i) \quad \text{or} \quad \pi_0 = \prod_{i=1}^{M} f_i(\pi_i) \tag{1.11}$$

where M is the totatl number of parameters. This assumption has been stated explicitly in Refs. [32, 15] with very limited accuracy, and implicitly assumed in other works. Given the shortcomings and complexities mentioned above, it seems unlikely that such simplifications can be made while still offering accurate predictions of temperature separation over a range of parameters.

The criticisms stated here stem from the assumption that the overall goal of these studies is to inform and challenge the theories surrounding Ranque-Hilsch flow and temperature separation. However, it is important to acknowledge that many of these studies also endeavor to aid VT designers in finding the best performing designs, while a complete understanding of temperature separation is not a primary goal.

Nevertheless, this thesis endeavors to identify the mechanisms of temperature separation in the RHVT, and no more progress can be made without considering the physics at play within the tube; the black box must be opened.

1.3 Fluid Mechanics of the Ranque-Hilsch Vortex Tube

While RHVTs are possible under the laws of thermodynamics, the mechanism(s) responsible for temperature separation must lurk in the altogether more complicated realm of fluid mechanics. Here are the governing equations of fluid mechanics, namely, the compressible Navier-Stokes equations:

$$\frac{\partial \rho}{\partial t} + \boldsymbol{\nabla} \cdot (\rho \mathbf{u}) = 0 \tag{1.12}$$

$$\rho \left(\frac{\partial \mathbf{u}}{\partial t} + (\mathbf{u} \cdot \boldsymbol{\nabla}) \mathbf{u} \right) = -\boldsymbol{\nabla} p + \mu \nabla^2 \mathbf{u} + \frac{1}{3} \mu \boldsymbol{\nabla} (\boldsymbol{\nabla} \cdot \mathbf{u}) \tag{1.13}$$

where ρ is the density, $\mathbf{u}$ is the velocity, t is time, p is thermodynamic the pressure, and μ is the viscosity. The solution to these equations will yield the flow structure inside the RHVT, which strongly affects the flow of energy inside the domain. Unfortunately, the non-linear and second derivative terms complicate the solution process, requiring the use of simplified models, or numerical methods to obtain adequate solutions. These will be addressed below.

While the energy shell balance written above is useful for parametric studies and verification checks, the energy balance for an infinitesimal control volume within the RHVT is required to analyze the internal energy separation mechanisms:

$$\rho \left(\underbrace{\frac{\partial \xi}{\partial t}}_{\substack{\text{unsteady} \\ \text{term}}} + \underbrace{\mathbf{u} \cdot \boldsymbol{\nabla} \xi}_{\substack{\text{advection} \\ \text{term}}} \right) = \underbrace{-p (\boldsymbol{\nabla} \cdot \mathbf{u})}_{\substack{\text{compressibility} \\ \text{term}}} - \underbrace{\boldsymbol{\nabla} \cdot \mathbf{q}}_{\substack{\text{heat flux} \\ \text{term}}} + \underbrace{\Phi}_{\substack{\text{viscous} \\ \text{term}}} \tag{1.14}$$

where $\xi(T)$ is the internal energy, $\mathbf{q}$ is the local heat flux due to conduction heat transfer, and Φ is the heat increase due to viscous dissipation within the flow field. As it has already been demonstrated, heat flux at the walls of the RHVT does not contribute to the temperature separation mechanisms, so boundary effects may be neglected for this analysis. However, the influence of heat transfer inside the domain cannot be ruled out.

With this knowledge in mind, each of the terms in equation 1.14 can be assessed as a potential motivator for energy separation. The unsteady term, the advection term, and the heat flux term (through application of Fourier's law) are all proportional to temporal or spatial variations in the temperature field, serving only to redistribute thermal energy throughout the domain. Since the RHVT does not rely on any initial energy gradients inside the tube, only the compressibility and viscous dissipation terms can initiate variations in the temperature field where none exist. This conclusion has an important corollary; since incompressible fluids have a constant density (barring material gradients, which seem difficult to attain in Ranque-Hilsch flow), $\boldsymbol{\nabla} \cdot \mathbf{u} = 0$ by equation 1.12, and the compressibility term vanishes. Therefore, viscous

dissipation is the only source of internal energy within incompressible flows. Moreover, since Φ must always be positive [33], the thermal energy must increase. This analysis explains the results obtained by Balmer [34], who found significant 'temperature separation' when water (incompressible) was used as a working fluid within a commercial RHVT, which was designed for use with air. Across the range of parameters studied, Balmer found the hot exit temperature exceeded the cold exit temperature, while the temperature of both exits significantly exceeded the inlet temperature. Given the exit temperatures differed substantially, there was still an energy separation mechanism at play, however no cooling effect is possible.

1.3.1 Review of Flow Structures in the RHVT

Figure 1.5 shows the fascinating flow pattern inside the RHVT. The offset of the inlets from the tube axis produces a strong vortex inside the tube. While part of the incoming fluid swirls as expected and proceeds to the hot exit, the remainder flows part way down the tube, before reversing towards the cold exit. Temperature, velocity, pressure, and density changes are observed throughout the domain.

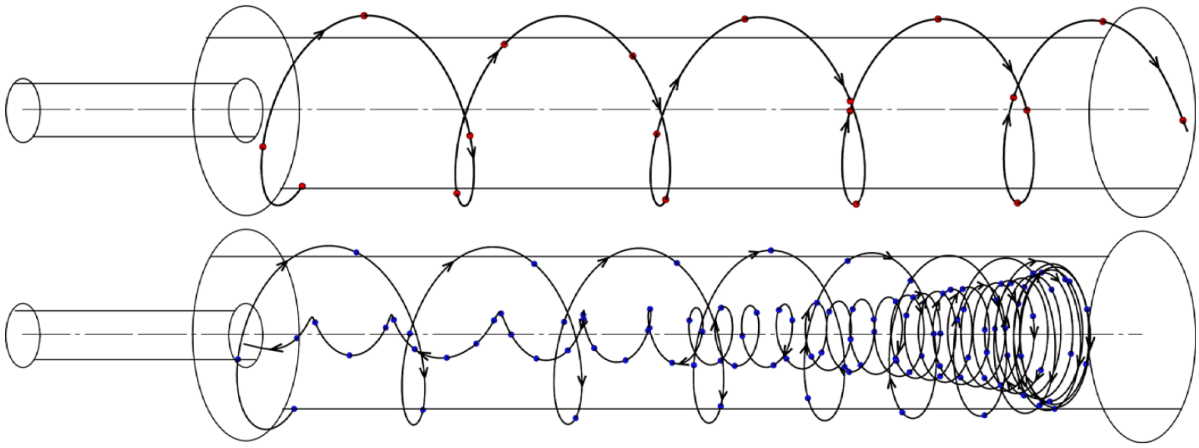

Figure 1.5: Streamlines from a CFD simulation moving to the hot and cold exit taken from Ref. [35]

Researchers often discuss processes occurring within the hot and cold streams; fluid parcels within the domain which eventually leave via the hot exit belong to the hot stream, and parcels eventually exiting via the cold exit belong to the cold stream.

While figure 1.5 captures the generally agreed upon flow structure inside the RHVT, there are still some details under debate. For example, the effect of turbulence on the flow structure is unclear. Also, some researchers have noted the presence of recirculation zones in the fluid, and claim they are integral to the temperature separation process.

Recently, Guo et al. [36] have thoroughly reviewed all studies of the RHVT in which internal flow properties have been collected, including intrusive and non-intrusive measurements of experimental data, and data from numerical calculations. A selection of these works will be highlighted in the next two subsections.

Experimentally and Numerically Observed Flow Structures

Although this thesis aims to *model* the RHVT, it would be remiss to ignore the literature on experimentally observed flow structures in the RHVT alongside numerical ones. While internal flow measurements and visualizations come with some unique challenges, careful experiments can yield insightful data which can be used as a comparison for models of the RHVT.

In an early study by Lay [8] hypodermic probes and hot-wire anemometers were inserted into a 2 in diameter, transparent co-flow RHVT at 6 different measurement stations. These experiments showed total temperature and total pressure increasing with radius, while the axial velocity close to the center-line reversed near the entrance (this anticipates the discovery of a recirculation bubble at the tube axis, a feature of co-flow RHVTs which is now well known). Finally, a decent visualization of the flow near the wall, very similar to figure 1.5, was obtained by photographing the tube after milk was injected at the inlet.

Ahlborn and Groves [37] used a 1.6 mm Pitot probe to measure velocities inside a 25 mm diameter vortex tube, and computed the mass fluxes at various locations. They noticed near the axis of the vortex tube greater mass flow appeared to be moving towards the cold exit than was measured downstream, leading them to the conclusion that an isolated, annular, recirculation region persisted within the domain.

More recently, Zhang et al. [38] have conducted unsteady Reynolds-Averaged Navier-Stokes (RANS) simulations using FLUENT Software, in which they have re-analyzed the vortex tube studied experimentally by Dincer et al. [23], and numerically using steady-state RANS models by Baghdad et al. [39]. Zhang et al. clearly demonstrated the presence of a precess-

ing vortex core (PVC) within a four-nozzle RHVT. A snapshot of the rotating core is clearly identifiable in figure 1.9. The time-averaged hot and cold temperature separations have slightly better agreement with the experiments of Dincer et al. than the steady simulations of Baghdad et al., especially at higher cold mass fractions.

Xue et al. [40] used 2D particle image velocimetry to visualize the flow at axial cross-sections within a 30 mm co-flow VT with water. They confirmed experimentally the presence of a precessing vortex core discovered by Zhang et al.

Shamsoddini et al. [31] conducted 3D, steady, RANS simulations using FLUENT and the RNG $k-\varepsilon$ model to study the VT of Aljuwayhel et al. [41] to determine the effects of increasing the number of tangential nozzles. Nozzles were evenly spaced around the circumference, and tangentially-oriented to the tube. Configurations with $n = 2, 3, 4, 6, 8$ nozzles were considered, and performance improved as the number of nozzles were increased. Perhaps the most noteworthy outcome from Shamsoddini et al.'s work is shown in figure 1.6: the 3D simulation including 8 nozzles is nearly identical to the results obtained from an equivalent axisymmetric geometry. The axisymmetric results are also in close agreement with experiments conducted by Aljuwayhel et al.

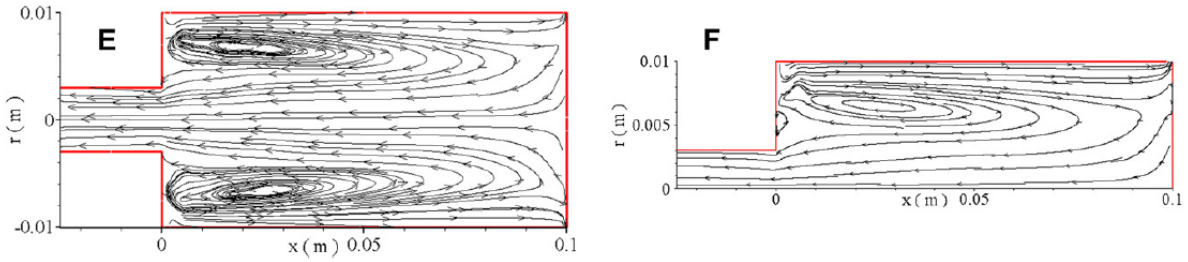

Figure 1.6: Comparison of a 3D simulation of a vortex tube with eight nozzles at the periphery with an equivalent axisymmetric simulation, modified from Ref. [31]

2D Disc Approximations

A pair of 1948 reports by Kassner and Knoernschild [42] proposed a working theory of RHVT operation one year after Hilsch's re-discovery. While rudimentary, the report was the first to analyze mathematically the processes occuring inside the RHVT, by assuming a strong circumferential flow field that is very close to the Rankine vortex in nature. The report conveyed the

idea that momentum can be transferred outward via shear in a rotating fluid, and concluded by saying this must be the energy separation mechanism inside the RHVT, while making some unclear statements about heat transfer.

Pengelley [43] considers a viscous, compressible, perfect gas with radial and circumferential motions in an annular region between two porous cylinders, in the absence of heat transfer. Starting from the Navier-Stokes and energy equations, they assume the radial flow is small when compared to the circumferential component, and solve the simplified equations. The results show that there are circumstances wherein the stagnation temperature decreases significantly as it the fluid moves towards the center, while work is transferred to the outer wall.

Savino and Ragsdale [44] have carried out experiments on a device very similar to the device studied by Pengelley: in their case an outer shroud was supplied with air at high pressure, this air was deflected in the circumferential direction by a ring of guide vanes as it moved towards the low pressure axial exit. They observed a significant total temperature drop, and while no direct comparisons were made, they commented that their results are in agreement with Pengelly's findings.

Allahverdyan and Fauve [45] have studied analytically a similar flow to Pengelly, except the influence of large radial velocities and internal heat transfer has been taken into account. They also argue that Pengelley did not accurately account for the heat transfer boundary condition, so the model falls somewhat short of the goal of demonstrating that cooling of a swirling compressible fluid is possible without energy input. Here the authors carefully demonstrate that cooling is acheived not through the action of refrigeration (i.e. external work input), or through heat transfer via the boundaries, but through the action of viscosity, and a net positive work output is done by the fluid on the rotating porous boundaries. The results are in strong agreement with the measurements of Savino and Ragsdale. An example of the results obtained is shown in figure 1.7.

Polihronov and Straatman [46] considered an altogether different setup, studying the radially-inward flow of a perfect gas through a straight duct rotating about an axis perpendicular to the duct centerline. Treating the problem as one-dimensional, and applying the conservation of energy, they demonstrated that the temperature between a pressurized supply tank at radius r is reduced by $\omega r/c_p$, where ω is the angular velocity of the duct. They attribute the physics of

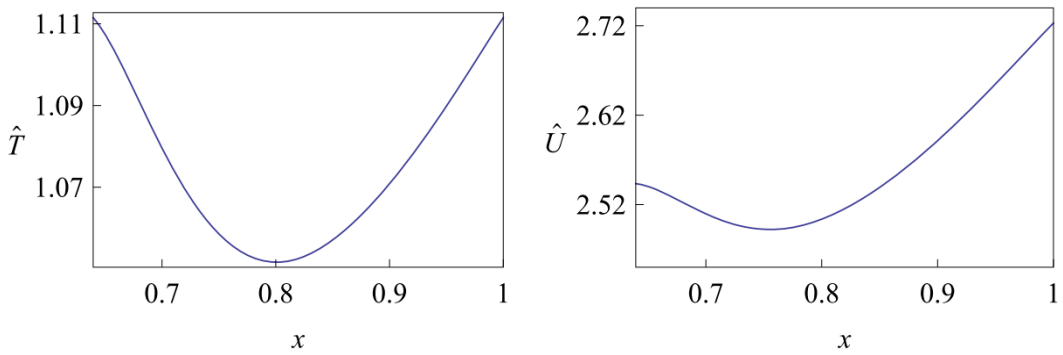

Figure 1.7: Results obtained by Allahverdyan and Fauve [45], wherein $\hat{T}$ is the dimensionless static temperature, $\hat{U}$ is the dimensionless stagnation enthalpy, and x is the dimensionless radial distance between the rotating cylinders

this temperature drop to the conservation of momentum of the system as a whole; as the fluid moves towards the center of rotation, it imparts some angular momentum to the walls of the duct through which it moves.

Axisymmetric Approximations

Van Deemter [47] aimed to describe RHVT flow using an extended Bernoulli equation, but in reality described the flow inside a uniflow VT.

Deissler and Perlmutter [48] described a similar setup to Pengelley, except the vortex is divided into an outer annulus and an inner core. Linear variations in axial velocity u_z are permitted, but the remaining quantities including temperature, pressure, and other velocity components, are independent of axial position (i.e. $\frac{\partial}{\partial z} = 0$). A focus is placed on the influence of turbulence by replacing μ with a constant eddy viscosity $\rho\varepsilon$ in the momentum equations, whose value is informed by experiments. The analysis resulted in a Rankine vortex-like tangential velocity profile across the two flow regions. Predictions of hot and cold exit temperature separation compared poorly with the experimental data of Hilsch [2], although the authors claim this is due to unexpected heat transfer in Hilsch's experiments. In addition, an attempt was made to quantify the different modes of energy transfer in a fully 3D model. It was found that two modes, the so-called 'turbulent conduction due to temp gradients' and 'turbulent conduction due to pressure gradients' were the largest magnitude energy transfer mechanisms, but, having

opposite signs, they largely cancelled over the range of r. The remaining shear work transfer then became the dominant mechanism.

Lewellen [49] endeavored to study the motion of an incompressible fluid entering a cylindrical container tangentially, spiraling towards the center, and exiting through an axial opening. Lewellen argues that previous works by Deissler and Perlmutter [48] and Einstein and Li [50] give the axial momentum equation ”no consideration”. Lewellen cast the governing equations in terms of the stream function and circulation, and developed series expansion solutions in this framework, and emphasized that existing exact solutions (such as those by Donaldson and Sullivan [51]) cannot satisfy arbitrary boundary conditions, and thus have limited utility in practice.

Linderstrøm-Lang [52] adopted the series expansion approach studied by Lewellen to develop incompressible flow solutions of the RHVT. To do this, the tube is divided into four regions: a main flow region, an inlet region, a small annular region containing the boundary layer, and a region close to the hot exit which contains the stagnation point. It seems only flow in the first region is solved. The laminar viscosity is again replaced by a constant eddy viscosity. The temperature profile is computed from the decomposed energy equation discussed by Reynolds [53] (see section 1.3.3) where the fluctuating terms are replaced by eddy viscosity models developed by Kassner and Knoernschild [42] and Deissler and Perlmutter [48], and a host of other approximations based on physical arguments. Moderate agreement with Hilsch's experimental data is observed.

1.3.2 Critical Review of Modelled Flow Structures

Temperature separation in the RHVT is dependent on the thermodynamics within the tube, which is closely coupled to the momentum transport, and, consequently, the flow structure. Therefore, viable theories on the nature of temperature separation should make some reference to the flow structure. Unfortunately, the flow is compressible, highly turbulent, and fully 3D.

Much data on the flow structure and properties has been gathered in the years since Ranque's discovery. Each data set needs to be interrogated for quality, though in different ways depending on how it was collected.

The comparison of Shamsoddini et al. [31] between the 2D and 3D simulations are encouraging, however the use of a 2D axisymmetric CFD model requires that the injection inlet angle of the flow be approximated somehow. The only known method for doing this is detailed by Skye et al. [22], who roughly approximated this angle based on the nozzle geometry in their experiment. No known studies examine other methods for approximating this inlet angle, or test the sensitivity of the results.

In many CFD studies [54, 31, 22, 39, 55] the computational domains are truncated at the 'immediate' exits of the vortex tube shown in figure 1.1, but, in the experiments from which these studies draw their comparisons, flow leaving these exits is commonly collected into plenums and exhausted to a downstream location where the measurements are taken. Often, these experimental works place probes in unfavourable locations [2], or do not specify where the measurement station is and how the probe(s) are positioned to collect the data [28, 56]. This leads to some confusion about whether total or static quantities have been measured, and which ones have been reported. As a result, comparisons with CFD results are tenuous for two reasons: pressure boundary conditions might have been applied at a different position in the CFD model than the measurement condition which can skew the calculation, and the temperatures at the boundaries extracted from the CFD results might not correspond to temperatures measured at a single point in the experiment.

Two-dimensional representations of Ranque-Hilsch flow are inherently simpler than 3D models, an their solutions easier to obtain. The work of Allahverdyan and Fauve [45] builds on previous attempts, and provides the most complete analytical model of compressible, swirling flow between porous cylinders. The obvious drawback is that it does not include any axial variations, and thus temperature separation cannot be achieved in the exact manner that it occurs in the RHVT.

While Deissler and Perlmutter [48] provided the first 3D model of RHVT, their model considered only linear variations in the axial velocity, which is a poor approximation in light of experimental findings [57, 58]. Their final solution also requires numerical methods to obtain.

Linderstøm-Lang [52] has addressed some of the shortcomings of Deissler and Perlmutter's model, however the process of solving the reduced equation set is cumbersome, and the final product still only obtains a solution field for a region of the flow field upstream of the stagnation

point in the flow. In addition, the details of all the approximations required to arrive at his reduced model are relegated to three auxillary papers, which are unavailable. At the same time, this study was, to the author's knowledge, the last, and most detailed numerical study of the RHVT before the advent of general CFD codes. In a way, this paper reveals the tension between striving for an accurate characterization of all the physical processes occurring in the RHVT (which is now doable), and the pursuit of simpler models which attempt to lay bare the mechanisms at play, by ignoring the irrelevant complexities. The ideal model should include enough of the relevant effects to satisfactorily predict temperature separation across a wide range of model parameters, while also making the role of energy separation mechanisms obvious.

1.3.3 Review of Temperature Separation Theories

With[2] general understandings of vortex tube operation, and the flow structure within, analysts of the RHVT have postulated several theories explaining the temperature separation phenomenon first observed by Ranque.

Pressure Gradient

Perfect gases undergoing isentropic expansion processes exhibit a temperature increase according to the well known relations:

$$\frac{T_2}{T_1} = \left(\frac{\rho_2}{\rho_1}\right)^{\gamma-1} = \left(\frac{p_2}{p_1}\right)^{(\gamma-1)/\gamma}, \tag{1.15}$$

Clearly, a decreasing density between the two states results in an decrease in temperature. Ranque [59] first attributed the temperature drop to adiabatic expansion.

Acoustic Streaming

The first researcher to comment on acoustic phenomena occurring within the RHVT was Kurosaka [60], who identified an interesting link between acoustic intensity and total temperature separation, visible in figure 1.8. Most notably, the drop-off in sound intensity coin-

[2] or without

cides with a sudden increase in cold outlet temperature. This is the first substantial evidence suggesting an acoustic phenomena occurring within the RHVT may be partly responsible for temperature separation.

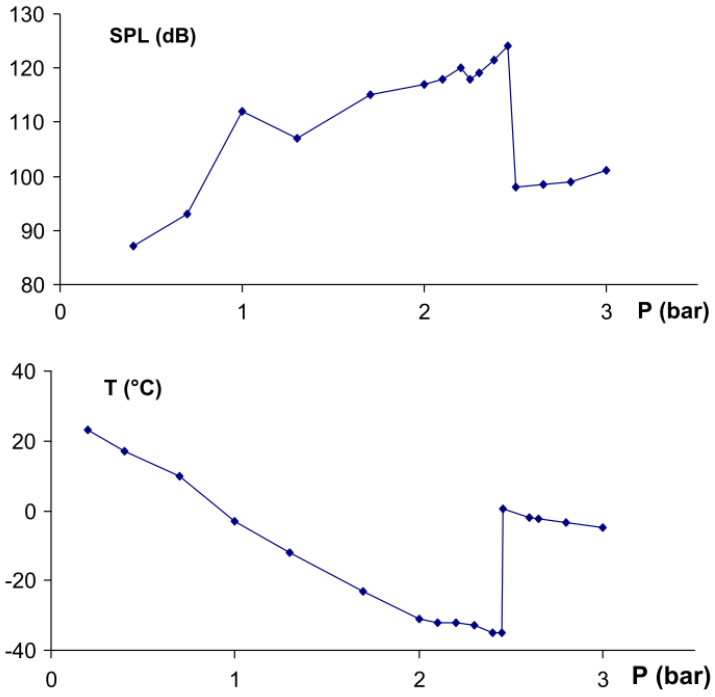

Figure 1.8: Measurement of acoustic intensity and cold exit temperature over a range of inlet pressures. Data from Ref. [60], figure from Ref. [61].

Kuroda [62] also noticed the drop-off of temperature separation with sound intensity in his experiments. Kuroda further identified several 'pure tone' intensity spikes, which he attributed to velocity fluctuations in the circumferential direction.

The precessing vortex core found in the numerical simulations of Zhang et al. [38, 6] and their claims that the "vibrating boundary layer" is responsible for temperature separation are in the same vein as the work of Kurosaka and Kuroda; however their work stops short of drawing this comparison.

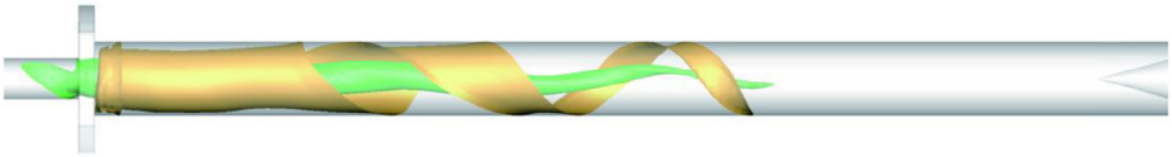

Figure 1.9: Instantaneous iso-surfaces of the axial velocity [38].

Turbulence

Other researchers claim that turbulence is responsible for energy separation. This theory was first championed by Deissler and Perlmutter [48], who analytically studied the a simplified set of turbulent energy equations including an approximated eddy diffusivity, to argue that the turbulent shear work term in the energy equation was positive in the periphery of the VT, thereby adding heat to the system, and negative near the tube axis; acting as a sink.

Alan J. Reynolds [53] also investigated the influence of turbulence in the RHVT. First, Reynolds decomposition[3] is performed on the total energy equation where the heat flux and viscous terms are absent. This is followed by an order-of-magnitude analysis of the mean and fluctuating terms, culminating in a description of the energy exchanges of a compressible lump of fluid moving up and down the radial pressure gradient, wherein the energy exchanges are related to the surviving terms of the decomposed energy equation. The author concludes by arguing that heat transfer is the dominant energy mechanism in the core of the VT, while 'work fluxes' dominate the periphery.

Liew et al. [63] have adopted this theory, asserting that radial velocity fluctuations are responsible for a heat exchange process which heats the outer region and cools the inner region. While supporting this theory, they have focused their effort on developing a semi-empirical relationship based on an approximation of the inner and outer core velocity profiles, along with other approximations to yield an equation which accurately predicts the temperature separation.

Secondary Circulation

Some numerical studies have revealed the presence of re-circulation region(s) at various points within the VT, exemplified by figure 1.10. Both Ahlborn and Groves [37, 64], and Xue and

[3] named after *Osborne* Reynolds, of course

others [65, 66, 67]. They suggest multiple re-circulation zones exist, each one behaving as a heat pump to move energy away from the core and towards the periphery.

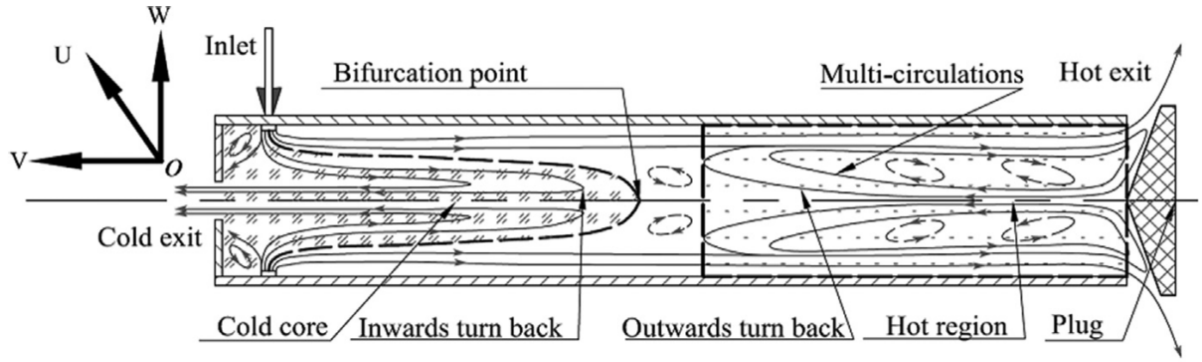

Figure 1.10: Hypothesized multi-circulation streamline plot modified from Xue et al. [65]

While earlier papers have provided mediocre evidence for this theory, more recent papers reporting the results of steady and unsteady, 3D, RANS and LES results have included streamline plots depicting multiple recirculation zones occuring within short vortex tubes [63, 68, 69, 70]. The re-circulation zones appear to be highly mobile; very sensitive to geometry and boundary conditions.

Work Transfer

Other researchers still have contended that shear work is the mode by which kinetic energy is transferred from the cold stream to the hot stream. The consequent reduction in angular kinetic energy of the inner core reduces the centripetal acceleration and causes the core to narrow towards the cold exit, cooling because of the contraction. The opposite effect is hypothesized for the outer vortex; the increased kinetic energy results in an increase in centripetal acceleration, and the outer core is compressed against the tube wall, resulting in a temperature increase.

Hilsch [2] first proposed this idea without evidence in his initial study of the vortex tube. Since then, the hypothesis has been supported by numerous researchers. The analyses of Pengelley [43] and Allahverdyn and Fauve [45] coupled with experiments of Savino and Ragsdale [44] clearly show work transfer to be the dominant energy transfer mechanism in 2D planar flows most similar to the RHVT. The alternative approach of Polihronov and Straatman [46] demonstrates that cooling can be achieved through action on external surfaces.

In addition, several authors conducting CFD studies on the RHVT have used their results to compute the energy transfers between the cold and hot streams of fluid [41, 71, 72, 73, 74]. In each case work transfer was found to be the dominant form of energy transfer, with heat transfer serving to degrade temperature separation.

1.3.4 Critical Review of Temperature Separation Theories

While many theories have been proposed, some of the earlier ones have fallen out of favour. In the case of adiabatic expansion, the theory can be dismissed because the data obtained in many cases (Gao [75] and Xue et al. [76]) have both shown that equation 1.15 over-predicts the temperature drop significantly. While the temperature drop due to sudden expansion is important, it does not explain the temperature rise occurring at the hot exit.

Acoustic streaming is a highly interesting theory that has been under-explored in the literature: it seems there have been no followup experimental studies since the original works by Kurosaka [60] and Kuroda [62]. These observations have not been definitively linked to the precessing vortex core discovered in the numerical simulations of Zhang et al. either.

There is some confusion as to whether the turbulence theory is synonymous with the work transfer theory, as work transfer is greatly enhanced by the presence of turbulence, and the supporting authors sometimes signal the importance of work transfer in their writing. Their focus remains, however, on the importance of transport due to small turbulent fluctuations across the radial pressure gradient. Naturally, the scale of these effects are too small for them to be observed experimentally using currently available instruments, but a direct numerical simulation of the full problem, harnessing the resources at a state-of-the-art high performance computing center may be able to resolve these small scale activities. No known computational study of this magnitude has been conducted on the RHVT, so there is not yet any direct evidence to support this theory.

Perhaps the strongest evidence against theories of acoustic streaming, small scale turbulent activity, or any other physics aside from classical thermodynamics and fluid mechanics is this: numerical simulations using the general forms of the governing equations, generalized turbulence models, perfect gas assumptions and standard properties, have repeatedly predicted

experimentally measured values of temperature separation within a reasonable margin of error [22, 41, 38, 15, 77, 78] (c.f. figure 1.3). Since these computational studies are capable of predicting temperature separation without any unsteadiness, and without the use of specialized turbulence models, it stands to reason that the energy separation mechanism must be contained within the basic physics of these simulations. This does not preclude acoustic streaming or exotic turbulent activity from playing a role in the temperature separation process, but it does indicate that they are not the primary drivers of the effect.

Moreover, while stationary and mobile recirculation regions are often observed, at least two authors have obtained simulation results wherein temperature separation is adequately predicted, and no recirculation regions are present in the time-averaged flow structures [71, 22].

Work transfer is, in this author's opinion, the most likely explanation of the temperature separation phenomenon. It has been supported since the VTs re-discovery by Hilsch and evidenced through the detailed analyses of Allahverdyn and Fauve [45]. The most persuasive evidence is post-processing of the CFD results by Aljuwayhel et al. [41] wherein the authors compute the energy transfer from the hot stream to the cold stream via three mechanisms: circumferential shear work, axial shear work, and heat transfer. The total energy transferred by these three mechanisms was shown to balance with the total energy loss of the cold stream, and the energy gain of the hot stream. Energy transfer from the cold stream to the hot stream dominates the other two modes which transfer in the opposite direction, degrading the overall energy separation.

Despite the overwhelming support of the work transfer theory, the majority of recent papers published claim 'the mechanism responsible for temperature separation in the RHVT is still unknown', indicating the community is not satisfied with the available evidence.

Perhaps a more important task than convincing the VT community to rethink their stance is to pursue accurate modelling of the RHVT, which is of more use to designers who want to be able to predict the temperature separation of their designs. To this end, many of the numerical models used to predict energy separation, although they do capture energy separation, are somewhat unrealistic, containing boundary conditions that do not match the experiments to which they correspond, and containing other approximations which have not yet been justified.

1.4 Thesis Outline

In this thesis I endeavor to address some the literature gaps identified in the preceeding critical reviews. Contained in the following chapters are three efforts to improve modelling of the Ranque-Hilsch phenomenon and related flows, along with their bibliographic references:

- In chapter 2 the rotating duct problem introduced by Polihronov and Straatman [46] is revisited. Starting from the general compressible Euler equations in a non-stationary reference frame closed form expressions for velocity, temperature, density and pressure along the duct are determined. These results are more general than those obtained by Polihronov and Straatman, as the change of in-frame kinetic energy has been retained. The improvement of the present results over Polihronov and Straatman's is demonstrated by comparison with the results of a CFD study. The new results are further generalized to the case of a rotating duct with varying cross-sectional area, and again for a general curved passage in three-dimensional space. The work required or derived from the rotating duct is also been computed. The choked flow condition within the passage of varying cross-sectional area is identified, along with the constraints which must be placed on the Mach, Rossby, and tip Mach numbers to avoid choked flow. Finally, a straightforward technique to identify any locations where an ideal rotating flow in a constrained passage will become sonic is presented.

- In 1966 Chang-Yi Wang [79] used the streamfunction in concert with the vorticity equations to develop a methodology for obtaining exact solutions to the incompressible Navier-Stokes equations, now known as the extended Beltrami method. In Wang's approach, the vorticity is represented by the sum of a linear function of the streamfunction and an assumed auxiliary function, such that the vorticity equation can be reduced to a quasi-linear partial differential equation, and exact solutions are obtainable for many choices of the auxiliary function. In chapter 3 a natural extension of Wang's formulation to three-dimensional flows in arbitrary orthogonal curvilinear co-ordinates has been derived, wherein two auxiliary functions are formed at the outset, with the caveat that the pressure and velocity components may vary in two spatial dimensions. As is the case with two-dimensional extended Beltrami flows, exact solutions are only obtainable when

the forms of the auxiliary functions are 'simple enough' to render the governing equations solvable. To demonstrate the solutions which may be obtained using the extended formulation, the well-known Kovasznay flow is generalized to a three-dimensional flow. A unique solution in plane polar co-ordinates is found. An extension to the solution to Burgers vortex has been derived, and discussed in the context of existing literature. Finally, a new 3D swirling flow solution which is the angular analogue to Kovasznay flow has been developed. The streamlines of this solution are very similar to the general Ranque-Hilsch flow shown in figure 1.5.

- In chapter 4, the relative impacts that different boundary conditions have on the temperature separation predictions of Computational Fluid Dynamics (CFD) models of the RHVT are explored by comparing different permutations of fixed pressure and fixed mass flow rate conditions imposed at the inlet, cold exit, and hot exit. Concurrently, the impacts of including the exit plenums and inlet shroud in the computational models on temperature separation are examined. A 3D CFD model is run using the k-ε, k-ω, k-ω SST, and SAS SST turbulence models, and their relative impacts on energy separation are discussed. Finally, the efficacy of the often-used axisymetric assumption when modelling the RHVT computationally is tested, and a new method for computing the angle of injection for axisymetric CFD studies has been validated. In all cases, circumferential shear work is found to be the dominant mode of energy separation.

Bibliography

[1] Y. A. Cengel and M. A. Boles, *Thermodynamics: an engineering approach*. McGraw-Hill Higher Education, 8th ed., 2006.

[2] R. Hilsch, "The use of the expansion of gases in a centrifugal field as cooling process," *Review of Scientific Instruments*, vol. 18, no. 2, pp. 108–113, 1947.

[3] M. Silverman, "The vortex tube: a violation of the second law?," *European Journal of Physics*, vol. 3, pp. 88–92, 1982.

[4] N. Dukhan, M. Cress, and M. R. Cosley, "Cooling and heating system for an equipment enclosure using a vortex tube," 11 2000.

[5] A. D. Gutak, "Experimental investigation and industrial application of Ranque-Hilsch vortex tube," *International Journal of Refrigeration*, vol. 49, no. 0, pp. 93–98, 2015.

[6] B. Zhang and X. Guo, "Prospective applications of Ranque–Hilsch vortex tubes to sustainable energy utilization and energy efficiency improvement with energy and mass separation," *Renewable and Sustainable Energy Reviews*, vol. 89, pp. 135–150, 2018.

[7] S. Comassar, "The vortex tube," *Journal of the American Society for Naval Engineers*, vol. 63, pp. 99–108, 3 1951.

[8] J. E. Lay, "An Experimental and Analytical Study of Vortex-Flow Temperature Separation by Superposition of Spiral and Axial Flows: Part 1," *Journal of Heat Transfer*, vol. 81, pp. 202–211, 8 1959.

[9] S. Eiamsa-Ard and P. Promvonge, "Numerical simulation of flow field and temperature separation in a vortex tube," *International Communications in Heat and Mass Transfer*, vol. 35, no. 8, pp. 937–947, 2008.

[10] P. Promvonge and S. Eiamsa-ard, "Investigation on the Vortex Thermal Separation in a Vortex Tube Refrigerator," *ScienceAsia*, vol. 31, no. 3, p. 215, 2005.

[11] J. P. O'Connell, "Detailed thermodynamics for analysis and design of Ranque-Hilsch vortex tubes," *AIChE Journal*, vol. 64, no. 3, pp. 1067–1074, 2017.

[12] H. R. Thakare and A. D. Parekh, "Experimental investigation & CFD analysis of Ranque—Hilsch vortex tube," *Energy*, vol. 133, pp. 284–298, 2017.

[13] P. A. Ramakrishna, M. Ramakrishna, and R. Manimaran, "Experimental Investigation of Temperature Separation in a Counter-Flow Vortex Tube," *Journal of Heat Transfer*, vol. 136, no. 8, p. 082801, 2014.

[14] K. Stephan, S. Lin, M. Durst, F. Huang, and D. Seher, "A similarity relation for energy separation in a vortex tube," *International Journal of Heat and Mass Transfer*, vol. 27, no. 6, pp. 911–920, 1984.

[15] M. Baghdad, A. Ouadha, and Y. Addad, "Effects of kinetic energy and conductive solid walls on the flow and energy separation within a vortex tube," *International Journal of Ambient Energy*, pp. 1–17, 11 2018.

[16] R. Westley, "A Bibliography and Survey of The Vortex Tube," tech. rep., College of Aeronautics, Cranfield, 1954.

[17] S. Eiamsa-ard and P. Promvonge, "Review of Ranque-Hilsch effects in vortex tubes," *Renewable and Sustainable Energy Reviews*, vol. 12, no. 7, pp. 1822–1842, 2008.

[18] M. Yilmaz, M. Kaya, S. Karagoz, and S. Erdogan, "A review on design criteria for vortex tubes," *Heat Mass Transfer*, vol. 45, no. 5, pp. 613–632, 2009.

[19] H. R. Thakare, A. Monde, and A. D. Parekh, "Experimental, computational and optimization studies of temperature separation and flow physics of vortex tube: A review," *Renewable and Sustainable Energy Reviews*, vol. 52, pp. 1043–1071, 2015.

[20] K. D. Devade and A. T. Pise, "Issues and prospects of energy separation in vortex tubes: Review," *Heat Transfer-Asian Research*, vol. 47, pp. 461–491, 5 2018.

[21] V. Kırmacı, "Exergy analysis and performance of a counter flow Ranque-Hilsch vortex tube having various nozzle numbers at different inlet pressures of oxygen and air," *International Journal of Refrigeration*, vol. 32, no. 7, pp. 1626–1633, 2009.

[22] H. M. Skye, G. F. Nellis, and S. A. Klein, "Comparison of CFD analysis to empirical data in a commercial vortex tube," *International Journal of Refrigeration*, vol. 29, no. 1, pp. 71–80, 2006.

[23] K. Dincer, S. Baskaya, B. Z. Uysal, and I. Ucgul, "Experimental investigation of the performance of a Ranque-Hilsch vortex tube with regard to a plug located at the hot outlet," *International Journal of Refrigeration*, vol. 32, no. 1, pp. 87–94, 2009.

[24] S. Eiamsa-ard, "Experimental investigation of energy separation in a counter-flow Ranque-Hilsch vortex tube with multiple inlet snail entries," *International Communications in Heat and Mass Transfer*, vol. 37, no. 6, pp. 637–643, 2010.

[25] N. Li, Z. Y. Zeng, Z. Wang, X. H. Han, and G. M. Chen, "Experimental study of the thermal separation in a vortex tube," *International Journal of Refrigeration*, vol. 55, pp. 93–101, 2015.

[26] M. H. Saidi and M. S. Valipour, "Experimental modeling of vortex tube refrigerator," *Applied Thermal Engineering*, vol. 23, no. 15, pp. 1971–1980, 2003.

[27] O. Aydın and M. Baki, "An experimental study on the design parameters of a counterflow vortex tube," *Energy*, vol. 31, no. 14, pp. 2427–2436, 2006.

[28] K. Dincer, S. Baskaya, and B. Z. Uysal, "Experimental investigation of the effects of length to diameter ratio and nozzle number on the performance of counter flow Ranque-Hilsch vortex tubes," *Heat and Mass Transfer*, vol. 44, no. 3, pp. 367–373, 2008.

[29] M. J. Parker and A. G. Straatman, "Experimental Study on the Impact of Pressure Ratio on Temperature Drop in a Ranque-Hilsch Vortex Tube," *In Preparation*, 2020.

[30] V. Kırmacı and O. Uluer, "An Experimental Investigation of the Cold Mass Fraction, Nozzle Number, and Inlet Pressure Effects on Performance of Counter Flow Vortex Tube," *Journal of Heat Transfer*, vol. 131, 8 2009.

[31] R. Shamsoddini and A. H. Nezhad, "Numerical analysis of the effects of nozzles number on the flow and power of cooling of a vortex tube," *International Journal of Refrigeration*, vol. 33, no. 4, pp. 774–782, 2010.

[32] S. Subudhi and M. Sen, "Review of Ranque–Hilsch vortex tube experiments using air," *Renewable and Sustainable Energy Reviews*, vol. 52, pp. 172–178, 2015.

[33] R. B. Bird, W. E. Stewart, and E. N. Lightfoot, *Transport Phenomena*. John Wiley & Sons, 2007.

[34] R. T. Balmer, "Pressure driven Ranque Hilsch temperature separation in liquids," *Journal of fluids Engineering*, vol. 110, no. 2, pp. 161–164, 1988.

[35] T. Farouk and B. Farouk, "Large eddy simulations of the flow field and temperature separation in the Ranque-Hilsch vortex tube," *International Journal of Heat and Mass Transfer*, vol. 50, no. 23-24, pp. 4724–4735, 2007.

[36] X. Guo, B. Zhang, B. Liu, and X. Xu, "A critical review on the flow structure studies of Ranque–Hilsch vortex tubes," *International Journal of Refrigeration*, vol. 104, pp. 51–64, 8 2019.

[37] B. Ahlborn and S. Groves, "Secondary flow in a vortex tube," *Fluid Dynamics Research*, vol. 21, pp. 73–86, 1997.

[38] B. Zhang, X. Guo, and Z. Yang, "Analysis on the fluid flow in vortex tube with vortex periodical oscillation characteristics," *International Journal of Heat and Mass Transfer*, vol. 103, pp. 1166–1175, 2016.

[39] M. Baghdad, A. Ouadha, O. Imine, and Y. Addad, "Numerical study of energy separation in a vortex tube with different RANS models," *International Journal of Thermal Sciences*, vol. 50, pp. 2377–2385, 12 2011.

[40] Y. Xue, J. R. Binns, M. Arjomandi, and H. Yan, "Experimental investigation of the flow characteristics within a vortex tube with different configurations," *International Journal of Heat and Fluid Flow*, vol. 75, no. April 2018, pp. 195–208, 2019.

[41] N. F. Aljuwayhel, G. F. Nellis, and S. A. Klein, "Parametric and internal study of the vortex tube using a CFD model," *International Journal of Refrigeration*, vol. 28, no. 3, pp. 442–450, 2005.

[42] R. Kassner and E. Knoernschild, "Friction laws and energy transfer in circular flow," tech. rep., Wright-Patterson Air Force Base, Dayton, OH, 1948.

[43] C. D. Pengelley, "Flow in a Viscous Vortex," *Journal of Applied Physics*, vol. 28, no. 1, pp. 86–92, 1957.

[44] J. M. Savino and R. G. Ragsdale, "Some Temperature and Pressure Measurements in Confined Vortex Fields," *Journal of Heat Transfer*, vol. 83, no. 1, pp. 33–36, 1961.

[45] A. E. Allahverdyan and S. Fauve, "Modeling gasodynamic vortex cooling," *Physical Review Fluids*, vol. 2, p. 084102, 8 2017.

[46] J. G. Polihronov and A. G. Straatman, "Thermodynamics of Angular Propulsion in Fluids," *Physical Review Letters*, vol. 109, p. 54504, 8 2012.

[47] J. J. Van Deemter, "On the theory of the Ranque-Hilsch cooling effect," *Applied Scientific Research*, vol. 3, pp. 174–196, 5 1952.

[48] R. G. Deissler and M. Perlmutter, "Analysis of the flow and energy separation in a turbulent vortex," *International Journal of Heat and Mass Transfer*, vol. 1, pp. 173–191, 1960.

[49] W. S. Lewellen, "A solution for three-dimensional vortex flows with strong circulation," *Journal of Fluid Mechanics*, vol. 14, no. 3, pp. 420–432, 1962.

[50] H. A. Einstein and H. Li, "Steady vortex flow in a real fluid," in *Proc. Heat Transfer and Fluid Mechanics Institute*, (Stanford, CA), pp. 33–43, 1951.

[51] C. d. P. Donaldson and R. D. Sullivan, "Examination of the solutions of the Navier-Stokes equations for a class of three-dimensional vortices. part I. Velocity distributions for steady motion," tech. rep., Aeronautical Research Associates of Princeton, Princeton, N. J., 1960.

[52] C. U. Linderstrøm-Lang, "The three-dimensional distributions of tangential velocity and total-temperature in vortex tubes," *Journal of Fluid Mechanics*, vol. 45, no. 1, pp. 161–187, 1971.

[53] A. J. Reynolds, "Energy flows in a vortex tube," *ZAMP Zeitschrift fur Angewandte Mathematik und Mechanik*, vol. 12, no. 4, pp. 343–357, 1961.

[54] W. Fröhlingsdorf and H. Unger, "Numerical investigations of the compressible flow and the energy separation in the Ranque-Hilsch vortex tube," *International Journal of Heat and Mass Transfer*, vol. 42, no. 3, pp. 415–422, 1998.

[55] H. A. Kandil and S. T. Abdelghany, "Computational investigation of different effects on the performance of the Ranque-Hilsch vortex tube," *Energy*, vol. 84, pp. 207–218, 2015.

[56] B. Ahlborn, J. U. Keller, R. Staudt, G. Treitz, and E. Rebhan, "Limits of temperature separation in a vortex tube," *Journal of Physics D: Applied Physics*, vol. 27, no. 3, pp. 480–488, 1994.

[57] Y. Xue, M. Arjomandi, and R. Kelso, "Experimental study of the flow structure in a counter flow Ranque-Hilsch vortex tube," *International Journal of Heat and Mass Transfer*, vol. 55, no. 21-22, pp. 5853–5860, 2012.

[58] X. Guo, B. Zhang, L. Li, B. Liu, and T. Fu, "Experimental investigation of flow structure and energy separation of Ranque–Hilsch vortex tube with LDV measurement," *International Journal of Refrigeration*, vol. 101, no. May, pp. 106–116, 2019.

[59] G. J. Ranque, "Experiments on expansion in a vortex with simultaneous exhaust of hot air and cold air," *J. Phys. Radium*, vol. 4, no. 7, pp. 112–114, 1933.

[60] Kurosaka M, "Acoustic streaming in swirling flow and the Ranque-Hilsch (vortex-tube) effect," *Journal of Fluid Mechanics*, vol. 124, no. 1982, pp. 139–172, 1982.

[61] Y. Xue, M. Arjomandi, and R. Kelso, "A critical review of temperature separation in a vortex tube," *Experimental Thermal and Fluid Science*, vol. 46, no. 8, pp. 175–182, 2010.

[62] H. Kuroda, *An Experimental Study of Swirling Flow in Pipes*. PhD thesis, University of Tennessee - Knoxville, 1983.

[63] R. Liew, J. C. H. Zeegers, J. G. M. Kuerten, and W. R. Michalek, "Maxwell's demon in the ranque-hilsch vortex tube," *Physical Review Letters*, vol. 109, no. 5, pp. 3–6, 2012.

[64] B. Ahlborn, J. Camire, and J. U. Keller, "Low-pressure vortex tubes," *Journal of Physics D: Applied Physics*, vol. 29, no. 6, pp. 1469–1472, 1999.

[65] Y. Xue, M. Arjomandi, and R. Kelso, "The working principle of a vortex tube," *International Journal of Refrigeration*, vol. 36, no. 6, pp. 1730–1740, 2013.

[66] Y. Xue, M. Arjomandi, and R. Kelso, "Experimental study of the thermal separation in a vortex tube," *Experimental Thermal and Fluid Science*, vol. 46, pp. 175–182, 2013.

[67] Y. Xue, M. Arjomandi, and R. Kelso, "Energy analysis within a vortex tube," *Experimental Thermal and Fluid Science*, vol. 52, pp. 139–145, 2014.

[68] H. R. Thakare and A. D. Parekh, "Computational analysis of energy separation in counter-flow vortex tube," *Energy*, vol. 85, pp. 62–77, 2015.

[69] S. E. Rafiee and M. M. Sadeghiazad, "Experimental study and 3D CFD analysis on the optimization of throttle angle for a convergent vortex tube," *Journal of Marine Science and Application*, vol. 15, no. 4, pp. 388–404, 2016.

[70] V. Bianco, A. Khait, A. Noskov, and V. Alekhin, "A comparison of the application of RSM and LES turbulence models in the numerical simulation of thermal and flow patterns in a double-circuit Ranque-Hilsch vortex tube," *Applied Thermal Engineering*, vol. 106, pp. 1244–1256, 2016.

[71] U. Behera, P. J. Paul, S. Kasthurirengan, R. Karunanithi, S. N. Ram, K. Dinesh, and S. Jacob, "CFD analysis and experimental investigations towards optimizing the parameters of Ranque-Hilsch vortex tube," *International Journal of Heat and Mass Transfer*, vol. 48, no. 10, pp. 1961–1973, 2005.

[72] T. Dutta, K. P. Sinhamahapatra, and S. S. Bandyopadhyay, "CFD Analysis of Energy Separation in Ranque-Hilsch Vortex Tube at Cryogenic Temperature," *Journal of Fluids*, vol. 2013, pp. 1–14, 2013.

[73] A. Dhillon and S. Bandyopadhyay, "CFD analysis of straight and flared vortex tube," *IOP Conference Series: Materials Science and Engineering*, vol. 101, no. 1, 2015.

[74] R. Shamsoddini and B. Abolpour, "A geometric model for a vortex tube based on numerical analysis to reduce the effect of nozzle number," *International Journal of Refrigeration*, vol. 94, pp. 49–58, 10 2018.

[75] C. M. Gao, K. J. Bosschaart, J. C. H. Zeegers, and A. T. A. M. De Waele, "Experimental study on a simple Ranque-Hilsch vortex tube," *Cryogenics*, vol. 45, no. 3, pp. 173–183, 2005.

[76] Y. Xue and M. Arjomandi, "The effect of vortex angle on the efficiency of the Ranque–Hilsch vortex tube," *Experimental Thermal and Fluid Science*, vol. 33, no. 1, pp. 54–57, 2008.

[77] C. Morsbach, D. Schl, U. Doll, E. Burow, M. Beversdorff, G. Stockhausen, and C. Willert, "The Flow Field Inside a Ranque-Hilsch Vortex Tube Part II : Turbulence Modelling and Numerical Simulation Numerical Method and Test Case," in *International Symposium on Turbulence and Shear Flow Phenomena*, (Melbourne, Australia), pp. 1–6, 2015.

[78] U. Behera, P. J. Paul, K. Dinesh, and S. Jacob, "Numerical investigations on flow behaviour and energy separation in Ranque-Hilsch vortex tube," *International Journal of Heat and Mass Transfer*, vol. 51, no. 25-26, pp. 6077–6089, 2008.

[79] C.-Y. Wang, "On a Class of Exact Solutions of the Navier-Stokes Equations," *Journal of Applied Mechanics*, vol. 33, pp. 696–698, 9 1966.

Chapter 2

Compressible and Choked Flows in Rotating Passages

Nomenclature

Roman Symbols

A Duct or passage cross-sectional area

a Independent parameter

$A^*_{\text{Ch}} = A*_r /A*_t$ Critical cross-sectional area profile

$A^*_t = A/A_t$ Area to throat area ratio in a stationary passage

C, D, E Constants of integration

c_p Isobaric heat capacity

c_v Volumetric heat capacity

$\dot{E}_{\text{st}}$ Transient energy storage in a control volume

$h = \xi + p/\rho$ Specific enthalpy

$i = \sqrt{-1}$

$\hat{\mathbf{i}}, \hat{\mathbf{j}}, \hat{\mathbf{k}}$ Unit vectors aligned with the x, y, and z axes, respectively

$\dot{m}$ Mass flow rate

$\dot{m}_{\text{Ch}}$ Maximum (choked) mass flow rate

$\dot{m}_{\text{Ch, min}}$ Minimum choked mass flow rate; occurs at the location in a duct or passage which will choke first if the mass flow rate is slowly increased.

p Thermodynamic pressure

p pressure

$\mathbf{p}^*$ Parameterized position vector

R_s Specific ideal gas constant

T static temperature

$T_0 = T + \frac{u^2}{2c_p}$ Total temperature

$\mathbf{t}$ Unit tangent vector to a parametric curve $\mathbf{p}^*$

$\mathbf{u}$ Velocity

$\bar{u}$ Flow speed along along a constrained path

$\mathbf{x}$ Position vector

X, Y, Z Components of position vector

x, y, z Cartesian co-ordinates

Greek Symbols

$\gamma = \frac{c_p}{c_v}$ Ratio of specific heats

$\boldsymbol{\nabla}$ Gradient operator

ξ specific internal energy

ρ fluid density

ϕ Arbitrary scalar or vector quantity

$\bar{\phi}_0$ Stagnation quantity

$\boldsymbol{\Omega}$ Angular velocity of rotating frame

Dimensionless Groups

$Ma^2 = \frac{u_c^2}{\gamma R_s T_c}$ Global Mach number

$Ma_S = \frac{u_2}{\sqrt{\gamma R_s \bar{T}_2}}$ Shroud Mach number

$Ma_L = \frac{\hat{u}}{\sqrt{\gamma R_s \bar{T}}}$ Local Mach number

$Ma_t = \frac{\Omega_c x_c}{\sqrt{\gamma R_s \bar{T}_0}}$ Tip Mach number

Ma_t^* Modified tip Mach number ratio

$Ro = \frac{u_c}{\Omega_c x_c}$ Rossby number

Superscripts

$*$ Non-dimensional quantity

Subscripts

1 Quantity at boundary nearest to the center of rotation

2 Quantity at boundary furthest from the center of rotation

c Characteristic dimension

in Quantity entering a control volume

out Quantity exiting a control volume

Other Symbols

$'$ Derivative of single-variable function

$\hat{}$ Quantity in non-stationary frame

Acronyms

1D One-dimensional

CFD Computational Fluid Dynamics

CFD Computational Fluid Dynamics

RHVT Ranque-Hilsch Vortex Tube

RHVT Ranque-Hilsch Vortex Tube

RHS Right Hand Side

2.1 Introduction

In two recent publications Polihronov and Straatman [1, 2] have applied heuristic techniques to examine the energetics of confined fluid flow in a rotating reference frame. These works were completed in an effort to shed new light on the temperature separation phenomenon within the Ranque-Hilshe Vortex Tube (RHVT), first discovered by Ranque [3]. Presently, the literature contains no widely accepted explanation of the temperature separation phenomenon as noted in a recent review by Thakare et al. [4], but a fundamental understanding of rotating compressible flows appears to be a promising starting point.

Studies of rotating flows may be divided into two broad categories: flows through rotating passages, and swirling flows. Both types of flows share similar features, but the latter comes with increased complexity. We emphasize that the present work focuses on flows through rotating passages, and will tackle swirling flows in future publications. Rotating incompressible flows in confined passages have been studied extensively, both analytically and numerically. An initial treatment of rotating flows has been provided by Greenspan [5], and later textbooks have offered additional perspectives [6, 7, 8]. More recent work has focused on two and three-dimensional flow within rotating passages. Tatro and Mollo-Christensen [9] have studied the Ekman layers at low Rossby number flows experimentally, noting the presence of type I and type II instabilities. Kristofferson and Andersson [10] have employed direct numerical simulations to study turbulent boundary layer flows inside rotating passages, finding the variation in mean velocity profiles with changes in Rossby number. Khesghi and Scriven [11] have used the finite element method to study rotating flows when neither the Ekman nor the Rossby numbers may be neglected, and revealed the presence of an inviscid core flow near the axis of the straight passage.

Outside of the publications by Polihronov and Straatman, rotating *compressible* flows in

confined passages have received attention from a variety of research fields. Most notably, Seymour Lieblein submitted a NACA Technical Note in 1952 [12] wherein he developed a set of equations describing compressible flow in radial compressor blade passages, including a discussion of supersonic flow and the effects of losses. In later publications, it has become popular to define the rothalpy of a compressible fluid undergoing radial motion, wherein the rothalpy has been shown to be constant when the flow may be considered adiabatic and frictionless [13, 14]. Bosman [15] later showed that, for 'all engineering intents and purposes', the error associated with the constant rothalpy assumption may be neglected. Discussions of rothalpy now appear in graduate level fluid mechanics texts such as Refs. [7, 8].

The objective of the present work is to re-analyze the rotating duct problem studied by Polihronov and Straatman, starting instead from the governing equations of fluid mechanics. We will systematically obtain closed form mathematical expressions for the density, temperature, pressure, and velocity profiles within rotating, one-dimensional, straight and curved passages with constant and spatially varying cross-sectional areas, under the assumption that the flow is compressible, adiabatic, and invscid. The motivation for this work is to gain insight from the solutions about the mechanism responsible for the temperature separation phenomenon in the RHVT.

2.2 Governing Equations

The conservation equations of mass, momentum, and energy have been appropriately transformed into a general, non-inertial reference frame by Combrinck and Dala [16] by applying the Galilean transformation technique to the stationary conservation equations as suggested by Kageyama and Hyodo [17]. Here we work only with the steady forms of these equations. The conservation of mass is

$$\boldsymbol{\nabla} \cdot (\rho \hat{\mathbf{u}}) = 0, \tag{2.1}$$

where $\hat{\mathbf{u}}$ is the velocity in the rotating and accelerating reference frame, ρ is the density, and $\boldsymbol{\nabla}$ is the gradient operator. The inviscid, steady, conservation of momentum equation in a non-accelerating rotating frame in the absence of body forces is

$$(\hat{\mathbf{u}} \cdot \boldsymbol{\nabla})\,\hat{\mathbf{u}} = -\frac{\boldsymbol{\nabla} p}{\rho} + \underbrace{2\hat{\mathbf{u}} \times \boldsymbol{\Omega}}_{\substack{\text{Coriolis} \\ \text{acceleration}}} \underbrace{- (\hat{\mathbf{x}} \times \boldsymbol{\Omega}) \times \boldsymbol{\Omega}}_{\substack{\text{centrifugal} \\ \text{acceleration}}}, \tag{2.2}$$

where p is the thermodynamic pressure, $\boldsymbol{\Omega}$ is the angular velocity of the frame (which can be unsteady in general), and $\hat{\mathbf{x}}$ is the position vector. $\hat{\mathbf{x}}$ is defined relative to the origin of a coordinate system about which rotation occurs. When heat conduction and external heat sources may be neglected, the conservation of internal energy is

$$\rho \hat{\mathbf{u}} \cdot \boldsymbol{\nabla} \xi = -p\,(\boldsymbol{\nabla} \cdot \hat{\mathbf{u}})\,, \tag{2.3}$$

where ξ is the specific internal energy. Notice only the velocity vector $\hat{\mathbf{u}}$ and the position vector $\hat{\mathbf{x}}$ have been assigned the ˆ symbol. This emphasizes that these quantities are transformed versions of their stationary frame counterparts. All other quantities under consideration are scalars, which are not affected by the transformation into the rotating frame, so the distinction between scalar quantities in the rotating frame and their counterparts in the stationary frame is not made. The inviscid and non-heat-conducting assumptions are made for two reasons: the solutions are simplified considerably, and (as it will be seen below) it is plainly shown that steady cooling is possible in the absence of viscous forces and internal heat transfer.

2.2.1 Auxillary equations

All fluids analyzed in this work are characterized by the ideal gas equation of state:

$$p = \rho R_s T, \tag{2.4}$$

where R_s is the specific gas constant, and T is the static, absolute temperature.

We will further assume the heat capacities are constant, so that the internal energy and enthalpy may be respectively written as

$$\varepsilon = c_v T, \tag{2.5}$$

$$h = c_p T, \tag{2.6}$$

where c_v is the volumetric heat capacity and c_p is the isobaric heat capacity. Fluids which obey the ideal gas law and have constant heat capacities are called perfect gases [18].

2.2.2 Nondimensionalization

To further generalize our results we have presented much of our analyses and solutions in terms of non-dimensional quantities. We use the following scaled variables to non-dimensionalize the governing and auxillary equations:

$$\hat{\mathbf{x}}^* = \frac{\hat{\mathbf{x}}}{x_c} \quad \hat{\mathbf{u}}^* = \frac{\hat{\mathbf{u}}}{u_c} \quad p^* = \frac{p}{\rho_c x_c u_c \Omega_c} \quad \boldsymbol{\Omega}^* = \frac{\boldsymbol{\Omega}}{\Omega_c} \quad T^* = \frac{T}{T_c} \quad \rho^* = \frac{\rho}{\rho_c} \quad \boldsymbol{\nabla}^* = x_c \boldsymbol{\nabla}$$

Assuming the fluid is a perfect gas, the mass, momentum, and energy equations become

$$\boldsymbol{\nabla}^* \cdot (\rho^* \hat{\mathbf{u}}^*) = 0, \tag{2.7}$$

$$Ro\,(\hat{\mathbf{u}}^* \cdot \boldsymbol{\nabla}^*)\,\hat{\mathbf{u}}^* = -\frac{\boldsymbol{\nabla}^* p^*}{\rho^*} + 2\hat{\mathbf{u}}^* \times \boldsymbol{\Omega}^* - \frac{1}{Ro}\,(\hat{\mathbf{x}}^* \times \boldsymbol{\Omega}^*) \times \boldsymbol{\Omega}^*, \tag{2.8}$$

$$\rho^* Ro \hat{\mathbf{u}}^* \cdot \boldsymbol{\nabla}^* T^* = -\gamma(\gamma - 1) Ma^2 p^*\,(\boldsymbol{\nabla}^* \cdot \hat{\mathbf{u}}^*)\,, \tag{2.9}$$

where the relevant dimensionless groups are defined in table 2.1.

Table 2.1: Relevant dimensionless groups

$Ro = \dfrac{u_c}{\Omega_c x_c}$	Rossby number
$Ma^2 = \dfrac{u_c^2}{\gamma R_s T_c}$	Mach number
$\gamma = \dfrac{c_p}{c_v}$	heat capacity ratio

Using the same scaled variables the ideal gas equation 2.4 becomes

$$p^* = \frac{Ro}{\gamma Ma^2} \rho^* T^*. \tag{2.10}$$

2.3 Rotating Duct

This section derives the general solution for compressible flow inside a rotating duct under the following assumptions:

1. constant thermophysical properties,
2. steady rotation about the z-axis: $\mathbf{\Omega} = \omega\hat{\mathbf{k}}$,
3. steady flow,
4. subsonic flow,
5. unidirectional flow along the $\hat{x}$-axis such that $\hat{\mathbf{u}} = \hat{u}\hat{\mathbf{i}}$,
6. inviscid,
7. adiabatic, and
8. negligible heat conduction.

Based on these assumptions we have neglected any influences listed by Lyman [14] which may change the rothalpy inside the duct. A schematic of the duct under consideration is shown in Fig. 2.1.

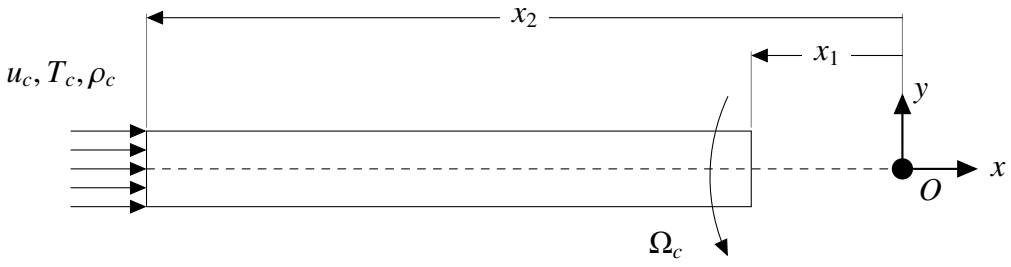

Figure 2.1: Schematic of the constant cross-section duct, rotating with a constant angular velocity about the origin O. Here the flow is shown moving from the outer position 2 to the inner position 1, however our analysis is independent of the flow direction. Furthermore, while we have chosen characteristic quantities at position 2, the choice is arbitrary, as long as they are all at the same location.

2.3.1 Constant cross-section

If the cross-sectional area of the duct is constant, the steady, non-dimensional conservation equations of mass, momentum, and energy reduce to

$$\hat{u}^* \frac{\mathrm{d}\rho^*}{\mathrm{d}\hat{x}^*} + \rho^* \frac{\mathrm{d}\hat{u}^*}{\mathrm{d}\hat{x}^*} = 0, \tag{2.11}$$

$$Ro\, \hat{u}^* \frac{\mathrm{d}\hat{u}^*}{\mathrm{d}\hat{x}^*} = -\frac{1}{\rho^*} \frac{\mathrm{d}p^*}{\mathrm{d}\hat{x}^*} + \frac{\hat{x}^*}{Ro}, \tag{2.12}$$

$$0 = -2\hat{u}^* + \frac{1}{Fr^2} \frac{\hat{f}^*}{\rho^*}, \tag{2.13}$$

$$Ro\, \rho^* \hat{u}^* \frac{\mathrm{d}T^*}{\mathrm{d}\hat{x}^*} = -\gamma(\gamma - 1) Ma^2 p^* \frac{\mathrm{d}\hat{u}^*}{\mathrm{d}\hat{x}^*}. \tag{2.14}$$

Use of the ideal gas law allows equations 2.11 and 2.14 to be simplified and solved through direct integration.

$$\rho^* = \frac{C}{\hat{u}^*}, \tag{2.15}$$

$$T^* = \frac{D}{\hat{u}^{*\gamma-1}}, \tag{2.16}$$

where C and D are constants of integration. The pressure distribution is therefore given by

$$p^* = \frac{Ro}{\gamma Ma^2} \frac{CD}{\hat{u}^{*\gamma}}. \tag{2.17}$$

Solving equation 2.12 requires substitution of 2.15 and 2.17 to obtain the differential equation

$$\hat{u}^* \frac{\mathrm{d}\hat{u}^*}{\mathrm{d}\hat{x}^*} = \frac{1}{Ma^2} \frac{D}{\hat{u}^{*\gamma}} \frac{\mathrm{d}\hat{u}^*}{\mathrm{d}\hat{x}^*} + \frac{\hat{x}^*}{Ro^2}, \tag{2.18}$$

whose solution is

$$\frac{\hat{u}^{*2}}{2} + \frac{1}{(\gamma - 1)Ma^2} \frac{D}{\hat{u}^{*\gamma-1}} - \frac{\hat{x}^{*2}}{2Ro^2} = E. \tag{2.19}$$

Equation 2.19 is an expression of Bernoulli's theorem in a rotating framework. Inserting the boundary conditions $T^*(-1) = 1$, and $\hat{u}^*(-1) = 1$ yields

$$T^* = \frac{1}{\hat{u}^{*\gamma-1}}, \tag{2.20}$$

$$\frac{1}{2}\left(\hat{u}^{*2}-1\right) + \frac{1}{(\gamma-1)Ma^2}\left(\frac{1}{\hat{u}^{*\gamma-1}}-1\right) - \frac{1}{2Ro^2}\left(\hat{x}^{*2}-1\right) = 0. \tag{2.21}$$

It is interesting to note that the velocity and temperature profiles are completely independent of the pressure and density. Only the inlet temperature and velocity boundary conditions influence the solution. Equation 2.21 may also be re-dimensionalized for better understanding of each of the terms:

$$\underbrace{\frac{\hat{u}^2-\hat{u}_c^2}{2}}_{\substack{\text{linear}\\ \text{kinetic energy}}} + \underbrace{c_p\left(T-T_c\right)}_{\text{enthalpy}} - \underbrace{\frac{\omega^2\left(\hat{x}^2-x_c^2\right)}{2}}_{\substack{\text{rotational}\\ \text{kinetic energy}}} = 0. \tag{2.22}$$

When the Mach and Rossby numbers are very small, the linear kinetic energy term in equation 2.21 may be neglected and the temperature profile reduces to

$$T^* = 1 - \frac{(\gamma-1)Ma^2}{2Ro^2}\left(1-\hat{x}^{*2}\right). \tag{2.23}$$

Re-dimensionalizing equation 2.23 and evaluating at $\hat{x} = 0$ yields the temperature distribution found by Polihronov and Straatman [1]:

$$T_c - T = \frac{\omega^2 x_c^2}{2c_p}. \tag{2.24}$$

This indicates their analysis has implicitly assumed the compressibility of the fluid is small, and the rotational energy of the fluid is large.

We have performed several computational fluid dynamics (CFD) simulations of rotating duct model using ANSYS-CFX © software [19] to demonstrate the accuracy of equations 2.16 and 2.19 over equation 2.23. A 1D mesh was generated for a straight square duct containing 10^3 evenly spaced grid points. Air was chosen as the working fluid, with a heat capacity ratio $\gamma = 1.4$, and a free slip boundary condition was enforced at each of the duct walls. The average residuals for the solution were converged within 10^{-4}. The results are shown in Fig. 2.2. A maximum error of 0.03% was observed between equation 2.19 and the CFD velocity profile, and a maximum error of 5×10^{-4} % was observed between equation 2.16 and the CFD temperature profile.

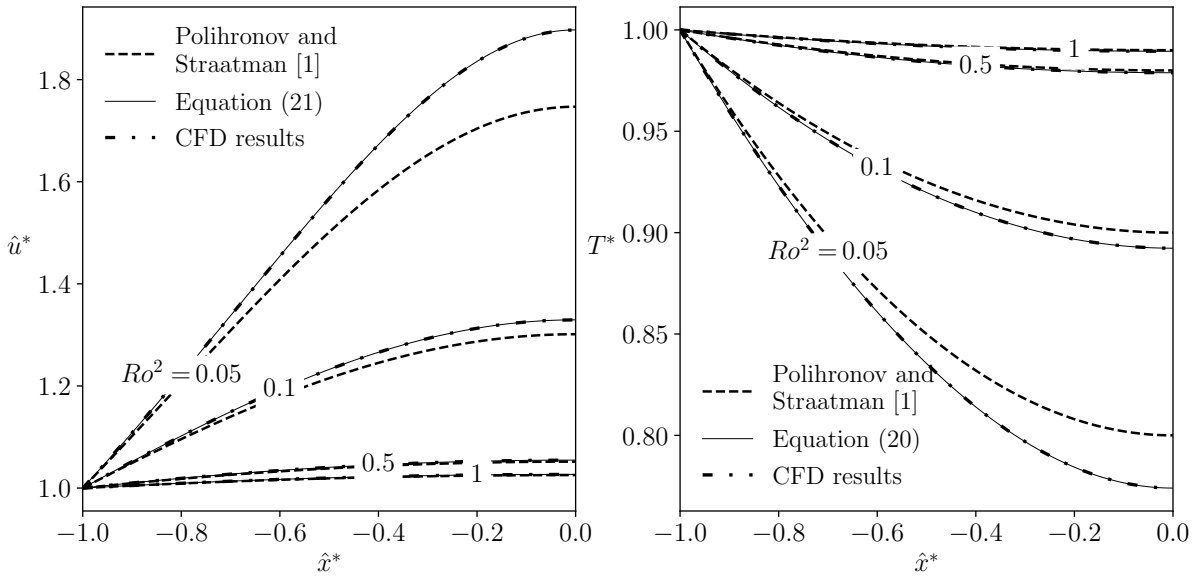

Figure 2.2: Plots of non-dimensional velocity and temperature in a straight duct with $Ma^2 = 0.05$ and $\gamma = 1.4$.

2.3.2 Arbitrary cross-sectional area

We will now generalize the above results to a duct of varying cross section $A(\hat{x})$. Analyzing a thin slice $\mathrm{d}\hat{x}$ of a straight duct aligned with the $\hat{x}$ axis where the free-slip boundary condition is applied at the duct walls leads to the following governing equations:

$$\frac{1}{\rho}\frac{\mathrm{d}\rho}{\mathrm{d}\hat{x}} + \frac{1}{A}\frac{\mathrm{d}A}{\mathrm{d}\hat{x}} + \frac{1}{\hat{u}}\frac{\mathrm{d}\hat{u}}{\mathrm{d}\hat{x}} = 0, \tag{2.25}$$

$$\hat{u}\frac{\mathrm{d}\hat{u}}{\mathrm{d}\hat{x}} = -\frac{1}{\rho}\frac{\mathrm{d}p}{\mathrm{d}\hat{x}} + x\omega^2, \tag{2.26}$$

$$c_v\frac{\mathrm{d}T}{\mathrm{d}\hat{x}} = -\frac{p}{\rho}\left(\frac{1}{A}\frac{\mathrm{d}A}{\mathrm{d}\hat{x}} + \frac{1}{\hat{u}}\frac{\mathrm{d}\hat{u}}{\mathrm{d}\hat{x}}\right). \tag{2.27}$$

Invoking the ideal gas equation 2.10, introducing the scaled cross-sectional area $A^*(\hat{x}^*) = A(\hat{x})/A_c$, and non-dimensionalizing 2.25 - 2.27 yields:

$$\frac{1}{\rho^*}\frac{\mathrm{d}\rho^*}{\mathrm{d}\hat{x}^*} + \frac{1}{A^*}\frac{\mathrm{d}A^*}{\mathrm{d}\hat{x}^*} + \frac{1}{\hat{u}^*}\frac{\mathrm{d}\hat{u}^*}{\mathrm{d}\hat{x}^*} = 0, \tag{2.28}$$

$$Ro\hat{u}^*\frac{\mathrm{d}\hat{u}^*}{\mathrm{d}\hat{x}^*} = -\frac{1}{\rho^*}\frac{\mathrm{d}p^*}{\mathrm{d}\hat{x}^*} + \frac{\hat{x}^*}{Ro}, \tag{2.29}$$

$$\frac{1}{T^*}\frac{\mathrm{d}T^*}{\mathrm{d}\hat{x}^*} = -(\gamma-1)\left(\frac{1}{A^*}\frac{\mathrm{d}A^*}{\mathrm{d}\hat{x}^*} + \frac{1}{\hat{u}^*}\frac{\mathrm{d}\hat{u}^*}{\mathrm{d}\hat{x}^*}\right). \tag{2.30}$$

Equations 2.28 and 2.30 may be solved by direct integration, and equation 2.10 may be used to obtain an expression for the pressure distribution:

$$\rho^* = \frac{C}{A^*\hat{u}^*}, \tag{2.31}$$

$$T^* = \frac{D}{(A^*\hat{u}^*)^{\gamma-1}}, \tag{2.32}$$

$$p^* = \frac{Ro}{\gamma Ma^2}\frac{CD}{(A^*\hat{u}^*)^{\gamma}}. \tag{2.33}$$

Solving equation 2.29 requires the use of equations 2.31 and 2.33 to obtain

$$\left(\hat{u}^* - \frac{D}{Ma^2}\frac{1}{(A^*\hat{u}^*)^{\gamma-1}\,\hat{u}^*}\right)\frac{\mathrm{d}\hat{u}^*}{\mathrm{d}\hat{x}^*} - \frac{D}{Ma^2}\frac{1}{(A^*\hat{u}^*)^{\gamma-1}A^*}\frac{\mathrm{d}A^*}{\mathrm{d}\hat{x}^*} - \frac{\hat{x}^*}{Ro^2} = 0. \tag{2.34}$$

Equation 2.34 may be solved using the method of exact differentials, yielding

$$\frac{\hat{u}^{*2}}{2} + \frac{1}{Ma^2(\gamma-1)}\frac{D}{(\hat{u}^*A^*)^{\gamma-1}} - \frac{\hat{x}^{*2}}{2Ro^2} = E. \tag{2.35}$$

Three boundary conditions are required to evaluate constants C, D and E. If the duct area is constant (i.e. $A(\hat{x}) = A_c$) then $A^* = 1$ and equations 2.31, 2.32, 2.33 and 2.35 reduce to the solutions for a constant cross-section duct; equations 2.15, 2.16, 2.17 and 2.19 respectively. In addition, we note that equation 2.35 is in complete agreement with equation 9 in Ref. [12].

To confirm this result, we have conducted several CFD simulations and compared the computed profiles to equations 2.32 and 2.35. These simulations were similar to those described in section 2.3.1 unless otherwise noted. The geometry under consideration is the straight square duct depicted in Fig. 2.3 whose cross-sectional area is given by

$$A^*(\hat{x}^*) = (3|\hat{x}^*| + 4)^2\,. \tag{2.36}$$

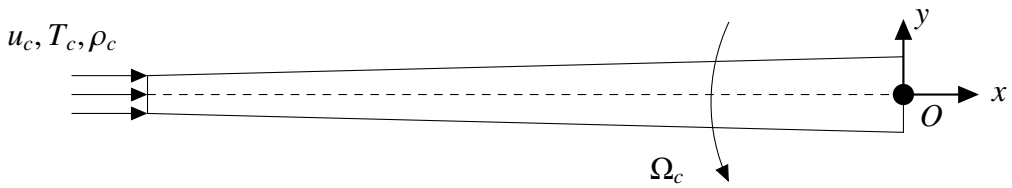

Figure 2.3: Schematic of the varying cross-section duct, rotating with a constant angular velocity Ω_c about the origin O. The area as a function of the $\hat{x}$ co-ordinate is given by equation 2.36.

A 1D mesh of constant grid spacing with 10^3 grid points was generated. The solution was again computed using ANSYS CFX © [19]. Solutions were converged when the average residuals were reduced below 10^{-4}. The results have been plotted in Fig. 2.4. A maximum error of 0.6% was observed between equation 2.35 and the CFD results while a maximum error of 0.004% was observed between equation 2.32 and the CFD results.

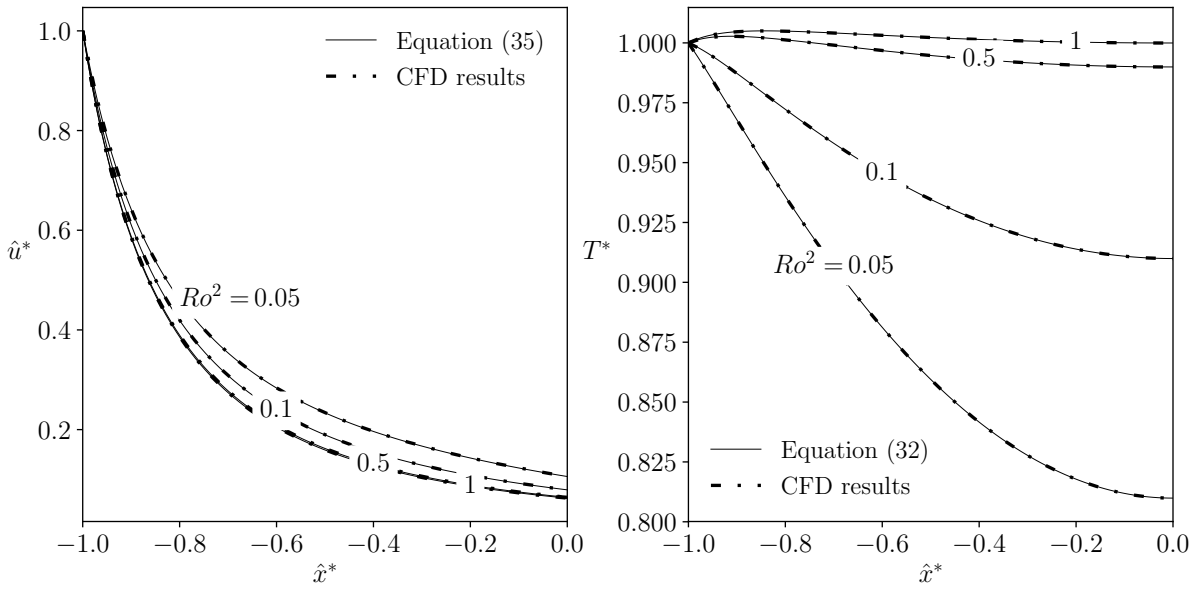

Figure 2.4: Plots of non-dimensional velocity and temperature of a duct with cross-sectional area varying in accordance with 2.36 with $Ma^2 = 0.05$ and $\gamma = 1.4$.

2.4 Rotating Passage

In this section we will further generalize the above results to an arbitrarily curved passage defined by the parameterization

$$\mathbf{p}(a) = X(a)\hat{\mathbf{i}} + Y(a)\hat{\mathbf{j}} + Z(a)\hat{\mathbf{k}}. \tag{2.37}$$

and the scaled path vector is given by $\mathbf{p}^* = \mathbf{p}/x_c$. The components of $\mathbf{p}$ may be any well-behaved functions, producing, for example, the path shown in Fig. 2.5.

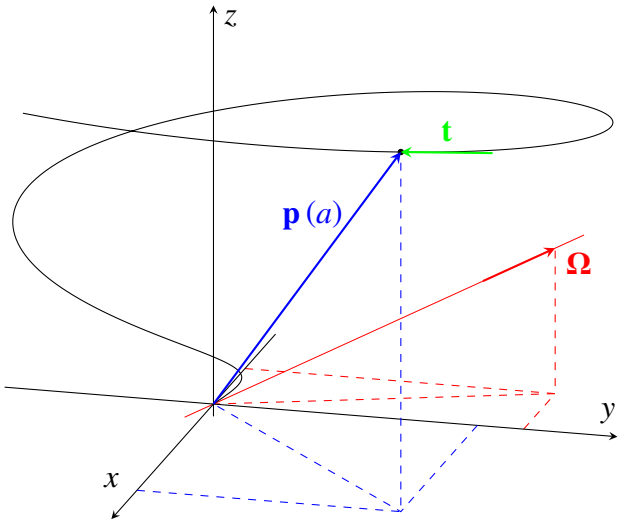

Figure 2.5: An arbitrary path defined by $\mathbf{p}(a)$, rotating about $\boldsymbol{\Omega}$.

The following derivation requires that the axis of rotation contains the origin of the coordinate system on which $\mathbf{p}^*$ is defined. The unit tangent vector parallel to the path $\mathbf{p}$ is given by

$$\mathbf{t} = \frac{\mathbf{p}'(a)}{\|\mathbf{p}'(a)\|} = \frac{\mathbf{p}^{*\prime}(a)}{\|\mathbf{p}^{*\prime}(a)\|}. \tag{2.38}$$

Similarly to the previous derivations, we will neglect the velocity variation across the duct, and assume the velocity at each point is parallel to the unit tangent vector:

$$\frac{\hat{\mathbf{u}}^*}{\bar{u}^*} = \mathbf{t}, \tag{2.39}$$

where $\bar{u}^* = \|\hat{\mathbf{u}}^*\|$.

2.4.1 Constant cross-section

The following steps apply when the duct cross-sectional area is constant along the path. If we have some quantity $\phi(\mathbf{p}^*(a))$, its total derivative is

$$\frac{\mathrm{d}\phi}{\mathrm{d}a} = \frac{\partial\phi}{\partial x}\frac{\mathrm{d}x}{\mathrm{d}a} + \frac{\partial\phi}{\partial y}\frac{\mathrm{d}y}{\mathrm{d}a} + \frac{\partial\phi}{\partial z}\frac{\mathrm{d}z}{\mathrm{d}a} = \boldsymbol{\nabla}\phi \cdot \mathbf{p}^{*\prime}(a) = \left(\mathbf{p}^{*\prime}(a) \cdot \boldsymbol{\nabla}\right)\phi. \tag{2.40}$$

Furthermore, given that all quantities are defined only on the path $\mathbf{p}(a)$, any gradient (e.g. $\boldsymbol{\nabla}\phi$) is parallel to the unit tangent vector:

$$\boldsymbol{\nabla}\phi = c\frac{\mathrm{d}\phi}{\mathrm{d}a}\mathbf{t}, \tag{2.41}$$

for some unknown value c. We will choose $c = 1/\|\mathbf{p}^{*\prime}(a)\|$ to satisfy equation 2.40. Substituting equations 2.39 and 2.41 into the governing equations 2.7 and 2.9 yields (after some manipulation)

$$\frac{1}{\rho^*}\frac{\mathrm{d}\rho^*}{\mathrm{d}a} + \frac{1}{\bar{u}^*}\frac{\mathrm{d}\bar{u}^*}{\mathrm{d}a} = 0, \tag{2.42}$$

$$\frac{1}{T^*}\frac{\mathrm{d}T^*}{\mathrm{d}a} + \frac{(\gamma-1)}{\bar{u}^*}\frac{\mathrm{d}\bar{u}^*}{\mathrm{d}a} = 0. \tag{2.43}$$

$$\left(\bar{u}^* + \frac{D}{\gamma Ma^2 \bar{u}^{*\gamma}}\right)\frac{Ro}{\|\mathbf{p}^{*\prime}\|}\frac{\mathrm{d}\bar{u}^*}{\mathrm{d}a}\mathbf{t} + \frac{Ro}{\|\mathbf{p}^{*\prime}\|}\bar{u}^{*2}\mathbf{t}' = 2\bar{u}^*\left(\mathbf{t} \times \boldsymbol{\Omega}^*\right) + \frac{1}{Ro}\left[\mathbf{p}^* - \left(\mathbf{p}^* \cdot \boldsymbol{\Omega}^*\right)\boldsymbol{\Omega}^*\right]. \tag{2.44}$$

Solving 2.42 and 2.43 yields equations 2.15 and 2.16, respectively. The ideal gas law may be expressed using equation 2.17.

To obtain a general solution for the velocity profile we will take the dot product of equation 2.44 with $\mathbf{t}$. Since $\mathbf{t}$ and $\mathbf{t}'$ are orthogonal, the second term on the left hand side must vanish. Furthermore, the first term on the right hand side also evaluates to zero, since it contains a triple scalar product with two parallel vectors. The remaining equation is given by

$$\left(\bar{u}^* + \frac{D}{\gamma Ma^2 \bar{u}^{*\gamma}}\right)\frac{\mathrm{d}\bar{u}^*}{\mathrm{d}a} = \frac{g'(a)}{Ro^2}, \tag{2.45}$$

where

$$g'(a) = \mathbf{p}^* \cdot \mathbf{p}^{*\prime} - (\mathbf{p}^* \cdot \mathbf{\Omega}^*)(\mathbf{p}^{*\prime} \cdot \mathbf{\Omega}^*). \tag{2.46}$$

Equation 2.45 may be solved using direct integration:

$$\frac{\bar{u}^{*2}}{2} + \frac{1}{(\gamma-1)Ma^2}\frac{D}{\bar{u}^{*\gamma-1}} - \frac{g(a)}{Ro^2} = E. \tag{2.47}$$

2.4.2 Arbitrary cross-sectional area

For a rotating passage of arbitrarily varying cross-sectional area $A(a)$, and $A^*(a) = A(a)/A_c$ we must include $A^*(a)$ in a manner similar to section 2.3.2. The density, temperature, and pressure profiles are given by equations 2.31, 2.32, and 2.33, respectively. The velocity profile is given by

$$\frac{\bar{u}^{*2}}{2} + \frac{1}{(\gamma-1)Ma^2}\frac{D}{(\bar{u}^* A^*)^{\gamma-1}} - \frac{g(a)}{Ro^2} = E. \tag{2.48}$$

2.4.3 Radius as the parameter

In light of this result, we are interested to see if we can make any statements about the function $g(a)$. Consider the following arbitrary curve in a cylindrical co-ordinate system whose z-axis is coincident with the axis of rotation:

$$\theta = \theta(r), \tag{2.49}$$

$$z = \zeta(r, \theta(r)). \tag{2.50}$$

We will proceed with the parameterization $r = a$:

$$\mathbf{p}^* = a\left[\cos(\theta(a))\hat{\mathbf{i}} + \sin(\theta(a))\hat{\mathbf{j}}\right] + \zeta(a, \theta(a))\,\hat{\mathbf{k}}. \tag{2.51}$$

Invoking definition 2.46 reveals $g'(a) = a$ whenever $\theta'(a)$ is well-behaved over the desired range of a. Under these circumstances, equation 2.48 collapses to 2.35, and we conclude that the flow *speed* $\bar{u}^*$ at any point in a constant cross-section rotating passage under isentropic

conditions is a function of the radial position only.

2.5 Work

One parameter of particular interest is the work derived from a radial turbine (or the work required to drive a radial compressor). In a straight duct, the work is most easily found by writing an energy balance over a control volume enveloping a section of the passage between two points:

$$\dot{W} - \dot{Q} = \dot{E}_{\text{st}} + \dot{m}_2 \left(h_2 + \frac{u_2^2}{2} \right) - \dot{m}_1 \left(h_1 + \frac{u_1^2}{2} \right). \tag{2.52}$$

Because the flow is adiabatic and steady we may neglect the heat transfer $\dot{Q}$ and transient energy storage $\dot{E}_{\text{st}}$ respectively. Furthermore we recognize that $\dot{m}_1 = \dot{m}_2 = \dot{m}$ and insert equation 2.6. With these simplifications, we have

$$\dot{W} = \dot{m} \left(c_p \left(T_2 - T_1 \right) + \frac{1}{2} \left(u_2^2 - u_1^2 \right) \right). \tag{2.53}$$

In a straight, radial duct such as the one shown in Fig. 2.1 or the duct shown in Fig. 2.3 we recognize that the velocity in the stationary frame is the vector sum of the in-frame velocity and the local tangential velocity of the duct $u(\hat{x}) = \sqrt{\hat{u}^2 + \omega^2 \hat{x}^2}$:

$$\begin{aligned}
\dot{W} &= \dot{m} \left(c_p T_2 + \frac{\left(\sqrt{\hat{u}_2^2 + \omega^2 \hat{x}_2^2} \right)^2}{2} - c_p T_1 - \frac{\left(\sqrt{\hat{u}_1^2 + \omega^2 \hat{x}_1^2} \right)^2}{2} \right) \\
&= \dot{m} \left(c_p \left(T_2 - T_1 \right) + \frac{\hat{u}_2^2 - \hat{u}_1^2}{2} + \frac{\omega^2 \left(\hat{x}_2^2 - \hat{x}_1^2 \right)}{2} \right) \\
&= \dot{m} \omega^2 \left(\hat{x}_2^2 - \hat{x}_1^2 \right) \qquad (2.54) \\
\dot{W}^* &= \frac{\left(\hat{x}_2^{*2} - \hat{x}_1^{*2} \right)}{Ro^2}. \qquad (2.55)
\end{aligned}$$

where $\dot{W}^* = \dot{W} / \dot{m} \hat{u}_c^2$ and equation 2.22 has been used. Equation 2.54 might be rewritten in terms of a duct tip speed $c = \omega \hat{x}_2$, so that where $\hat{x}_1 = 0$, the work transferred to/from the

passage is given by

$$\dot{W} = \dot{m}c^2. \tag{2.56}$$

Equation 2.56 is the rate form of the angular rocket propulsion equation developed by Polihronov and Straatman [2].

In a curved passage we must express the velocity in the stationary frame as $u(a) = \|\bar{u}\mathbf{t} + \boldsymbol{\Omega} \times \mathbf{p}\|$. Substituting this expression into equation 2.53 gives

$$\dot{W} = \dot{m}\left(c_p\left(T_2 - T_1\right) + \frac{1}{2}\left(\|\bar{u}_2\mathbf{t}_2 + \boldsymbol{\Omega} \times \mathbf{p}_2\|^2 - \|\bar{u}_1\mathbf{t}_1 + \boldsymbol{\Omega} \times \mathbf{p}_1\|^2\right)\right). \tag{2.57}$$

This equation cannot be reduced any further without knowing the form of $\mathbf{p}^*$.

2.6 Choked Flow Limitations

Several assumptions have been employed to arrive at the density, temperature, pressure, and velocity profiles of the above sections. These profiles are therefore only valid for particular combinations of Rossby and Mach numbers. While each of the assumptions listed at the beginning of section 2.3 merit their own discussion, in this work we will restrict our analysis to the sonic limit. If the flow transitions from subsonic to supersonic at any point in a rotating passage, there will inevitably be a shock at some point downstream as it again becomes subsonic. Shocks are highly irreversible and therefore undesirable in many applications, therefore it is of great interest to prevent the flow from transitioning in the first place. The next two subsections identify the conditions under which the flow transitions in rotating passages, and develop the appropriate constraints on the selection of *Ro* and *Ma*.

2.6.1 Sonic limitation in the shroud

Previously the adiabatic duct has been experimentally validated through injecting air tangentially into a circular passage surrounding a rotating disk and allowing the air to expand through

radial passages in the disk [20]. In this configuration the Mach number of the flow through the shroud, Ma_S, should be less than 1:

$$\begin{aligned} Ma_S &< 1 \\ \frac{u_2}{\sqrt{\gamma R_s T_2}} &< 1 \\ \frac{\omega^2 \hat{x}_2}{\sqrt{\gamma R_s T_2}} &< 1 \\ \frac{Ma^2}{Ro^2} &< 1 \\ Ma^2 &< Ro^2. \end{aligned} \tag{2.58}$$

2.6.2 Stagnation properties

In addition, we must ensure the flow does not transition within the passage itself, a state characterized by the presence of *choked flow* within the passage. To properly define this constraint we must first define several quantities before the topic can be addressed.

First, recall the *total enthalpy* in the stationary frame is defined as the total energy of a flowing stream per unit mass [21]:

$$h_0 = h + \frac{u^2}{2}. \tag{2.59}$$

If the fluid is assumed to be a perfect gas, the *total temperature* is found by invoking equation 2.6

$$\begin{aligned} T_0 &= T + \frac{u^2}{2c_p} \\ &= T + \frac{\hat{u}^2 + \omega^2 \hat{r}^2}{2c_p}. \end{aligned} \tag{2.60}$$

Equation 2.60 is similar to equation (17-4) in the thermodynamics text by Cengel and Boles [21], with the inclusion of the rotational energy per unit mass. This quantity is useful in sta-

tionary flows because it is constant over isentropic processes.

In contrast, the total temperature in the rotating frame may be defined as:

$$\hat{T}_0 = T + \frac{\hat{u}^2}{2c_p} \tag{2.61}$$

To see if either of these parameters are constant in the rotating duct problem we insert the temperature profile (Eq. 2.32) into the velocity profile (Eq. 2.48) and re-dimensionalize:

$$\frac{\hat{u}^2}{2c_p} + T - \frac{\omega^2\hat{r}^2}{2c_p} = \bar{T}_0.$$

Rearranging the above equation gives

$$\bar{T}_0 = T + \frac{\hat{u}^2 - \omega^2\hat{r}^2}{2c_p}. \tag{2.62}$$

We have called $\bar{T}_0$ the *stagnation temperature*, as this is the temperature which is attained if the fluid is brought to rest isentropically (while exchanging some energy with the walls of the passage). We have also replaced the parameter a with the co-ordinate $\hat{r}$, to emphasize that this quantity is the radial distance from the axis of rotation. Upon comparing equations 2.60 - 2.62 it's clear that neither the total temperature in the stationary frame nor the total temperature in the relative frame are constant along the passage, while the stagnation temperature, $\bar{T}_0$, is. Readers familiar with turbomachinery analysis will recognize the quantity $\bar{T}_0 c_p$ as the *rothalpy* [7]. Notice that the total temperature and stagnation temperature are not equal in general; i.e. $\hat{T}_0 \neq \bar{T}_0$.

The isentropic gas equations may be used to find relationships between stagnation and static pressure and density:

$$\frac{\bar{p}_0}{p} = \left(\frac{\bar{T}_0}{T}\right)^{\gamma/(\gamma-1)}, \tag{2.63}$$

$$\frac{\bar{\rho}_0}{\rho} = \left(\frac{\bar{T}_0}{T}\right)^{1/(\gamma-1)}. \tag{2.64}$$

Furthermore, we can use equation 2.62 to define the ratio of stagnation to static temperature in terms of dimensionless numbers:

$$\begin{aligned}\frac{\bar{T}_0}{T} &= 1 + \frac{\hat{u}^2 - \omega^2\hat{r}^2}{2c_pT},\\ \frac{\bar{T}_0}{T} &= \frac{1 + \frac{\gamma-1}{2}Ma_L^2}{1 + \frac{\gamma-1}{2}\left(\frac{\hat{r}}{\hat{r}_c}\right)^2 Ma_t^2},\end{aligned} \tag{2.65}$$

where Ma_L is a *local* Mach number and $Ma_t = \omega x_c / \sqrt{\gamma R_s \bar{T}_0}$ is the tip Mach number. Equation 2.65 reduces to its stationary counterpart (equation 17-18 in Ref. [21]) when $\omega = 0$.

In addition, we evaluate equation 2.48 at the location $\hat{r}^* = 1$ to devise two useful relationships between Ma, Ro, γ, and Ma_t:

$$\frac{1}{2} + \frac{1}{(\gamma-1)\,Ma^2} - \frac{1}{2Ro^2} = \frac{1}{(\gamma-1)\,Ma_t^2 Ro^2}, \tag{2.66}$$

$$\frac{Ma^2}{Ro^2 Ma_t^2} = \frac{\bar{T}_0}{T_c} = \frac{1 + \frac{\gamma-1}{2}Ma^2}{1 + \frac{\gamma-1}{2}Ma_t^2}. \tag{2.67}$$

2.6.3 Choked flow

Using the above definitions, the choked flow condition may be identified. The mass flow rate at any location in a radial passage is given by

$$\dot{m} = \rho A\hat{u} = pA\sqrt{\frac{\gamma}{RT}}Ma_L. \tag{2.68}$$

Using property ratios 2.65 and 2.63 and simplifying yields

$$\dot{m} = \bar{p}_0 A\sqrt{\frac{\gamma}{R\bar{T}_0}}Ma_L\left[\frac{1 + \frac{\gamma-1}{2}\left(\frac{\hat{r}}{\hat{r}_c}\right)^2 Ma_t^2}{1 + \frac{\gamma-1}{2}Ma_L^2}\right]^{(\gamma+1)/\left[2(\gamma-1)\right]}. \tag{2.69}$$

We can also define the maximum possible mass flow rate for any given duct, by differentiating equation 2.69 with respect to Ma_L and setting the result equal to 0, which yields $Ma_L = 1$. Inserting this restriction into equation 2.69 yields the critical, or choked mass flow:

$$\dot{m}_{\text{Ch}} = \bar{p}_0 A \sqrt{\frac{\gamma}{R\bar{T}_0}} \left[\frac{2}{\gamma+1} \left(1 + \frac{\gamma-1}{2} \left(\frac{\hat{r}}{\hat{r}_c} \right)^2 Ma_t^2 \right) \right]^{(\gamma+1)/\left[2(\gamma-1)\right]} . \tag{2.70}$$

We can nondimensionalize with $\dot{m}_{\text{Ch}} = \dot{m}^*_{\text{Ch}} \rho_c A_c \hat{u}_c$:

$$\dot{m}^*_{\text{Ch}} = \frac{\bar{\rho}_0}{\rho_c} \sqrt{\frac{\bar{T}_0}{T_c}} \frac{A^*}{Ma} \left[\frac{2}{\gamma+1} \left(1 + \frac{\gamma-1}{2} \hat{r}^{*2} Ma_t^2 \right) \right]^{(\gamma+1)/\left[2(\gamma-1)\right]} . \tag{2.71}$$

Using equations 2.64 and 2.65, the property ratios in the above equation may be cast in terms of the global Mach number and tip Mach number:

$$\dot{m}^*_{\text{Ch}} = \frac{A^*}{Ma} \left[\frac{2}{\gamma+1} \frac{1 + \frac{\gamma-1}{2} Ma^2}{1 + \frac{\gamma-1}{2} Ma_t^2} \left(1 + \frac{\gamma-1}{2} \hat{r}^{*2} Ma_t^2 \right) \right]^{(\gamma+1)/\left[2(\gamma-1)\right]} . \tag{2.72}$$

Equation 2.72 represents the maximum possible mass flow rate at any radial location. Notice $\dot{m}^*_{\text{Ch}}$ varies with the radial co-ordinate $\hat{r}^*$. If, at any location, $\dot{m}^*_{\text{Ch}} > 1$, the flow will be choked in the passage.

While expression 2.72 is useful, we desire a simpler test to determine whether the flow is choked. Regardless of the area profile the critical mass flow rate in the passage is dictated by the location of minimum choked flow, that is, where equation 2.72 is minimized. We begin by differentiating with respect to $\hat{r}^*$:

$$\begin{aligned} \frac{\mathrm{d}\dot{m}^*_{\text{Ch}}}{\mathrm{d}\hat{r}^*} = A^* B \frac{\gamma+1}{2} \left[1 + \frac{\gamma-1}{2} \hat{r}^{*2} Ma_t^2 \right]^{(\gamma+1)/\left[2(\gamma-1)\right]-1} \hat{r}^* Ma_t^2 + \\ + \frac{\mathrm{d}A^*}{\mathrm{d}\hat{r}^*} B \left[1 + \frac{\gamma-1}{2} \hat{r}^{*2} Ma_t^2 \right]^{(\gamma+1)/\left[2(\gamma-1)\right]} . \end{aligned} \tag{2.73}$$

Where we have defined the parameter B for compactness:

$$B = \frac{1}{Ma} \left[\frac{2}{\gamma+1} \frac{1 + \frac{\gamma-1}{2} Ma^2}{1 + \frac{\gamma-1}{2} Ma_t^2} \right]^{(\gamma+1)/\left[2(\gamma-1)\right]} .$$

Setting equation 2.73 equal to 0 yields

$$\frac{1}{A^*} \frac{\mathrm{d}A^*}{\mathrm{d}\hat{r}^*} = -\frac{\gamma+1}{2} \frac{\hat{r}^* Ma_t^2}{1 + \frac{\gamma-1}{2} \hat{r}^{*2} Ma_t^2} . \tag{2.74}$$

Constant cross-section duct

For the case when $A^* = 1$, the above equation suggests the only extrema is at $\hat{r}^* = 0$. By differentiating 2.73 again and inserting $\hat{r} = 0$ gives

$$\frac{\mathrm{d}^2 \dot{m}^*_{\mathrm{Ch}}}{\mathrm{d}\hat{r}^{*2}} = A^* B \frac{\gamma + 1}{2} Ma_t^2.$$

Since each of the terms in the above equation are positive, the concavity of 2.72 is positive at $\hat{r}^* = 0$, confirming that $\hat{r}^* = 0$ is a minima. Since it is the only extrema, it must be the global minimum, and therefore the location which determines the minimum choked mass flow rate for the duct of constant cross-section. Inserting $\hat{r}^* = 0$ into equation 2.72 yields

$$\dot{m}^*_{\mathrm{Ch,\,min}} = \frac{1}{Ma}\left[\frac{2}{\gamma+1}\frac{1+\frac{\gamma-1}{2}Ma^2}{1+\frac{\gamma-1}{2}Ma_t^2}\right]^{(\gamma+1)/[2(\gamma-1)]}. \tag{2.75}$$

Therefore, in order to ensure the flow is not choked, we require

$$\begin{aligned}
\dot{m}^* &< \dot{m}^*_{\mathrm{Ch,\,min}}, \\
1 &< \frac{1}{Ma}\left[\frac{2}{\gamma+1}\frac{1+\frac{\gamma-1}{2}Ma^2}{1+\frac{\gamma-1}{2}Ma_t^2}\right]^{(\gamma+1)/[2(\gamma-1)]}, \\
1 &< \frac{1}{Ma}\left[\frac{2}{\gamma+1}\frac{Ma^2}{Ro^2 Ma_t^2}\right]^{(\gamma+1)/[2(\gamma-1)]}, \\
\frac{2}{\gamma+1}Ma^{4/(\gamma+1)} &> Ro^2 Ma_t^2.
\end{aligned} \tag{2.76}$$

Combining equations 2.76 and 2.66 and re-arranging results in a cumbersome inequality in terms of Ma and Ro, which has been plotted in Fig. 2.6.

Rotating slice

If the duct area varies with the equation $A^* = \hat{r}^*$, $\hat{r}^* > 0$ (a rotating slice), equation 2.74 reduces to $\hat{r}^* = i/\gamma Ma_t$. Since there are no real solutions, there are no extrema on equation 2.72, and the critical section for choked flow may be determined by comparing the choked mass flow rates at the inner and outer radii: $\hat{r}^* = \hat{r}^*_1, \hat{r}^*_2$ where $\hat{r}^*_1 < \hat{r}^*_2$. Clearly, $\dot{m}^*_{\mathrm{Ch}}(\hat{r}^*_1) < \dot{m}^*_{\mathrm{Ch}}(\hat{r}^*_2)$, and the maximum mass flow rate is

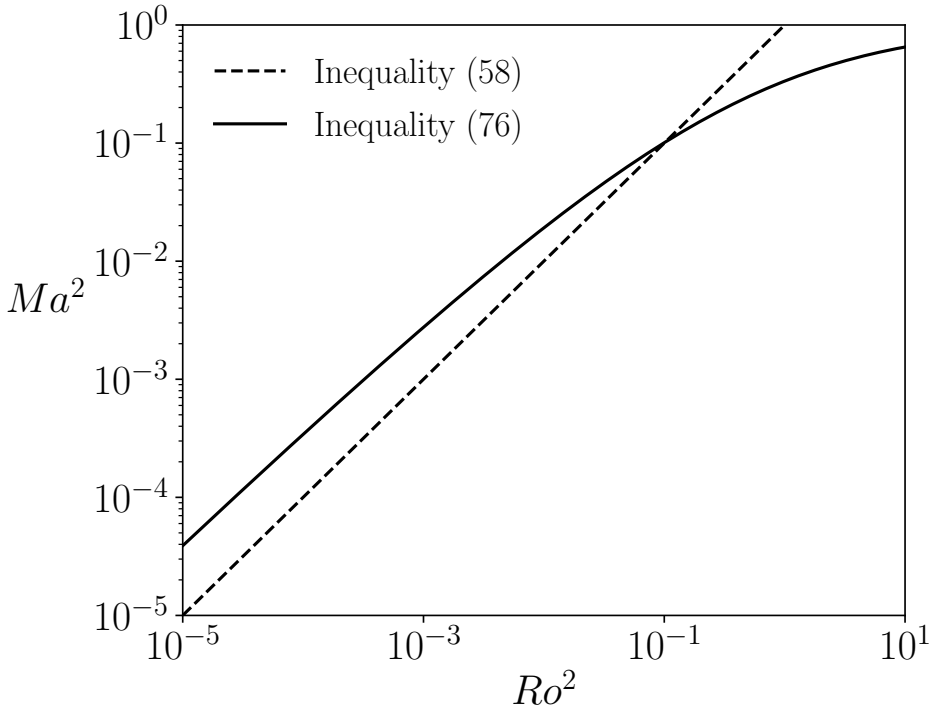

Figure 2.6: Restrictions on Rossby and Mach numbers dictated by the choked flow constraint for a straight, constant cross-section duct which crosses (or terminates at) the axis of rotation. All equations were evaluated with $\gamma = 1.4$.

$$\dot{m}^*_{\text{Ch, min}} = \frac{\hat{r}^*_1}{Ma}\left[\frac{2}{\gamma+1}\frac{1+\frac{\gamma-1}{2}Ma^2}{1+\frac{\gamma-1}{2}Ma_t^2}\left(1+\frac{\gamma-1}{2}\hat{r}^{*2}_1 Ma_t^2\right)\right]^{(\gamma+1)/[2(\gamma-1)]}. \tag{2.77}$$

Critical duct

If equation 2.72 is evaluated such that the flow is choked everywhere ($\dot{m}^*_{\text{Ch}} = 1$), we can formulate the critical cross-sectional area profile:

$$\begin{aligned} A^*_{\text{Ch}} &= Ma\left[\frac{\gamma+1}{2}\frac{1}{1+\frac{\gamma-1}{2}Ma^2}\frac{1+\frac{\gamma-1}{2}Ma_t^2}{1+\frac{\gamma-1}{2}\hat{r}^{*2}Ma_t^2}\right]^{(\gamma+1)/[2(\gamma-1)]}, \\ &= \frac{Ma^*_t(Ma_t,\hat{r}^*,\gamma)}{A^*_t(Ma,\gamma)}. \end{aligned} \tag{2.78}$$

Where we have recognized the appearance of the area ratio A/A_t, which has been defined for stationary ducts:

$$A_t^* = \frac{A}{A_t} = \frac{1}{Ma}\left[\frac{2}{\gamma+1}\left(1+\frac{\gamma-1}{2}Ma^2\right)\right]^{(\gamma+1)/[2(\gamma-1)]}. \tag{2.79}$$

We have also introduced a modified tip Mach number,

$$Ma_t^* = \left[\frac{1+\frac{\gamma-1}{2}Ma_t^2}{1+\frac{\gamma-1}{2}\hat{r}^{*2}Ma_t^2}\right]^{(\gamma+1)/[2(\gamma-1)]}. \tag{2.80}$$

Equation 2.79 has been tabulated for many values of Ma and γ in many engineering texts such as Ref. [21]. The scale of the profile is determined by A_t^*, while the profile shape is determined by Ma_t^*, which has been plotted in Fig. 2.7. When $Ma = 1$, $A_{\text{Ch}}^* = Ma_t^*$ and the curves represent the minimum area required to avoid the choked flow condition. When $Ma < 1$, these curves are scaled by $1/A_t^*$. Notice the required area decreases with increasing $\hat{r}^*$. We now propose an alternative method to determine whether the flow is choked in a known duct: plot the profiles $A^*(\hat{r}^*)$ and $A_{\text{Ch}}^*(\hat{r}^*)$ on the same axes. If $A^* < A_{\text{Ch}}^*$ at any point, the flow will be choked.

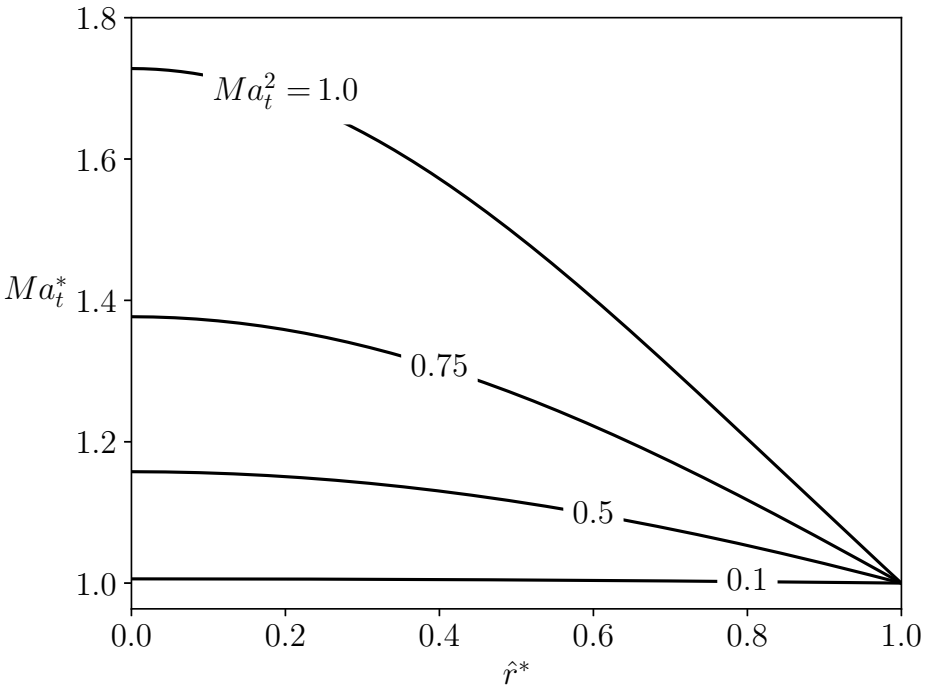

Figure 2.7: Plots of equation 2.80 for a range of Ma_t^* (tip Mach numbers) with $\gamma = 1.4$.

2.7 Conclusion

In this work we have developed expressions for density, temperature, pressure, and velocity profiles within arbitrarily curved ducts with arbitrarily varying cross-sectional area profiles under isentropic, compressible flow conditions where the fluid may be considered a perfect gas. These profiles are given by equations 2.31, 2.32, 2.33, and 2.35 respectively. We have verified our results through comparison with equivalent CFD simulations. These derivations verify the assumption that is frequently made in turbomachinery texts: rothalpy is conserved along curved passages when the five requirements indictated by Lyman et al. [14] are met. In addition, we have characterized the choked flow condition for compressible flow within straight ducts, clearly indicating the constraints on the choice of dimensionless groups Ma, Ro, Ma_t, and γ required to avoid the choked flow condition. We have characterized the variation in the critical cross-sectional area and shown how it can be used to quickly evaluate whether or not flow will choke in a rotating duct of known geometry. During this process we have identified the importance of the stagnation temperature, which may be much more pertinent than the often-used total temperature for studies involving rotating compressible flows.

Bibliography

[1] J. G. Polihronov and A. G. Straatman, "Thermodynamics of Angular Propulsion in Fluids," *Physical Review Letters*, vol. 109, p. 54504, 8 2012.

[2] J. G. Polihronov and A. G. Straatman, "Angular propulsion – the rotational analog of rocket motion," *Canadian Journal of Physics*, vol. 92, no. August 2014, pp. 89–92, 2015.

[3] G. J. Ranque, "Experiments on expansion in a vortex with simultaneous exhaust of hot air and cold air," *J. Phys. Radium*, vol. 4, no. 7, pp. 112–114, 1933.

[4] H. R. Thakare, A. Monde, and A. D. Parekh, "Experimental, computational and optimization studies of temperature separation and flow physics of vortex tube: A review," *Renewable and Sustainable Energy Reviews*, vol. 52, pp. 1043–1071, 2015.

[5] H. P. Greenspan, *The theory of rotating fluids*. New York, NY, USA: CUP Archive, 1 ed., 1968.

[6] J. P. Vanyo, *Rotating fluids in engineering and science*. Mineola, NY, USA: Elsevier, 1 ed., 2015.

[7] S. L. Dixon and C. Hall, *Fluid mechanics and thermodynamics of turbomachinery*. Butterworth-Heinemann, 7th ed., 2013.

[8] E. M. Greitzer, C. S. Tan, and M. B. Graf, *Internal flow: concepts and applications*, vol. 3. Cambridge University Press, 2007.

[9] P. R. Tatro and E. L. Mollo-Christensen, "Experiments on Ekman layer instability," *Journal of Fluid Mechanics*, vol. 28, no. 3, pp. 531–543, 1967.

[10] R. Kristoffersen and H. I. Andersson, "Direct simulations of low-Reynolds-number turbulent flow in a rotating channel," *Journal of Fluid Mechanics*, vol. 256, p. 163, 11 1993.

[11] H. S. Kheshgi and L. E. Scriven, "Viscous Flow Through a Rotating Square Channel," *Physics of Fluids*, vol. 28, no. 10, pp. 2968–2979, 1985.

[12] S. Lieblein, "Theoretical and experimental analysis of one-dimensional compressible flow in a rotating radial-inlet impeller channel," Tech. Rep. October, 1952.

[13] N. A. Cumpsty, *Compressor aerodynamics*. Longman Scientific & Technical, 1989.

[14] F. Lyman, "On the conservation of rothalpy in turbomachines," *Journal of Turbomachinery*, vol. 115, no. 3, 1993.

[15] C. Bosman and O. C. Jadayel, "A quantified study of rothalpy conservation in turbomachines," *International Journal of Heat and Fluid Flow*, vol. 17, no. 4, pp. 410–417, 1996.

[16] M. L. Combrinck and L. N. Dala, "Eulerian Derivations of Non-Inertial Navier-Stokes Equations," in *11th International Conference on Heat Transfer, Fluid Mechanics and Thermodynamics*, (Kruger National Park), pp. 1–20, 2014.

[17] A. Kageyama and M. Hyodo, "Eulerian derivation of the Coriolis force," *Geochemistry, Geophysics, Geosystems*, vol. 7, no. 2, pp. 1–5, 2006.

[18] K. Masatsuka, *I do like CFD*, vol. 1. Cradle, 2 ed., 2013.

[19] ANSYS Inc., "ANSYS CFX-Pre User's Guide," 2011.

[20] J. Polihronov and A. G. Straatman, "Mechanism for enhanced energy extraction and cooling pressurized gas," 2013.

[21] Y. A. Cengel and M. A. Boles, *Thermodynamics: an engineering approach*. McGraw-Hill Higher Education, 8th ed., 2006.

Chapter 3

Exact Solutions to the Three-Dimensional Navier–Stokes Equations Using the Extended Beltrami Method

3.1 Introduction

The Navier-Stokes equations describe mathematically the motions of a fluid where pressure forces and viscous forces are significant. When the flow may be considered incompressible and isothermal, the governing equations may be written in dimensionless form:

$$\boldsymbol{\nabla} \cdot \mathbf{u} = 0, \tag{3.1}$$

$$\frac{\partial \mathbf{u}}{\partial t} + (\mathbf{u} \cdot \boldsymbol{\nabla})\,\mathbf{u} = -\boldsymbol{\nabla} p + \frac{1}{Re}\nabla^2 \mathbf{u}, \tag{3.2}$$

where $\mathbf{u}$ is the velocity, t is time, $\boldsymbol{\nabla}$ is the gradient operator, p is the thermodynamic pressure, and the Reynolds number is defined as $Re = u_c x_c / \nu$. The parameters u_c and x_c are characteristic velocity and length scales, respectively, and ν is the kinematic viscosity. Equation 3.2 introduces significant complexity in solving fluid flow problems, as the second term (known as the advection term) renders the equation non-linear, while the fourth term, (representing the contribution of viscous forces) contains derivatives of the second order. No general solution to the system 3.1-3.2 has been found, nor is there a single solution technique which can be used

to obtain all the solutions found in the literature. Many fluid flow problems encountered in engineering contain complicated geometries and boundary conditions, which can be intractable without the aid of numerical methods. Nevertheless, exact solutions, wherever they can be obtained, can give important insights into the relationships between solution parameters, provide closed-form expressions of base flows as starting points for linear and non-linear stability analyses, and serve as benchmark solutions for testing computer codes. Fluid dynamics textbooks such as Ref. [1] contain many elementary solutions to the Navier-Stokes equations, but are not exhaustive. Readers are directed to the reviews of Wang [2, 3] and the book by Drazin and Riley [4] for a comprehensive summary of the exact solutions found in the literature.

An *exact solution* to the Navier-Stokes equations is a solution

Exact solutions are most commonly obtained by one of three general approaches: analysis of unidirectional or essentially unidirectional flows, similarity solutions, and Beltrami and Beltrami-related flows. Since the approach described in the present work extends a Beltrami-related solution technique, only similar solution techniques will be reviewed here.

Taking the curl of the vector equation 3.2 gives the vorticity equation

$$\frac{\partial \omega}{\partial t} + \boldsymbol{\nabla} \times (\omega \times \mathbf{u}) = \frac{1}{Re} \nabla^2 \omega \tag{3.3}$$

where $\omega = \boldsymbol{\nabla} \times \mathbf{u}$ is the vorticity. Flows in which the vorticity is 0 everywhere are called irrotational [1]. If the flow is assumed to be planar, and cross-flow is absent, two of the vorticity components are zero, and only one equation survives. Several researchers have addressed this general case, by guessing various functional forms of the streamfunction, and solving the vorticity equation, including Polyanin and Aristov [5], Polyanin and Zhurov [6], and Kumar and Kumar [7]. These solutions often include complicated unsteady terms, which are difficult to visualize.

3.1.1 Beltrami Flows

In a Beltrami flow, the vorticity is parallel to the streamlines everywhere and the cross product $\omega \times \mathbf{u}$ vanishes. This condition is primarily useful for solving flow problems with negligible

viscous forces (i.e. $\nu \to 0$), where the flow is still rotational. In this case it can be shown (see section 3.6 of Ref. [1]) that the Bernoulli function remains constant throughout the flow domain.

3.1.2 Generalized Beltrami Flows

When the alternative condition $\nabla \times (\omega \times \mathbf{u}) = \mathbf{0}$ holds, the flow is called a *generalized* Beltrami flow. Most often, this approach has been adopted to study 2D planar and 2D axissymetric flows without cross-flow or swirl, respectively. In these cases, two of the vorticity components vanish, and the solution is constrained by the definition of the third component of vorticity, the generalized Beltrami flow condition, and the remaining terms in equation 3.3. For the special case when the vorticity is constant, the three equations reduce to a single Poisson type equation in terms of the streamfunction. Working in Cartesian co-ordinates, Tsien [8] developed two solutions describing the influence of a line source and a line vortex on a shear flow, respectively. Wang [9] presented a solution representing "shear flow over convection cells", and another solution [3] describing the oblique impingement of two jets. In cylindrical co-ordinates a similar simplification yields a Poisson-like partial differential equation in terms of the streamfunction. Specific solutions include Hill's spherical vortex [10] and augmentations thereof: O'Brien's ellipsoidal vortex [11], Wang's toroidal vortex [9], and the solutions given by Fujimoto et al.[12]. Recently, Joseph [13] has shown that there is a general family of solutions in terms of generalized hypergeometric series which contain, in addition to Hill's, Wang's and Fujimoto et al.'s solutions as special cases, 'figure 8' and butterfly vortices, for different choices of the coefficients. Berker [14] gives a homogeneous solution in terms of Bessel functions and exponential functions. Terrill [15], apparently independantly, developed a solution describing the axissymmetric motion of fluid in a porous pipe which is an expression of Berker's solution.

Saccomandi studied steady and unsteady *pseudo-plane* flows wherein only the third component of the advection term is required to vanish [16, 17] in a Cartesian co-ordinate system (i.e. $\nabla \times (\omega \times \mathbf{u}) \cdot \hat{\mathbf{k}} = 0$, where $\hat{\mathbf{k}}$ is the unit vector pointing in the z-direction). In these works pseudo-plane flows are those in which the motion is restricted to the x-y plane, but the streamfunction retains dependence on the z co-ordinate.

Weinbaum and O'Brien [18] have collected and expanded the set of known solutions to the Navier-Stokes equations under the generalized Beltrami condition where out-of-plane velocity components (called cross-flow for Cartesian systems, and swirl in axisymmetric cylindrical co-ordinate systems) are significant, with the stipulation that the streamfunction and out-of-plane velocity components vary only with in-plane co-ordinates, and time.

3.1.3 Extended Beltrami Flows

Wang [19] presented another solution technique, wherein the third component of vorticity is expressed as a function of the streamfunction plus an auxiliary function of assumed form. The rationale for this choice as well as existing solutions obtainable using this method will be discussed in section 3.3.

Our initial motivation for undertaking the present work was to develop an exact solution that resembles Ranque-Hilsch flow, however we quickly realized that our derivation (described in section 3.6.2) was based on a more general extension of the extended Beltrami method, which has not yet been detailed in the literature. In the present work we aim to systematically reduce the governing equations according to the assumptions of the extended Beltrami method, while keeping the formulation co-ordinate system independent.

In section 3.2, we develop the streamfunction-vorticity equation set in general orthogonal curvilinear co-ordinates, laying the groundwork for section 3.3 where the extended Beltrami method surmised by Wang is extended to three dimensional flows. In section 3.4 we show our formulation reduces to that of Wang for 2D planar flows, and revisit some familiar solutions. In section 3.5 we briefly demonstrate that all planar solutions of section 3.4 support a non-uniform out-of-plane velocity distribution, which is easily obtainable from the planar solution. In section 3.6 we study axisymmetric flows with swirl; we revisit Burgers vortex and related flows, and develop a new solution, which can be considered the angular analogue of Kovasznay flow. We summarize our contributions in section 3.7.

3.2 Governing Equations

In the present section the governing equations 3.2 and 3.3 will be further developed in preparation for deriving the working equations in section 3.3. We first write the continuity equation 3.1 in terms of a general orthogonal curvilinear co-ordinate system (x_1, x_2, x_3), wherein velocity and pressure are independent of the the third co-ordinate, x_3:

$$\frac{\partial}{\partial x_1}(h_2 h_3 u_1) + \frac{\partial}{\partial x_2}(h_3 h_1 u_2) = 0 \tag{3.4}$$

Furthermore, the velocity can be represented in terms of a pair of streamfunctions, ψ and γ [1]:

$$\mathbf{u} = \boldsymbol{\nabla} \times (\psi \boldsymbol{\nabla} \gamma) + u_3 \hat{\mathbf{e}}_3 \tag{3.5}$$

where the first term on the right hand side of equation 3.5 is a vector lying in the x_1-x_2 surface and the final term is a vector pointing in the x_3 direction. Inserting equation 3.5 into equation 3.4, we find $\gamma = x_3$, and the velocity may be expressed as

$$\mathbf{u} = \frac{1}{h_3}(\boldsymbol{\nabla}\psi) \times \hat{\mathbf{e}}_3 + u_3 \hat{\mathbf{e}}_3 = \frac{1}{h_2 h_3}\frac{\partial \psi}{\partial x_2}\hat{\mathbf{e}}_1 - \frac{1}{h_1 h_3}\frac{\partial \psi}{\partial x_1}\hat{\mathbf{e}}_2 + u_3 \hat{\mathbf{e}}_3 \tag{3.6}$$

where $h_i = h_i(x_1, x_2), \mathbf{e}_i, i \in \{1, 2, 3\}$ are the corresponding scale factors and unit vectors, respectively. Note the present analysis excludes co-ordinate systems in which any of the scale factors vary with the third co-ordinate, x_3, such as conical, confocal ellipsoidal, and confocal paraboloidal co-ordinate systems. The vorticity may also be expressed in terms of the streamfunction:

$$\omega = \boldsymbol{\nabla} \times \mathbf{u} = \frac{1}{h_2 h_3}\frac{\partial (h_3 u_3)}{\partial x_2}\hat{\mathbf{e}}_1 - \frac{1}{h_1 h_3}\frac{\partial (h_3 u_3)}{\partial x_1}\hat{\mathbf{e}}_2 - \frac{1}{h_1 h_2}\left[\frac{\partial}{\partial x_1}\left(\frac{h_2}{h_1 h_3}\frac{\partial \psi}{\partial x_1}\right) + \frac{\partial}{\partial x_2}\left(\frac{h_1}{h_2 h_3}\frac{\partial \psi}{\partial x_2}\right)\right]\hat{\mathbf{e}}_3 \tag{3.7}$$

As it will be seen later, it is useful to define the pseudo-vorticity; a modified definition of the third component of the vorticity vector [19]:

$$\xi = \frac{\omega_3}{h_3} = \frac{-1}{h_1 h_2 h_3}\left[\frac{\partial}{\partial x_1}\left(\frac{h_2}{h_1 h_3}\frac{\partial \psi}{\partial x_1}\right) + \frac{\partial}{\partial x_2}\left(\frac{h_1}{h_2 h_3}\frac{\partial \psi}{\partial x_2}\right)\right] = -\frac{D^2(\psi)}{V} \tag{3.8}$$

where $V = h_1 h_2 h_3$. The cross-flow velocity may be written as $\sigma = h_3 u_3$. Using these definitions, the u_3-momentum and ω_3-vorticity equations may be expressed as:

$$V\frac{\partial \sigma}{\partial t} + K(\sigma, \psi) = \frac{h_3^2 D^2(\sigma)}{Re} \tag{3.9}$$

$$V\frac{\partial \xi}{\partial t} + K(\xi, \psi) - K\left(\frac{\sigma}{h_3^2}, \sigma\right) = \frac{D^2\left(h_3^2 \xi\right)}{Re} \tag{3.10}$$

where $K(a, b) = \frac{\partial a}{\partial x_1}\frac{\partial b}{\partial x_2} - \frac{\partial b}{\partial x_1}\frac{\partial a}{\partial x_2}$ is the Jacobian. Equations 3.9 and 3.10 have been derived in the Appendix. While the pressure p may be determined through the first two components of equation 3.2, the first two equations in 3.3 are superfluous in the present formulation [20]. Thus, solutions to the system of equations 3.8-3.10 are also solutions to the Navier-Stokes equations. These equations are the point of departure for Polyanin [21] and Polyanin and Zhurov [6], who have assumed various forms of the streamfunction ψ in the absence of cross-flow ($\sigma = 0$), and arrived at a variety of solutions for 2D planar flows. Lewellen [22] has developed the same equations for the case of axisymmetric cylindrical co-ordinates, and derived an asymptotic series solution to describe vortex motion wherein a specific dimensionless parameter is considered small. Granger [23] has adopted Lewellen's formulation, and derived approximate solutions using a power series formulation.

3.3 Wang's Approach

Wang [19, 2] surmised the solution techniques of earlier researchers including Kovasznay [24], Taylor [25], Kelvin, and others, suggesting that, in the absence of flow normal to the ψ-plane, the pseudo-vorticity of any axisymmetric or 2D flow could be represented as:

$$\xi = g(\psi) + \chi(x_1, x_2, t) = -\frac{D^2(\psi)}{V} \tag{3.11}$$

where $g(\psi)$ and $\chi(x_1, x_2)$ are known functions. Wang rationalizes this choice by observing that when equation 3.11 is inserted into equation 3.10 (with $\sigma = 0$) the advection terms involving g are self-cancelling. Furthermore, under this formulation the viscous term in equation 3.10 contains $D^2\left(h_3^2 \xi\right)$, which in turn may be replaced using equation 3.11 twice. When

$g(\psi) \propto \psi$ equation 3.10 reduces to a first order quasi-linear partial differential equation, which is readily solvable for many choices of χ. The aim of the present work is to develop similar relations to yield solutions for cases where the cross-flow σ may vary with x_1, x_2. While Wang's original work developed equation 3.10, including the out-of-plane velocity component, the Navier-Stokes equations were not explicitly considered and only solutions to 2D planar flows were derived. To the best of our knowledge, no exact solutions extending Wang's approach to three dimensions exist in the open literature.

To begin, ξ *and* σ are first expressed in terms of ψ and t such that the advection terms are reduced to 0. Beginning with the advection terms of equations 3.9 and 3.10, the reasoning of Leprovost et al. [26] has been followed, while generalizing the derivation for unsteady flows in an arbitrariry orthogonal curvilinear co-ordinate system:

$$K(\sigma, \psi) = 0 \tag{3.12}$$

$$K(\xi, \psi) - K\left(\frac{\sigma}{h_3^2}, \sigma\right) = 0 \tag{3.13}$$

Equation 3.12 is satisfied when $\sigma = F(\psi, t)$. Then, using the identity

$$K\left(\frac{\sigma}{h_3^2}, F\right) = K\left(\frac{\sigma}{h_3^2}\frac{\partial F}{\partial \psi}, \psi\right) \tag{3.14}$$

equation 3.13 may be rewritten:

$$K\left(\xi - \frac{F}{h_3^2}\frac{\partial F}{\partial \psi}, \psi\right) = 0 \tag{3.15}$$

which suggests $\xi - (F/h_3^2)\,\partial F/\partial\psi = G(\psi, t)$. The desired forms of the cross-flow velocity and pseudo-vorticity are

$$\sigma = F(\psi, t) \tag{3.16}$$

$$\xi = \frac{F}{h_3^2}\frac{\partial F}{\partial \psi} + G(\psi, t) \tag{3.17}$$

Together with equation 3.8, these are the Bragg-Hawethorne or Squire-Long equations presented for a general curvilinear orthogonal co-ordinate system [27, 28]. In their present state,

application of equations 3.16 and 3.17 to the system 3.9 and 3.10 would leave only the unsteady and viscous terms, and generalized Beltrami flows can be obtained by solving the reduced equation set. Instead we follow Wang's approach [19], and add auxiliary functions to σ and ξ:

$$\sigma = F(\psi, t) + \Phi(x_1, x_2, t) \tag{3.18}$$

$$\xi = \frac{F}{h_3^2}\frac{\partial F}{\partial \psi} + G(\psi, t) + X(x_1, x_2, t) = -\frac{D^2(\psi)}{V} \tag{3.19}$$

Substituting the above forms into equations 3.9 and 3.10 and simplifying yields

$$V\frac{\partial F}{\partial t} + V\frac{\partial \Phi}{\partial t} + K(\Phi, \psi) = \frac{h_3^2}{Re}\left\{\frac{\partial F}{\partial \psi}D^2(\psi) + \frac{\partial^2 F}{\partial \psi^2}\bar{\psi}^2 + D^2(\Phi)\right\} \tag{3.20}$$

$$\begin{aligned}\frac{V}{h_3^2}\left(\frac{\partial F}{\partial t}\frac{\partial F}{\partial \psi} + F\frac{\partial^2 F}{\partial \psi \partial t}\right) + V\frac{\partial G}{\partial t} + V\frac{\partial X}{\partial t} + K(X, \psi) + \frac{2}{h_3^3}\left[(F + \Phi)\, K\left(h_3, \Phi\right) + \Phi\frac{\partial F}{\partial \psi}K\left(h_3, \psi\right)\right] = \\ = \frac{1}{Re}\left\{\left[\left(\frac{\partial F}{\partial \psi}\right)^2 + F\frac{\partial^2 F}{\partial \psi^2} + h_3^2\frac{\partial G}{\partial \psi}\right]D^2(\psi) + \frac{\partial}{\partial \psi}\left[\left(\frac{\partial F}{\partial \psi}\right)^2 + F\frac{\partial^2 F}{\partial \psi^2} + h_3^2\frac{\partial G}{\partial \psi}\right]\bar{\psi}^2\right\} + \\ + \frac{1}{Re}\left\{D^2\left(h_3^2\right)G + D^2\left(h_3^2 X\right) + 4\frac{\partial G}{\partial \psi}\left[\frac{h_2}{h_1}\frac{\partial h_3}{\partial x_1}\frac{\partial \psi}{\partial x_1} + \frac{h_1}{h_2}\frac{\partial h_3}{\partial x_2}\frac{\partial \psi}{\partial x_2}\right]\right\}\end{aligned} \tag{3.21}$$

where

$$\bar{\psi}^2 = \frac{h_2}{h_1 h_3}\left(\frac{\partial \psi}{\partial x_1}\right)^2 + \frac{h_1}{h_2 h_3}\left(\frac{\partial \psi}{\partial x_2}\right)^2 \tag{3.22}$$

Equations 3.20 and 3.21 are cumbersome and unlikely to yield solutions while the nonlinear $\bar{\psi}^2$ terms are present. To eliminate these terms we set $F, G \propto \psi$. Additionally, from hereon-in we narrow our focus to steady solutions, dropping the dependence on t, so equations 3.18 and 3.19 are reduced to

$$F(\psi) = d_F \psi \tag{3.23}$$

$$G(\psi) = d_G \psi \tag{3.24}$$

and the auxiliary functions are relabeled: $\Phi(x_1, x_2) = \phi(x_1, x_2)$ and $X(x_1, x_2) = \chi(x_1, x_2)$. With these simplifications, the pseudo-vorticity reduces to:

$$\xi = \frac{d_F^2}{h_3^2}\psi + d_G\psi + \chi = -\frac{D^2(\psi)}{V} \tag{3.25}$$

and equations 3.20 and 3.21 become:

$$K(\phi, \psi) = \frac{1}{Re}\left\{h_3^2 D^2(\phi) - V d_F\left(d_F^2\psi + d_G h_3^2\psi + h_3^2\chi\right)\right\} \tag{3.26}$$

$$K(\chi, \psi) + \frac{2}{h_3^3}\left[\left(d_F\psi + \phi\right)K\left(h_3, \phi\right) + \phi d_F K\left(h_3, \psi\right)\right] =$$

$$= \frac{1}{Re}\left\{-V\left(d_F^2 + d_G h_3^2\right)\left(\frac{d_F^2}{h_3^2}\psi + d_G\psi + \chi\right) + d_G D^2\left(h_3^2\right)\psi + D^2\left(h_3^2\chi\right) + 4d_G\left[\frac{h_2}{h_1}\frac{\partial h_3}{\partial x_1}\frac{\partial\psi}{\partial x_1} + \frac{h_1}{h_2}\frac{\partial h_3}{\partial x_2}\frac{\partial\psi}{\partial x_2}\right]\right\} \tag{3.27}$$

In principle, equations 3.25-3.27 may be used to find almost any 3D flow in an orthogonal co-ordinate system, provided the flow is independent of one of the co-ordinates and the scale factors of the chosen co-ordinate system are independent of the same co-ordinate. In practice, the value of the present formulation is limited by the number of auxiliary functions which are 'simple enough' to generate exact solutions. In the following subsections both existing and new solutions will be found, using linear and quadratic auxiliary functions. Further assumptions are required to reach general solutions, and these will be explored in the following sections.

3.4 2D planar flows

In the absence of an out-of-plane velocity component (i.e. $\sigma = d_F = \phi = 0$), equation 3.26 is automatically satisfied. In planar co-ordinate systems $h_3 = 1$. With these simplifications, equations 3.27 and 3.25 reduce to:

$$K(\chi, \psi) = \frac{1}{Re}\left\{D^2(\chi) - d_G V\left(d_G\psi + \chi\right)\right\} \tag{3.28}$$

$$\xi = d_G\psi + \chi = -\frac{D^2(\psi)}{V} \tag{3.29}$$

These equations have been solved in the Cartesian co-ordinate system by many authors to find solutions describing several well-known flows.

3.4.1 Cartesian co-ordinate system

In Cartesian co-ordinates (x, y, z), the scale factors become $h_1 = h_2 = h_3 = V = 1$. Given the restrictions $\chi = \chi(y)$ and $D^2(\chi) = 0, \chi = cy$, and equation 3.28 has the solution

$$\psi = \eta(y)\exp(\beta x) - \frac{cy}{d_G} \tag{3.30}$$

where $\eta(y)$ is an unknown function and $\beta = d_G^2/(cRe)$. Inserting equation 3.30 into 3.29 yields a single constraint equation:

$$\eta'' + \left(d_G + \beta^2\right)\eta = 0 \tag{3.31}$$

The solution is:

$$\eta(y) = c_s \sin\left(\sqrt{d_G + \beta^2}y\right) + c_c \cos\left(\sqrt{d_G + \beta^2}y\right) \tag{3.32}$$

Choosing the forms of the coefficients $\sqrt{d_G + \beta^2} = \lambda$, $c_s = A/\lambda$, $c_c = 0$, $c = -d_G$, $d_G = -Re\beta$ gives the classical Kovasznay flow [24]

$$\begin{aligned} \psi &= y - \frac{A}{\lambda}\sin(\lambda y)\exp(\beta x) \\ \beta &= -\frac{1}{2}\left[\sqrt{Re^2 + 4\lambda^2} - Re\right] \end{aligned} \tag{3.33}$$

where A and λ are arbitrary constants. A representative flow is shown in figure 3.1.

If the same coefficients are chosen as the Kovasznay solution except $c_s = -Ai/\lambda$, $c_c = -A/\lambda$, and $\sqrt{d_G + \beta^2} = -i\lambda$, Lin and Tobak's solution may be obtained [29]:

$$\begin{aligned} \psi &= y - \frac{A}{\lambda}\exp(\lambda y + \beta x) \\ \beta &= \frac{1}{2}\left[\sqrt{Re^2 - 4\lambda^2} + Re\right] \end{aligned} \tag{3.34}$$

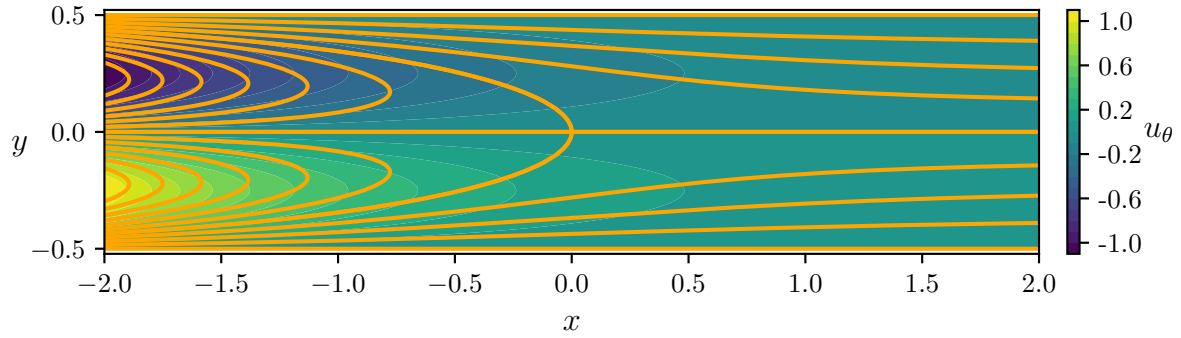

Figure 3.1: Kovasznay flow with $Re = 40$, $A = 1$, $\lambda = 2\pi$ and $d_F = 1$. The streamlines are those of the in-plane velocity field; contours are of the out-of-plane velocity component.

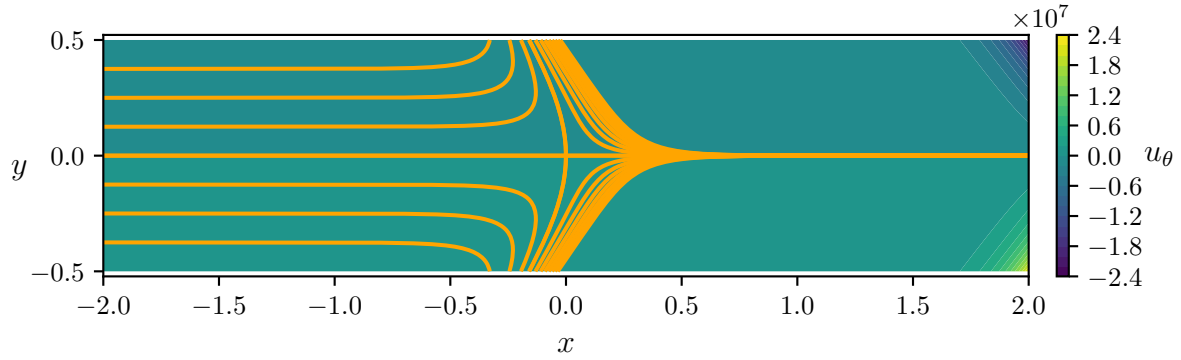

Figure 3.2: Wang's flow (equation 3.35) at $Re = 13$, $A = 1$, $\lambda = 2\pi$ and $d_F = 1$. The streamlines are those of the in-plane velocity field; contours are of the out-of-plane velocity component.

Wang's solution appears when the coefficients of Lin and Tobak's solution are selected, with the exception $c_c = 0$ [19]

$$\psi = y - \frac{A}{\lambda}\sinh(\lambda y)\exp(\beta x) \tag{3.35}$$
$$\beta = \frac{1}{2}\left[\sqrt{Re^2 - 4\lambda^2} + Re\right]$$

This flow is shown in figure 3.2.

Aside from the above solutions many other solutions have been obtained using the extended Beltrami method, working in Cartesian co-ordinates. Early solutions have been reviewed by Wang [2, 3] and Drazin and Riley [4]. More recently Chandna and Oku-Ukpong [30] have

obtained solutions by assuming polynomial forms of $\chi(x, y)$, which were later generalized by Islam et al. [31]. Hui [32], has retained the unsteady terms in their fomulation and arrived at a variety of solutions exponentially dependent on time. Jamil [33] assumed $\chi = -U\exp(ax + by)$ and found solutions depending only on $ax + by$, indicating the flow is unidirectional.

3.4.2 Plane polar co-ordinates

Working in polar co-ordinates (r, θ, z) we have $h_1 = 1$ and $h_2 = r$. If we assume $\chi = -a(d_G r^2 + 4)$, a general solution for ψ may be found using equation 3.28:

$$\psi = ar^2 + \eta(r)\exp\left(\frac{d_G\theta}{2aRe}\right) \tag{3.36}$$

where $\eta(r)$ is an unknown function. Inserting equation 3.36 into equation 3.29 yields

$$\eta'' + \frac{\eta'}{r} + d_G\left(1 + \frac{d_G^3}{4a^2Re^2r^2}\right)\eta = 0 \tag{3.37}$$

whose solution is

$$\eta(r) = c_{\eta 1}J_{\frac{id_G}{aRe}}\left(\sqrt{d_G}r\right) + c_{\eta 2}Y_{\frac{id_G}{aRe}}\left(\sqrt{d_G}r\right) \tag{3.38}$$

where $J_n(x)$ and $Y_n(x)$ are Bessel functions of order n of the first and second kinds, respectively. Note that the orders of each of the Bessel functions in equation 3.38 are imaginary. To eliminate the imaginary parts, we will leverage the identity $\mathrm{Im}\{J_{iv}(x)\} \approx \tanh(\pi v/2)\,\mathrm{Re}\{Y_{iv}(x)\}$ for small x [34], by choosing $c_{\eta 2} = -c_{\eta 1}\tanh(\pi d_G/(2aRe))i$. Noting that $\mathrm{Re}\{J_{iv}(x)\} \propto \mathrm{Im}\{Y_{iv}(x)\}$, the final solution may be written as:

$$\psi = ar^2 + c_\eta\,\mathrm{Re}\left\{J_{\frac{id_G}{aRe}}\left(\sqrt{d_G}r\right)\right\}\exp\left(\frac{d_G\theta}{2aRe}\right) \tag{3.39}$$

Since the exponential term containing θ cannot be made cyclic without introducing further imaginary components, equation 3.39 has limited utility since it may only be applied across a finite range of θ, where suitable boundary conditions must be applied at the domain boundaries (upper and lower bounds of θ).

3.5 3D Flows in Extruded Co-ordinate systems

We now shift the focus to 3D fluid motions in extruded co-ordinate systems ($h_3 = 1$), where equations 3.26 and 3.27 reduce to

$$K(\phi, \psi) = \frac{1}{Re}\left\{\nabla^2\phi - d_F V\left(d_H\psi + \chi\right)\right\} \tag{3.40}$$

$$K(\chi, \psi) = \frac{1}{Re}\left\{\nabla^2\chi - d_H V\left(d_H\psi + \chi\right)\right\} \tag{3.41}$$

while the vorticity definition 3.25 becomes

$$\xi = d_H\psi + \chi = -\frac{D^2(\psi)}{V} \tag{3.42}$$

where $d_H = d_F^2 + d_G$. One can immediately recognize that solutions to the 2D planar equations of section 3.4 are also solutions to equations 3.41 and 3.42, where d_G is relabelled d_H and the cross-flow, u_3, may be constructed from the solution to equation 3.40. In all cases, the function $\phi = d_F\chi/d_H$ is admissible, such that equations 3.40 and 3.41 are linearly dependant. As an example, Kovasznay's flow (equation 3.33) supports a cross flow

$$u_z = \sigma = d_F\psi + \phi = -\frac{d_F A}{\lambda}\sin(\lambda y)\exp(\beta x) \tag{3.43}$$

The cross-flow variation is shown in the colour contours in figure 3.1. A similar cross-flow solution may be constructed for Wang's solution (equation 3.35) and the cross-flow component has been included in figure 3.2.

3.6 Swirling Flow in Cylindrical Co-ordinates

In cylindrical co-ordinates (z, r, θ), the scale coefficients are $h_1 = h_2 = 1$ and $h_3 = r$. Note the present co-ordinate system is a permutation of the plane polar co-ordinate system in section 3.4.2; in that section, we studied motions in the r-θ plane where no axial variation is permitted. Here we study flows which vary in the meridional (z-r) plane, but are invariant with respect to θ. Equations 3.25, 3.26 and 3.27 become:

$$\xi = \frac{d_F^2}{r^2}\psi + d_G\psi + \chi = -\frac{D^2(\psi)}{r} \tag{3.44}$$

$$K(\phi,\psi) = \frac{1}{Re}\left\{r^2D^2(\phi) - rd_F\left(d_F^2\psi + d_Gr^2\psi + r^2\chi\right)\right\} \tag{3.45}$$

$$\begin{aligned} K(\chi,\psi) - \frac{2}{r^3}\left[(d_F\psi+\phi)\frac{\partial\phi}{\partial z} + d_F\phi\frac{\partial\psi}{\partial z}\right] = \\ = \frac{1}{Re}\left\{-r\left(d_F^2 + d_Gr^2\right)\left(\frac{d_F^2}{r^2}\psi + d_G\psi + \chi\right) + D^2\left(r^2\chi\right) + 4d_G\frac{\partial\psi}{\partial r}\right\} \end{aligned} \tag{3.46}$$

3.6.1 Vanishing centrifugal term

The second term in equation 3.46 is the centrifugal acceleration term; it represents the influence of angular momentum variation along the z axis on the motion in the meridional plane. In this subsection we will discuss a family of solutions which have a vanishing centrifugal term. To facilitate this, we begin with the assumptions $d_F = 0$ and $\phi = \phi(r)$. Equation 3.45 reduces to

$$-\frac{\mathrm{d}\phi}{\mathrm{d}r}\frac{\partial\psi}{\partial z} = \frac{r^2D^2(\phi)}{Re} \tag{3.47}$$

Since ψ is the only z-dependent term in equation 3.47, we must also have

$$\psi = z\Psi(r) + \delta(r) \tag{3.48}$$

to obtain non-trivial solutions. Inserting this corollary into equation 3.44 yields

$$\chi = \frac{z}{r^3}\left(-d_Gr^3\Psi - r\frac{\mathrm{d}^2\Psi}{\mathrm{d}r^2} + \frac{\mathrm{d}\Psi}{\mathrm{d}r}\right) + \frac{1}{r^3}\left(-d_Gr^3\delta - r\frac{\mathrm{d}^2\delta}{\mathrm{d}r^2} + \frac{\mathrm{d}\delta}{\mathrm{d}r}\right) \tag{3.49}$$

Furthermore, χ may be broken into two terms to accommodate equation 3.49:

$$\chi = zX(r) + Y(r) \tag{3.50}$$

Equation 3.49 can be broken into two equations to balance the coefficients of the z terms:

$$X(r) = \frac{1}{r^3}\left(-d_Gr^3\Psi - r\frac{\mathrm{d}^2\Psi}{\mathrm{d}r^2} + \frac{\mathrm{d}\Psi}{\mathrm{d}r}\right) \tag{3.51}$$

$$Y(r) = \frac{1}{r^3}\left(-d_Gr^3\delta - r\frac{\mathrm{d}^2\delta}{\mathrm{d}r^2} + \frac{\mathrm{d}\delta}{\mathrm{d}r}\right) \tag{3.52}$$

Using these reduced forms, equation 3.46 can be simplified with the help of Maple™ software [35]:

$$\zeta\Psi''' + \Psi'' + \frac{Re}{2}\left(\Psi\Psi'' - \Psi'^2\right) = C \tag{3.53}$$

$$\zeta\delta''' + \delta'' + \frac{Re}{2}\left(\Psi\delta'' - \Psi'\delta'\right) = D \tag{3.54}$$

$$\zeta = \frac{kRe\, r^2}{2}$$

where $'$ denotes differentiation with respect to ζ. Equations 3.53 and 3.54 are a system of ordinary differential equations in ζ, and qualify as a family of exact solutions under the criteria described in the introduction. Terrill and Thomas [36] have studied the case where $\delta = \Psi$ numerically with a constant suction/injection velocity at $\zeta = 1$, finding four solution branches. While Terrill and Thomas considered only Re and C as free parameters, the general case also requires choosing D, along with six additional parameters to fully define the boundary conditions. We will not describe this rich set of solutions here, but analyze one special case, appearing when we assume the function

$$\Psi = \frac{2}{Re}\zeta \tag{3.55}$$

which satisfies equation 3.53. Using this result, solving equation 3.54 (using Maple™ software) yields:

$$\delta = c_1 + c_2\left(\frac{\zeta^2}{2} + \zeta\right) - D\zeta + \frac{c_3}{2}\left(\zeta\left[\zeta + 2\right]\mathrm{E}_1(\zeta) - \left[\zeta + 1\right]\exp(-\zeta)\right) \tag{3.56}$$

where $\mathrm{E}_1(x) = -\int_{-x}^{\infty} \exp(t)/t\,\mathrm{d}t$ is the exponential integral. We can set $c_1 = 0$ and $D = c_2$, without loss of generality. Furthermore, equation 3.47 is used to evaluate ϕ and the solution is

$$\psi = \frac{2}{Re}\zeta z + \frac{c_2}{2}\zeta^2 + \frac{c_3}{2}\left(\zeta\left[\zeta + 2\right]\mathrm{E}_1(\zeta) - \left[\zeta + 1\right]\exp(-\zeta)\right) \tag{3.57}$$

$$u_\theta = \frac{\phi}{r} = \frac{\Gamma}{2\pi r}\left(1 - \exp(-\zeta)\right) \tag{3.58}$$

When $\delta = 0$, the well-known Burgers vortex [37] is recovered. If we instead retain c_2 and set $c_3 = 0$, Berker's solution is obtained [14], which describes two opposing streams with a

stagnation point at the origin. We find that Berker's solution supports the same circumferential velocity profile as Burgers vortex, as shown by the present analysis. Interestingly, the parameter d_G does not appear in the final solution, and has no bearing on the velocity field.

Other researchers have developed generalizations of the Burgers vortex. Sullivan [38] discovered that the ansatz $\Psi = 2\zeta/Re + A\,(1 - \exp(\beta\zeta))$ produces a solution describing a two-cell vortex (which the present formulation also admits) wherein the flow within a bounding radius recirculates along the z-axis while flow outside the bounding radius re-circulates away from the axis. Bellamy-Knights [39] have generalized Sullivan's solution to include unsteady motions of the bounding surface. More recently Craik [40] has thoroughly explored all solutions of the type $\Psi = Ar^2 + B\log r$ where A and B are constants or functions of time. When $B = 0$, many unsteady generalizations of Burgers vortex may be found. The solution described by equations 3.57 and 3.58 with $c_3 \neq 0$ is an extension to Burger's solution which has not yet been considered, however the axial velocity becomes singular at $r = 0$, due to the presence of $\mathrm{E}_1(\zeta)$. Consequently, it appears to have little practical use.

3.6.2 Swirling Kovasznay flow

Another solution may be found by assuming the auxiliary functions vary only with r; $\phi = \phi(r)$ and $\chi = \chi(r)$. With these guesses, solving equation 3.45 returns:

$$\psi = \eta(r)\exp(\beta(r)z) + \kappa(r) \tag{3.59}$$

$$\beta(r) = \frac{d_F r}{Re\,\phi'}\left(d_G r^2 + d_F^2\right) \tag{3.60}$$

$$\kappa(r) = \frac{\phi'' - \frac{\phi'}{r} - d_F r^2 \chi}{d_F\left(d_F^2 + d_G r^2\right)} \tag{3.61}$$

where $\eta(r)$ is an unknown function, and $'$ denotes differentiation with respect to r. Inserting equation 3.59 into equation 3.44 yields

$$\left(d_G r^2 + d_F^2\right)(\eta\exp(\beta z) + \kappa) + r^2\chi = \left(z\eta\frac{\beta'}{r} + \frac{\eta'}{r} - z^2\eta\,(\beta')^2 - z\eta\beta'' - 2z\eta'\beta' - \beta^2\eta - \eta''\right)\exp(\beta z) - \kappa'' + \frac{\kappa'}{r} \tag{3.62}$$

Since equation 3.62 contains no unknown functions of z, the coefficients of the terms containing z must sum to 0:

$$\exp(\beta z) \; : \; \eta'' - \frac{\eta'}{r} + \left(d_G r^2 + d_F^2 + \beta^2\right)\eta = 0 \tag{3.63}$$

$$z\exp(\beta z) \; : \; 2\eta'\beta' + \eta\beta'' - \frac{\eta}{r}\beta' = 0 \tag{3.64}$$

$$z^2\exp(\beta z) \; : \; \eta\left(\beta'\right)^2 = 0 \tag{3.65}$$

$$z^0 \; : \; \kappa'' - \frac{\kappa'}{r} + \left(d_G r^2 + d_F^2\right)\kappa + r^2\chi = 0 \tag{3.66}$$

Equation 3.65 is only satisfied when $\eta = 0$ or $\beta = \text{const}$. Taking the latter solution, equation 3.64 is immediately satisfied, and ϕ may be found using 3.60:

$$\phi = \frac{d_F r^2}{4Re\,\beta}\left(d_G r^2 + 2d_F^2\right) \tag{3.67}$$

where an integration constant has been set to 0 to avoid singular solutions of u_θ at $r = 0$. Equation 3.66 may be solved using equations 3.61 and 3.67:

$$\chi = \left(d_G r^2 + d_F^2\right)\left(\frac{c_{\chi 1}}{r^2} + c_{\chi 2}\right) + \frac{d_G^3 r^6 + d_F^6 - 8d_F^2 d_G}{4d_G Re\beta r^2} \tag{3.68}$$

Substituting the above results into equation 3.44 yields (after much simplification)

$$\left(4Rec_{\chi 2}\beta d_G^2 r^4 - 3d_F^2 d_G^2 r^4 - 4Rec_{\chi 1}\beta d_F^2 d_G - d_F^6 + 8d_F^2 d_G\right)\eta + d_G^2 r^3\eta' = 0 \tag{3.69}$$

Equations 3.63 and 3.69 are incompatible, and one must be eliminated to yield an admissible solution. A non-trivial solution arises when $d_G = 0$ and $c_{\chi 1} = \left(8 - d_F^4/d_G\right)/(4Re\beta)$, so equation 3.69 is satisfied. Then equation 3.63 may be solved:

$$\eta = c_{\eta 1} r J_1(\lambda r) + c_{\eta 2} r Y_1(\lambda r) \tag{3.70}$$

where $\lambda = \sqrt{d_F^2 + \beta^2}$, and J_n and Y_n are *nth*-order Bessel functions of the first and second kinds, respectively. Choosing $c_{\eta 2} = 0$ eliminates the singularity at the axis produced by $Y_1(0)$. The final solution reads:

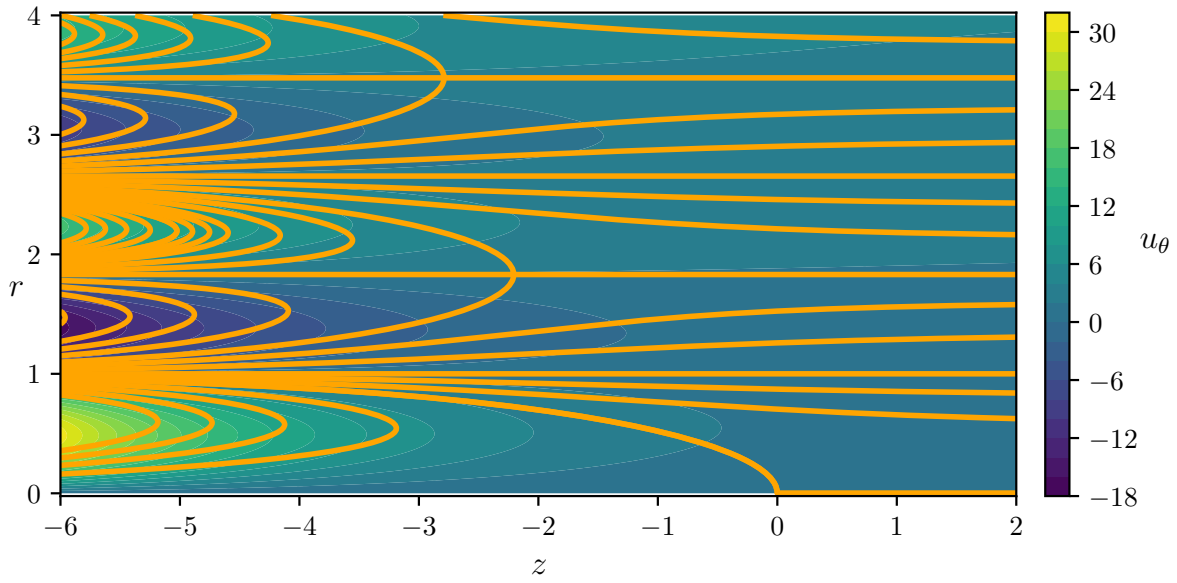

Figure 3.3: The swirling flow solution given by equations 3.71 and 3.72 with $Re_\theta = 50$, $\lambda = j_0$, $\Omega = 1$, and $c = 1$ where j_0 is the first root of $J_1(x)$. The streamlines are those of the meridional plane velocity field, and the colour contours correspond to the circumferential velocity distribution.

$$\psi = c\left[r^2 - \frac{2}{\lambda} r J_1(\lambda r)\exp(\beta z)\right] \tag{3.71}$$

$$\sigma = \Omega r^2 - \frac{2cd_F r}{\lambda} J_1(\lambda r)\exp(\beta z) \tag{3.72}$$

$$\beta = \frac{d_F^3}{2Re_\theta} \quad d_F = -\sqrt{\sqrt[3]{\frac{2}{9}b} - \sqrt[3]{\frac{32}{b}}} \quad b = Re_\theta^2\left(9\lambda^2 + \sqrt{3\left(16Re_\theta^2 + 27\lambda^4\right)}\right)$$

where setting $c_{\eta 1} = 2c/\lambda$ shifts the stagnation point to the origin, and $c = -c_{\chi 2}$. The Reynolds number has been replaced by $Re_\theta = Re\,\Omega^*$, and $\Omega = \Omega^* - cd_F$. A representative flow is shown in figure 3.3 and two 3D streamlines showing the recirculating and non-recirculating motions of the particles near the axis are visible in figure 3.4. These streamlines bear a strong resemblance to streamlines produced from computational fluid dynamics simulation results (see, for example figures 14 and 15 in Ref. [41]), although the present flow is incompressible whereas the flow inside the Ranque-Hilsch vortex tube is highly compressible. To the best of our knowledge, the solution described by equations 3.71 and 3.72 is new, although it may be

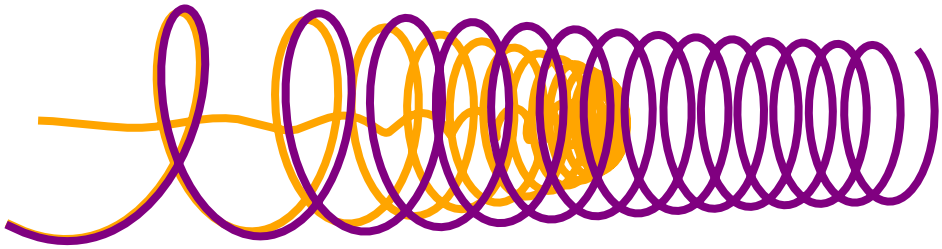

Figure 3.4: 3D streamlines of the solution given by equations 3.71 and 3.72 with $Re_\theta = 50$, $\lambda = j_0$, $\Omega = 40$, and $c = 1$ where j_0 is the first root of $J_1(x)$. The orange streamline ($\psi = -0.01872$) recirculates back along the axis, while the purple streamline ($\psi = 0.313919$) proceeds along the axis.

considered a generalization of the solution presented by Fatsis et. al [42]. The solution set may be viewed as the cylindrical analogue of Kovasznay's solution, as both flows are cellular, have a uniform base flow, and contain strong recirculation regions. The clear difference is that the above solution collapses to a uniform flow along the axis when the swirl vanishes, whereas the Kovasznay solution has no such dependence on the out-of-plane velocity. Since the sign of the Bessel function alternates between cells the sign of u_θ may become negative in the initial even numbered cells (assuming the cells are numbered sequentially statring with the innermost cell) depending on whether the first or second term in equation 3.72 dominates, meaning the bulk of the fluid in these cells can rotate in an opposite sense to its neighbours about the z-axis.

As shown in Figure 3.5 increasing Re_θ causes the recirculating regions to become increasingly slender; a behaviour also exhibited by Kovasznay flow. Furthermore the swirl magnitudes near the origin decrease with increasing Re_θ. Finally, the adjustment of the swirl factor Ω changes the magnitude of the 'background' rigid body swirl, and the circumferential velocity is increased with increasing radius, however it has no influence on the streamlines in the meridional plane.

While the counter-rotating annular cells visible in figure 3.3 are certainly interesting, the flow within the innermost cell is the most readily applicable to the study of various fluid machinery. First, the present solution might be applied to the study of cyclonic separators, which

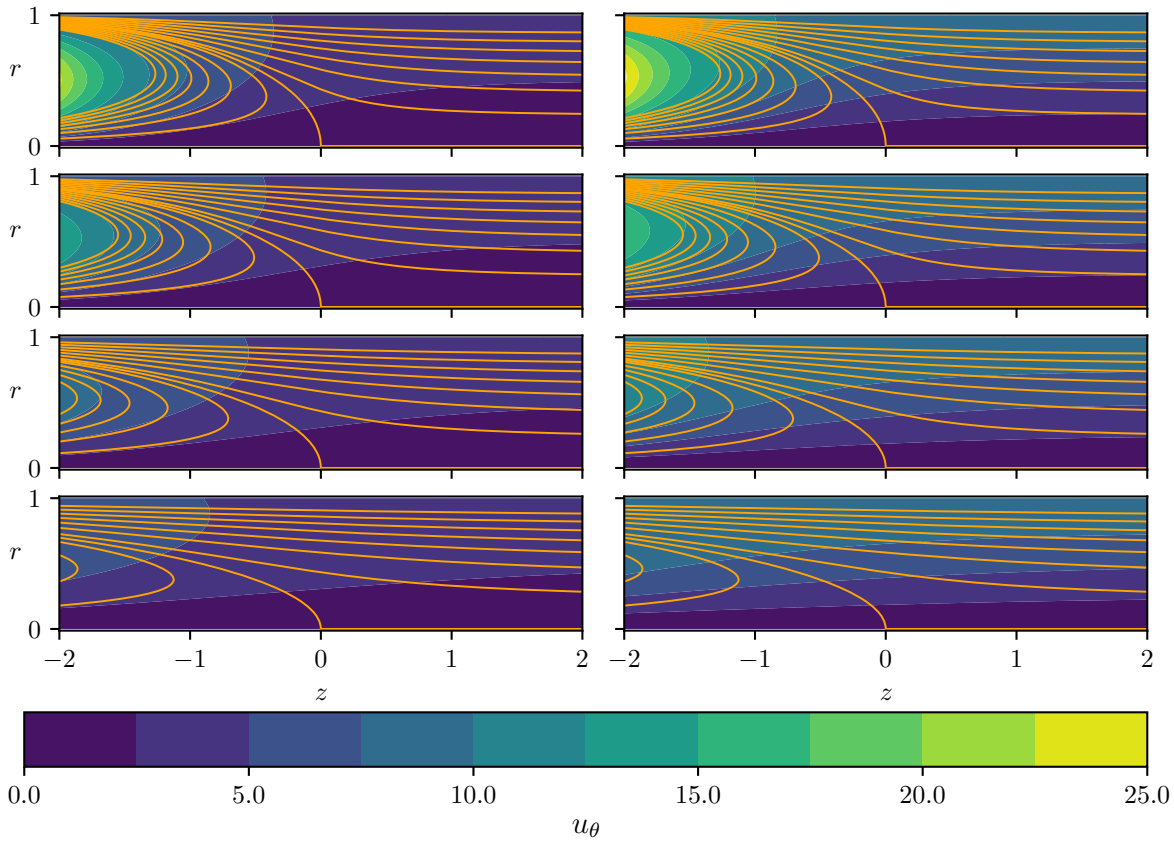

Figure 3.5: Plots are described by the caption to figure 3.3 except $Re_\theta = 5, 10, 20, 50$ for each row, and $\Omega = 1, 5$ for each column.

are frequently analyzed using exact techniques, however viscous effects have often been neglected in the search for exact solutions (cf. Bloor and Ingham [43]). In a related application, Maicke et al. [44] have numerically solved the axisymmetric Euler equations to study compressible flows in a bi-directional vortex, where swirling fluid is injected near the periphery of a tube and is withdrawn near the axis at the same axial location. An important finding of Maicke et al. is that, for high swirl flows, compressibility appears to have little influence on the solution field. The present incompressible solution may be readily applied to their problem when Re_θ is small. Finally, the present solution bears strong similarities to axisymmetric Ranque-Hilsch flow. Most importantly, it includes the effect of viscous forces, which has been shown to be the dominant energy transfer mechanism across the stagnation streamline [45, 46].

3.7 Summary and Discussion

In the present work the extended Beltrami approach first presented by Wang [19] has been reviewed and extended. We have shown that our general formulation (equations 3.25 - 3.27) can be used to analyze viscous three-dimensional flows in planar and revolved co-ordinate systems. Specifically, we are able to recover all known 2D planar solutions, and have discovered that each one supports an out-of-plane velocity distribution which is closely related to the streamfunction solution. Furthermore, we have analyzed the equations of motion in cylindrical co-ordinates with a vanishing centrifugal term, finding a new generalization of Burger's vortex. Finally, we have discovered a new swirling flow solution describing flow resembling Kovasznay flow, and also bears strong similarities to Ranque-Hilsch flow.

Comparing the planar results of sections 3.4 and 3.5 with the axisymmetric flows of section 3.6, we find that the planar solutions can be separated into the in-plane and out-of-plane motions, where the in-plane velocities are unaffected by the out of plane motion. This is because the centrifugal term, given by $K(\sigma/h_3^2, \sigma)$ vanishes for planar flows, and only a one-way coupling exists between the vorticity and out-of-plane momentum equations. In contrast, the centrifugal term does not vanish, in general, for axisymmetric flows because $h_3 \neq 1$. If the swirl velocity is independent of z, however, the equations describe an important sub-class of flows in which the meridional plane motion is independent of the swirl, some of which are

described in section 3.6.1. In contrast, the swirling flow solution given by equations 3.71 and 3.72 appears to be the first of its kind, in that it is a 3D axisymmetric Navier-Stokes solution with a non-vanishing centrifugal term.

Appendix

Here we aim to develop the third components of the momentum and vorticity equations 3.2 and 3.3, respectively, in terms of $\sigma = h_3 u_3$ and $\xi = \omega_3/h_3$. Beginning with equation 3.2, the transient term may be written as

$$\frac{\partial \mathbf{u}}{\partial t} = \frac{1}{h_2 h_3}\frac{\partial^2 \psi}{\partial x_2 \partial t}\hat{\mathbf{e}}_1 - \frac{1}{h_1 h_3}\frac{\partial^2 \psi}{\partial x_1 \partial t}\hat{\mathbf{e}}_2 + \frac{\partial u_3}{\partial t}\hat{\mathbf{e}}_3 \tag{3.73}$$

The advection term is given by

$$\begin{aligned}
(\mathbf{u}\cdot\boldsymbol{\nabla})\,\mathbf{u} = \boldsymbol{\nabla}\left(\frac{\mathbf{u}\cdot\mathbf{u}}{2}\right) + \omega \times \mathbf{u} = \\
= \boldsymbol{\nabla}\left(\frac{\mathbf{u}\cdot\mathbf{u}}{2}\right) + \frac{1}{h_1}\left[\xi\frac{\partial\psi}{\partial x_1} - \frac{\sigma}{h_3^2}\frac{\partial\sigma}{\partial x_1}\right]\hat{\mathbf{e}}_1 + \frac{1}{h_2}\left[\xi\frac{\partial\psi}{\partial x_2} - \frac{\sigma}{h_3^2}\frac{\partial\sigma}{\partial x_2}\right]\hat{\mathbf{e}}_2 + \\
+ \frac{1}{h_1 h_2 h_3^2}\left(\frac{\partial\sigma}{\partial x_1}\frac{\partial\psi}{\partial x_2} - \frac{\partial\sigma}{\partial x_2}\frac{\partial\psi}{\partial x_1}\right)\hat{\mathbf{e}}_3 = \\
= \boldsymbol{\nabla}\left(\frac{\mathbf{u}\cdot\mathbf{u}}{2}\right) + \frac{1}{h_1}\left[\xi\frac{\partial\psi}{\partial x_1} - \frac{\sigma}{h_3^2}\frac{\partial\sigma}{\partial x_1}\right]\hat{\mathbf{e}}_1 + \frac{1}{h_2}\left[\xi\frac{\partial\psi}{\partial x_2} - \frac{\sigma}{h_3^2}\frac{\partial\sigma}{\partial x_2}\right]\hat{\mathbf{e}}_2 + \frac{K(\sigma,\psi)}{h_3 V}\hat{\mathbf{e}}_3
\end{aligned} \tag{3.74}$$

The pressure term is written as

$$-\boldsymbol{\nabla} p = -\frac{1}{h_1}\frac{\partial p}{\partial x_1}\hat{\mathbf{e}}_1 - \frac{1}{h_2}\frac{\partial p}{\partial x_2}\hat{\mathbf{e}}_2 \tag{3.75}$$

The viscous term may be written as

$$\begin{aligned}
\frac{\nabla^2\mathbf{u}}{Re} = -\frac{\boldsymbol{\nabla}\times\omega}{Re} = \frac{1}{Re\,V}\left(-h_1\frac{\partial\left(h_3\omega_3\right)}{\partial x_2}\hat{\mathbf{e}}_1 + h_2\frac{\partial\left(h_3\omega_3\right)}{\partial x_1}\hat{\mathbf{e}}_2 + h_3\left[\frac{\partial\left(h_1\omega_1\right)}{\partial x_2} - \frac{\partial\left(h_2\omega_2\right)}{\partial x_1}\right]\hat{\mathbf{e}}_3\right) = \\
= -\frac{h_1}{Re\,V}\frac{\partial\left(h_3^2\xi\right)}{\partial x_2}\hat{\mathbf{e}}_1 + \frac{h_2}{Re\,V}\frac{\partial\left(h_3^2\xi\right)}{\partial x_1}\hat{\mathbf{e}}_2 + \frac{h_3}{Re\,V}D^2(\sigma)\hat{\mathbf{e}}_3
\end{aligned} \tag{3.76}$$

Re-assembling the $\hat{\mathbf{e}}_3$ components of equations 3.73-3.76 and multiplying through by $h_3 V$ yields equation 3.9. The vorticity equation terms are similarly developed here. The transient term is the time derivative of equation 3.7

$$\frac{\partial \omega}{\partial t} = \frac{1}{h_2 h_3}\frac{\partial^2 \sigma}{\partial x_2 \partial t}\hat{\mathbf{e}}_1 - \frac{1}{h_1 h_3}\frac{\partial^2 \sigma}{\partial x_1 \partial t}\hat{\mathbf{e}}_1 + h_3 \frac{\partial \xi}{\partial t}\hat{\mathbf{e}}_3 \tag{3.77}$$

Taking the curl of 3.74 gives the vorticity equation advection term:

$$\begin{aligned}
\boldsymbol{\nabla} \times (\omega \times \mathbf{u}) = \\
= \frac{h_1}{V}\left[\frac{\partial}{\partial x_2}\left(\frac{K(\sigma,\psi)}{V}\right)\right]\hat{\mathbf{e}}_1 - \frac{h_2}{V}\left[\frac{\partial}{\partial x_1}\left(\frac{K(\sigma,\psi)}{V}\right)\right]\hat{\mathbf{e}}_2 + \\
+ \frac{h_3}{V}\left[\frac{\partial}{\partial x_1}\left(\xi\frac{\partial \psi}{\partial x_2} - \frac{\sigma}{h_3^2}\frac{\partial \sigma}{\partial x_2}\right) - \frac{\partial}{\partial x_2}\left(\xi\frac{\partial \psi}{\partial x_1} - \frac{\sigma}{h_3^2}\frac{\partial \sigma}{\partial x_1}\right)\right]\hat{\mathbf{e}}_3 = \\
= \frac{h_1}{V}\left[\frac{\partial}{\partial x_2}\left(\frac{K(\sigma,\psi)}{V}\right)\right]\hat{\mathbf{e}}_1 - \frac{h_2}{V}\left[\frac{\partial}{\partial x_1}\left(\frac{K(\sigma,\psi)}{V}\right)\right]\hat{\mathbf{e}}_2 + \frac{h_3}{V}\left[K(\xi,\psi) - K\left(\frac{\sigma}{h_3^2},\sigma\right)\right]\hat{\mathbf{e}}_3
\end{aligned} \tag{3.78}$$

Since, the curl of term 3.75 is 0, the pressure does not appear in the vorticity equation. Finally, taking the curl of 3.76 gives the viscous terms

$$\begin{aligned}
-\frac{\boldsymbol{\nabla} \times (\boldsymbol{\nabla} \times \omega)}{Re} = \\
= \frac{h_1}{Re\, V}\left[\frac{\partial}{\partial x_2}\left(\frac{h_3^2}{V}D^2(\sigma)\right)\right]\hat{\mathbf{e}}_1 - \frac{h_2}{Re\, V}\left[\frac{\partial}{\partial x_1}\left(\frac{h_3^2}{V}D^2(\sigma)\right)\right]\hat{\mathbf{e}}_2 + \\
+ \frac{h_3}{Re\, V}\left(\frac{\partial}{\partial x_1}\left[\frac{h_2}{h_1 h_3}\frac{\partial\left(h_3^2\xi\right)}{\partial x_1}\right] + \frac{\partial}{\partial x_2}\left[\frac{h_1}{h_2 h_3}\frac{\partial\left(h_3^2\xi\right)}{\partial x_2}\right]\right)\hat{\mathbf{e}}_3 = \\
= \frac{h_1}{Re\, V}\left[\frac{\partial}{\partial x_2}\left(\frac{h_3^2}{V}D^2(\sigma)\right)\right]\hat{\mathbf{e}}_1 - \frac{h_2}{Re\, V}\left[\frac{\partial}{\partial x_1}\left(\frac{h_3^2}{V}D^2(\sigma)\right)\right]\hat{\mathbf{e}}_2 + \frac{h_3}{Re\, V}D^2\left(h_3^2\xi\right)\hat{\mathbf{e}}_3
\end{aligned} \tag{3.79}$$

Reassembling the $\hat{\mathbf{e}}_3$ components of 3.77 - 3.79 and multiplying through by V/h_3 yields equation 3.10. While the $\hat{\mathbf{e}}_1$ and $\hat{\mathbf{e}}_2$ terms may also be assembled into equations, both of these are linearly dependant on equation 3.9, and are therefore superfluous.

Bibliography

[1] C. Pozrikidis, *Introduction to theoretical and computational fluid dynamics*. New York, NY, USA: Oxford university press, 2nd ed., 2011.

[2] C.-Y. Wang, "Exact Solutions of the Unsteady Navier-Stokes Equations," *Applied Mechanics Reviews*, vol. 42, pp. S269–S282, 11 1989.

[3] C.-Y. Wang, "Exact Solutions Of The Steady-State Navier-Stokes Equations," *Annu. Rev. Fluid Mech.*, vol. 23, no. 1, pp. 159–177, 1991.

[4] P. G. Drazin and N. Riley, *The Navier-Stokes Equations: A Classification of Flows and Exact Solutions*. Cambridge: Cambridge University Press, 1st ed., 2006.

[5] A. D. Polyanin and S. N. Aristov, "A new method for constructing exact solutions to three-dimensional Navier-Stokes and Euler equations," *Theoretical Foundations of Chemical Engineering*, vol. 45, no. 6, pp. 885–890, 2011.

[6] A. D. Polyanin and A. I. Zhurov, "Functional and generalized separable solutions to unsteady Navier-Stokes equations," *International Journal of Non-Linear Mechanics*, vol. 79, pp. 88–98, 2016.

[7] M. Kumar and R. Kumar, "On some new exact solutions of incompressible steady state Navier-Stokes equations," *Meccanica*, vol. 49, no. 2, pp. 335–345, 2014.

[8] H. S. Tsien, "Symmetrical Joukowsky Airfoils in Shear Flow," *Quarterly of Applied Mathematics*, vol. 1, no. 2, pp. 130–148, 1943.

[9] C.-Y. Wang, "Exact solutions of the Navier-Stokes equations- the generalized Beltrami flows, review and extension," *Acta Mechanica*, vol. 81, no. 1-2, pp. 69–74, 1990.

[10] M. J. M. Hill, "VI. On a spherical vortex," *Philosophical Transactions of the Royal Society A: Mathematical, Physical and Engineering Sciences*, vol. 185, no. 1, pp. 213–245, 1894.

[11] V. O'Brien, "Steady spheroidal vortices—More exact solutions to the Navier-Stokes equation," *Quarterly of Applied Mathematics*, vol. 19, no. 2, pp. 163–168, 1961.

[12] M. Fujimoto, S. Science, K. Uehara, and S. Yanase, "Vortex solutions of the generalized Beltrami flows to the Euler equations," *ArXiv: 1501.05620*, 2015.

[13] S. P. Joseph, "Polynomial solutions and other exact solutions of axisymmetric generalized Beltrami flows," *Acta Mechanica*, vol. 229, pp. 2737–2750, 7 2018.

[14] R. Berker, *Intégration des équations du mouvement d'un fluide visqueux incompressible*. Berlin: Springer, 1963.

[15] R. M. Terrill, "An exact solution for flow in a porous pipe," *ZAMP Zeitschrift fur Angewandte Mathematik und Mechanik*, vol. 33, no. 4, pp. 547–552, 1982.

[16] G. Saccomandi, "Some exact pseudo-plane solutions of the first kind for the Navier-Stokes equations," *ZAMP Zeitschrift fur Angewandte Mathematik und Mechanik*, vol. 45, no. 6, pp. 978–985, 1994.

[17] G. Saccomandi, "Some unsteady exact pseudo-plane solutions for the Navier-Stokes equations," *Meccanica*, vol. 29, no. 3, pp. 261–269, 1994.

[18] S. Weinbaum and V. O'Brien, "Exact Navier-Stokes Solutions Including Swirl and Cross Flow," *Physics of Fluids*, vol. 10, no. 7, pp. 1438–1447, 1967.

[19] C.-Y. Wang, "On a Class of Exact Solutions of the Navier-Stokes Equations," *Journal of Applied Mechanics*, vol. 33, pp. 696–698, 9 1966.

[20] J. M. Lopez, "Axisymmetric vortex breakdown Part 1. Confined swirling flow," *Journal of Fluid Mechanics*, vol. 221, p. 533, 1990.

[21] A. D. Polyanin, "Exact solutions to the Navier-Stokes equations with generalized separation of variables," *Doklady Physics*, vol. 46, no. 10, pp. 726–731, 2001.

[22] W. S. Lewellen, "A solution for three-dimensional vortex flows with strong circulation," *Journal of Fluid Mechanics*, vol. 14, no. 3, pp. 420–432, 1962.

[23] R. Granger, "Steady three-dimensional vortex flow," *Journal of Fluid Mechanics*, vol. 25, pp. 557–576, 7 1966.

[24] L. I. G. Kovasznay, "Laminar flow behind a two-dimensional grid," *Proc. Camb. Phil. Soc.*, vol. 44, no. May, pp. 58–62, 1948.

[25] G. Taylor, "On the decay of vortices in a viscous fluid," *The London, Edinburgh, and Dublin Philosophical Magazine and Journal of Science*, vol. 46, pp. 671–674, 10 1923.

[26] N. Leprovost, B. Dubrulle, and P. H. Chavanis, "Dynamics and thermodynamics of axisymmetric flows: Theory," *Physical Review E - Statistical, Nonlinear, and Soft Matter Physics*, vol. 73, no. 4, pp. 1–18, 2006.

[27] G. K. Batchelor, "Axial flow in trailing line vortices," *Journal of Fluid Mechanics*, vol. 20, p. 645, 12 1964.

[28] S. Bhattacharya, "Exact analytical solutions for steady three-dimensional inviscid vortical flows," *Journal of Fluid Mechanics*, vol. 590, pp. 147–162, 2007.

[29] S. P. Lin and M. Tobak, "Reversed flow above a plate with suction," *AIAA Journal*, vol. 24, pp. 334–335, 2 1986.

[30] O. P. Chandna and E. O. Oku-Ukpong, "Flows for chosen vorticity functions - exact solutions of the Navier-Stokes equations," *International Journal of Mathematics and Mathematical Sciences*, vol. 17, no. 1, pp. 155–164, 1994.

[31] S. Islam, C.-y. Zhou, and X.-j. Ran, "Exact solutions for different vorticity functions of couple stress fluids," *Journal of Zhejiang University-SCIENCE A*, vol. 9, no. 5, pp. 672–680, 2008.

[32] W. H. Hui, "Exact solutions of the unsteady two-dimensional Navier-Stokes equations," *ZAMP Zeitschrift fur Angewandte Mathematik und Mechanik*, vol. 38, no. 5, pp. 689–702, 1987.

[33] M. Jamil, "A Class of Exact Solutions to Navier-Stokes Equations for the Given Vorticity Basic governing equations," *Journal of Nonlinear Science*, vol. 9, no. 3, pp. 296–304, 2010.

[34] T. M. Dunster, "Bessel Functions of Purely Imaginary Order, with an Application to Second-Order Linear Differential Equations Having a Large Parameter," *SIAM Journal on Mathematical Analysis*, vol. 21, no. 4, pp. 995–1018, 1990.

[35] Maplesoft: a division of Waterloo Maple Inc., "Maple 2018.1," 2018.

[36] R. M. Terrill and P. W. Thomas, "On laminar flow through a uniformly porous pipe," *Applied Scientific Research*, vol. 21, pp. 37–67, 1 1969.

[37] J. Burgers, "A Mathematical Model Illustrating the Theory of Turbulence," *Advances in Applied Mechanics*, vol. 1, pp. 171–199, 1 1948.

[38] R. D. Sullivan, "A Two-Cell Vortex Solution of the Navier-Stokes Equations," *Journal of the Aerospace Sciences*, vol. 26, pp. 767–768, 11 1959.

[39] P. G. Bellamy-Knights, "An unsteady two-cell vortex solution of the Navier—Stokes equations," *Journal of Fluid Mechanics*, vol. 41, no. 3, pp. 673–687, 1970.

[40] A. D. D. Craik, "Exact vortex solutions of the Navier - Stokes equations with axisymmetric strain and suction or injection," *Journal of Fluid Mechanics*, vol. 626, pp. 291–306, 2009.

[41] T. Farouk and B. Farouk, "Large eddy simulations of the flow field and temperature separation in the Ranque-Hilsch vortex tube," *International Journal of Heat and Mass Transfer*, vol. 50, no. 23-24, pp. 4724–4735, 2007.

[42] A. Fatsis, J. Statharas, A. Panoutsopoulou, and N. Vlachakis, "A new class of exact solutions of the Navier-Stokes equations for swirling flows in porous and rotating pipes," *WIT Transactions on Engineering Sciences*, vol. 69, pp. 67–78, 2010.

[43] M. I. G. Bloor and D. B. Ingham, "The flow in industrial cyclones," *Journal of Fluid Mechanics*, vol. 178, no. 1987, p. 507, 1987.

[44] B. A. Maicke, O. M. Cecil, and J. Majdalani, "On the compressible bidirectional vortex in a cyclonically driven Trkalian flow field," *Journal of Fluid Mechanics*, vol. 823, pp. 755–786, 2017.

[45] N. F. Aljuwayhel, G. F. Nellis, and S. A. Klein, "Parametric and internal study of the vortex tube using a CFD model," *International Journal of Refrigeration*, vol. 28, no. 3, pp. 442–450, 2005.

[46] N. J. Dyck and A. G. Straatman, "Energy Transfer Mechanisms in the Ranque-Hilsch Vortex Tube," in *2018 Canadian Society for Mechanical Engineering (CSME) International Congress*, (Toronto), 2018.

Chapter 4

The Impact of Boundary Condition and Model Parameters on CFD Simulations of the Ranque-Hilsch Vortex Tube

4.1 Introduction

The Ranque-Hilsch vortex tube (RHVT) is a simple mechanical device with no moving parts capable of separating a supply of compressed fluid into hot and cold streams through a process called temperature separation. A representative schematic of the RHVT is shown in Fig. 4.1. Presently, the RHVT is being used in a variety of industrial applications, many of which harness the cold stream for cooling where a refrigeration system would be impractical, such as cooling of electrical cabinets [1]. The RHVT is also capable of separating mixtures of gases into their components [2]. A recent review has detailed other current and prospective applications of the RHVT [3].

Despite the large number of scientific studies documenting the temperature separation effect, there is no consensus on the mechanism responsible for temperature separation in the RHVT [4, 5]. Recently, Computational Fluid Dynamics (CFD) software has been employed to model the flow inside the RHVT, and predict temperature separation.

Throughout this work, we emphasize the importance of the hydrodynamic boundary con-

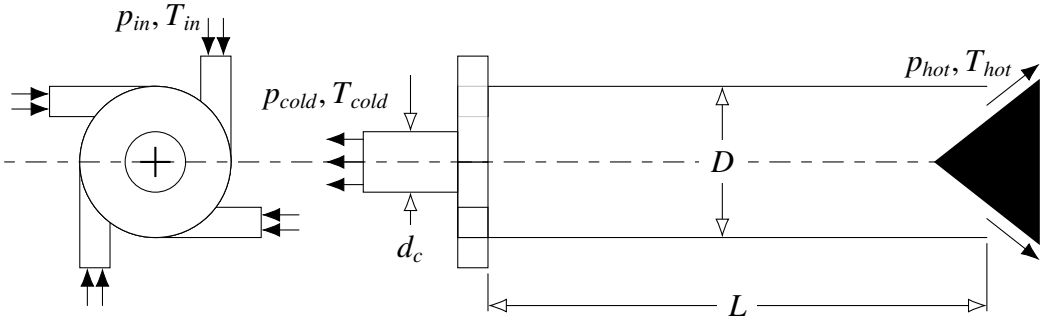

Figure 4.1: A schematic of a typical counter-flow Ranque-Hilsch vortex tube with four inlet nozzles, an annular hot exit created by a conical plug, and an axial cold exit

ditions (BCs) applied to CFD models of the RHVT. Here, we introduce a notation to concisely refer to each BC combination; we follow the template ⟨inlet BC⟩-⟨cold outlet BC⟩-⟨hot outlet BC⟩. We use P to denote a pressure BC, M to denote a mass flow BC, and V to denote a velocity BC. For example the M-P-M configuration indicates the inlet mass flow, cold exit pressure, and hot exit mass flow have been fixed.

Early on, Fröhlingsdorf and Unger [6] simulated vortex tube flow using an axisymetric model and a V-P-P configuration, comparing both circumferential velocity profiles and measurements of temperature separation with the measurements of Bruun [7]. Using a regularly spaced orthogonal grid Fröhlingsdorf and Unger obtained excellent agreement with Bruun, but only after implementing a specialized turbulence model developed by Keyes [8], assigning the same turbulent eddy viscosity for the entire flow domain, and adjusting the turbulent Prandtl number to 10 times its typical magnitude.

Aljuwayhel et al. [9] conducted experiments and simulations on a VT of aspect ratio 10, using ANSYS Fluent with a 2D axisymetric model in the P-P-P configuration, comparing the k-ε and RNG k-ε turbulence models. Both turbulence models were capable of predicting temperature separation, matching hot and cold exit experimental measurements of temperature separation within 2 K. Aljuwayhel et al. also post-processed the results to identify the streamline separating the hot and cold exits, computed the total energies transferred across the streamline, and found that shear, also known as work transfer, from the cold stream to the hot stream was the dominant form of energy transfer. Shamsoddini and Nezhad [10] have also studied the vortex tube of Aljuwayhel et al. using a 3D model, ANSYS Fluent and the M-

P-P configuration, showing that increasing the number of nozzles in the vortex tube increases temperature separation, finding strong agreement with experimentally observed temperature separation.

Skye et al. [11] have performed experiments using a commercial vortex tube (the Exair® 708 slpm), and have reported detailed measurements of the internal dimensions of the vortex tube (VT) in order to simulate the flow using an axisymetric CFD model using a M-P-M BC configuration and the k-ε turbulence model. While the CFD results accurately reflected the trends seen in the experimental results, the CFD model under-predicted the cold and hot exit temperature separations by approximately 16 K and 4 K, respectively. Furthermore, the CFD model over-predicted the average pressure at the hot outlet by 20 kPa. Possible reasons for these discrepancies were not discussed.

Other researchers have performed their own CFD studies of the same VT studied by Skye et al., including Kandil and Abdelghany [12, 13], who also used Fluent to perform axisymetric CFD simulations with a M-P-P configuration, using the k-ε turbulence model (among other models). The outlet pressures were weighted such that the pressure profiles were allowed to vary across the outlets, but the averages were maintained at specified values. It is unclear whether the CFD model was checked to see if the same outlet pressures produced the same mass flow splits observed by Skye et al. Regardless, excellent agreement with the experimental results of Skye et al. was achieved in the cold mass fraction range $0.35 < \lambda < 0.8$.

Notably, Skye et. al [11], Kandil et. al [12], and Dyck and Straatman [14] have observed entrainment of flow into their axisymetric CFD domains near the axis of the cold exit, and it is unclear from these studies whether the presence of this recirculation region is caused by an inaccuracy in the numerical models, or whether it is physically accurate.

Thakare and Parekh [4] also studied the vortex tube of Skye et al., using the same computational setup as Kandil and Abdelghany, except that they have applied an atmospheric BC to the cold exit, rather than the experimentally observed boundary pressures reported by Skye et al. Later, Thakare and Parekh [15] also performed experimental studies of the Exair® 708 slpm VT, and varied the inlet pressure, but only measured pressures at the inlet and cold outlet. In the same work using a similar CFD model to Skye et al., Thakare and Parekh used a M-P-M BC configuration, but did not indicate how the pressure at the hot exit was determined.

They additionally tested the influence of insulating the RHVT, discovering that the presence of insulation increased the observed temperature separation.

Rafiee and Sadeghiazad [16] also studied the Exair® 708 slpm VT using Fluent, using a 3D model with 6 inlet channels and the M-P-P configuration, to test the influence of different turbulence models, finding the Reynolds Stress Model (RSM) yielded the most accurate results, agreeing well with the experiments of Skye et al. Rafiee and Sadeghiazad also advocated for the use of Pressure-Far-Field BCs, demonstrating that accurate results can be obtained simply by adjusting the cold outlet area. It is unclear how the Pressure-Far-Field BCs were implemented, or if they are consistent with the experiments conducted by Skye et al.

A set of experiments has been carried out by Dincer et al. [17, 18], who studied a VT of aspect ratio 14.78 and obtained a large amount of data. Their experimental setup included instrumentation for the temperature at all boundaries and static pressure instrumentation at the inlet. They plotted temperature separation against the cold mass fraction, showing the variation with the hot plug position, inlet pressure and d/D ratio. The reports of Dincer et al. do not include concomitant information needed to replicate the experiment, such as outlet pressures or the total mass flow rate.

Nevertheless, several authors have attempted to replicate the results of Dincer et al. using CFD; Baghdad, Ouadha and others [19, 20] used ANSYS Fluent to simulate the flow through a 1/4 model of the VT with a P-P-M configuration (the mass fraction leaving the hot exit was fixed, while the total mass flow rate was unconstrained). They obtained good agreement with experimental results using the RSM turbulence model, showing the influence of variable thermo-physical properties to be negligible, and evaluating the exergy efficiency of the VT. In a later work Baghdad et al. [21] used a similar model to investigate the effects of non-adiabatic wall BCs in the vortex tube using a P-P-P configuration and the k-ε turbulence model, wherein the cold outlet pressure was set to atmospheric, and the hot exit pressure was adjusted to obtain the desired cold mass fraction. They found the model was sensitive to the thermal BC at the wall: CFD cases assuming a constant heat transfer coefficient at the tube wall based on the correlation developed by Churchill and Chu under-predicted temperature separation, while CFD cases assuming adiabatic wall conditions over-predicted temperature separation.

Zhang et al. [22] simulated the VT studied by Dincer et al. using a 3D model in AN-

SYS Fluent with a P-P-P configuration to investigate the precessing vortex core: an unsteady, screw-like flow structure which rotates about the tube axis. The predicted temperature separation agreed within 3 K of the experimental results. They interpreted the precessing core as a vibrating boundary layer, and claimed it is the primary energy transfer mechanism.

Other researchers have conducted a substantial number of experiments on VTs, with intentions of examining and improving the energy separation phenomenon. Celik et al. [23] conducted detailed experiments on a commercially available VT, with an experimental setup that included instrumentation at all three boundaries for measuring the temperature, pressure and mass flow rate. Celik et al.'s experiments analyzed the effect of the aspect ratio (L/D) and the ratio between the cold orifice and tube diameters (d_c/D). However, the reported data does not detail the exact temperature, pressure, and mass flow rate at all three boundaries for a specific data point. Kumar et al. [24] performed further experiments on a VT, focusing on the effect of insulating the tube. The experimental setup included instrumentation for pressure, temperature, mass flow rate, and relative humidity at the inlet and cold outlet, while at the hot outlet, there was only instrumentation for the temperature. Kırmacı [25] conducted VT experiments comparing the effects of using different working fluids and varying the number of inlet nozzles on the temperature separation between the outlets for a cold mass fraction of 0.5. The experimental setup allowed for measuring the pressure at all three boundaries; however, the experimental setup does not include measurements of the temperature and mass flow rate at the hot and cold outlets. Furthermore, Kırmacı does not report the specific temperatures and pressures at the outlets.

Many researchers have proposed theories on the mechanism of temperature or energy separation, and these theories have been collected in recent review papers [26, 4]. Ahlborn and Groves [27, 28] observed re-circulation regions within the VT, and suggested that each of these regions works as a heat pump, to receiving heat at low pressure from the cold stream and delivering heat to the hot stream at a higher pressure. Reynolds [29] has theorized that turbulence is responsible for energy separation using a simplified model of a compressible lump of fluid exchanging energy as oscillates radially. Other researchers including Hilsch [30] have argued that energy separation occurs because energy is transferred radially outward due to viscous shearing from the high-angular-velocity inner layers to the more sluggish outward moving layers.

A common theme amongst many experimental studies of the RHVT is a lack of specific information on the measurement stations, including the positions and orientations of the measurement probes and the local geometry of the domain. A brief hand calculation is useful in demonstrating the potential sensitivity of probe placement. In compressible flows, such as those observed in the RHVT, it is useful to work with total thermodynamic properties, such as the total temperature

$$T_0 = T_s + \frac{V^2}{2c_p} \tag{4.1}$$

where T_s is the static temperature, V is the local velocity, and c_p is the heat capacity of the gas. Consider air flowing at a constant mass flow rate of 3.5 $\mathrm{g\,s^{-1}}$ through the cold exit tube of a RHVT with a radius of 2.5 mm at an absolute pressure of 110 kPa and static temperature of 280 K. Under these conditions, usage of the ideal gas law and the continuity equation indicates the average axial flow speed is 147 $\mathrm{m\,s^{-1}}$, and the magnitude of the dynamic component of temperature is $V^2/(2c_p) = 6.2\,\mathrm{K}$. Moreover, for this simple calculation we have assumed that the flow is purely in the axial direction, while the velocities in the RHVT often have significant circumferential velocity components. If a temperature probe is mounted near the wall of the cold exit tube, the circumferential velocity component will be large, introducing additional uncertainty into the temperature measurement. Alternatively, if the probe extends to the tube axis where the circumferential velocity component vanishes, the probe leads and any supporting structure will partially block the flow, and other errors will be incurred. Despite the marked difference between these static and total temperatures, we have found no works in the literature which clearly indicate whether the static, total, or intermediate temperatures have been measured at the inlet and outlet locations. To further complicate the situation, it is unclear whether a temperature probe inserted into the flow stream will measure the static temperature, total temperature or some intermediate value. Eckert and Drake [31] have introduced the concept of a recovery temperature to model the true temperature measured by a temperature probe:

$$T_r = T_s + r\frac{V^2}{2c_p} \tag{4.2}$$

where r is a recovery factor in the range $0 \leq r \leq 1$. In fast moving flows, the boundary layer around the temperature probe may be thin, and the probe might measure a quantity closer

to the static temperature, but the same cannot be said for slower flows and thicker boundary layers. Though a thorough discussion of measurement techniques and local fluid dynamics is beyond the scope of this work, it suffices to say the recovery factor r must be determined experimentally for the range of expected operating conditions.

The total temperature separation at the cold and hot exits are given by

$$T_{s,c} = T_{in} - T_{cold} \tag{4.3}$$

$$T_{s,h} = T_{hot} - T_{in} \tag{4.4}$$

In this work, we aim to evaluate the influence of BCs when modelling the RHVT using CFD software. In section 4.2 we detail the experimental setup and procedure, specifically designed to enable accurate comparisons with CFD results. Section 4.3 describes the general features common to all CFD models used in this work, and section 4.4 contains a grid independence study to ensure our results are accurate solutions to the governing equations. In the subsequent sections we investigate the accuracy of CFD results in three studies:

1. *Evaluate the impact of BC locations and type.* Three different VT domains have been used in the CFD model: one domain has boundaries at the exits of the vortex tube (similar to the boundary locations in previous numerical studies), a second domain includes the outlet plenums in the experiment (such that the boundary locations are at the same position as the measurement stations in the experiments), and a third domain includes both the outlet plenums and the inlet shroud. By comparing the CFD results from these domains, we evaluate the error associated with truncating the domain at the vortex tube exit locations. We will further assess the relative impact of using different combinations of mass flow and pressure BCs.

2. *Evaluate the impact of the different turbulence models.* Several studies have reviewed the impact of various turbulence models on the energy separation within the RHVT, often concluding that one model is superior because the predicted temperature separations are closest to the experimentally measured results. Here we perform a similar study using the k-ε, k-ω, k-ω Shear Stress Transport (k-ω SST), and Scale-Adaptive Simulation

Shear Stress Transport (SAS SST) turbulence models, specifically analyzing how these turbulence models affect the flow structure in the RHVT and the local variations in energy transfer across the stagnation streamline.

3. *Evaluate the impact of the axisymetric assumption.* In many studies an axisymetric model of the VT has been employed to simplify the domain, and reduce the computational cost of the simulations. In these cases, the nozzle ring (or vortex generator) must be replaced by a prescribed injection angle to generate the vortex, and the angle of this injection is often roughly computed based on the angle of the inlet channels. We will show the impact of two different choices for the injection angle, and compare to 3D simulations and experimental data. We will also show the influence of of the nozzles on the local energy separation by comparing the 2D axisymmetric results with results obtained from a 3D axisymmetric domain with axisymmetric BCs and a similar domain with the inlet nozzles modelled.

In each of these studies, we have chosen to replicate a specific set of experimental data collected by Parker and Straatman [32] wherein the upstream inlet gauge pressure was regulated to 275.79 kPa. This data set was chosen because it was replicated twice experimentally; once using the setup using an aluminum VT, and a second time using a Delrin VT. In all cases the results were virtually the same.

To ensure the results are reproducible, we have granted access to digital files containing the 3D models from which the physical vortex tube was fabricated, the computational grids used, the scripting files used to generate the grids, and the simulation setup files.

4.2 Experimental Apparatus

The computational models studied in this paper are based on the VT designed and fabricated for experiments by Parker and Straatman [32]. Fig. 4.2 shows a detailed illustration of the vortex tube, including the inlet shroud and outlet plenums. Sensor blocks were installed upstream of the inlet shroud and downstream of each outlet plenum where the static pressure and recovery temperature was measured. Fig. 4.3 shows the position of the temperature and pres-

sure measurements taken in the sensor blocks in relation to the vortex tube. Table 4.1 provides the values for geometric parameters. The total mass flow was measured upstream of the inlet sensor block using a laminar mass flow meter, while the outlet mass flow rates were measured using rotameters, installed downstream of the sensor blocks. Hence, the temperature, pressure and mass flow rates were known upstream of the VT entrance, and just downstream of both the hot and cold exits. The temperature and static pressure were also measured inside of the outlet plenums. The purpose of the plenums is this: while the flow properties at the 'immediate exits' (c.f. the VT exits in Fig. 4.1) of the VT may vary significantly over their cross-sections due to the strong swirl velocity, the flow properties at the downstream sensor blocks are nearly uniform over the pipe radius, such that the measured properties can be reasonably assumed to be the bulk properties of the flow. In each sensor block, the pressure sensor was inserted into a recessed hole, such that the sensor did not protrude into the tube, while the hemi-spherical head (radius 2 mm) of the temperature probe protruded into the 5 mm diameter tube by approximately 1.5 mm. The probe was seated in a hole drilled into Delrin sensor blocks resulting in the leads being insulated from the metal pipes. Parker and Straatman [32] have estimated the recovery factor of these sensors, and all reported temperatures have been adjusted using these factors.

Each of the experimental runs were carried out by holding the pressure at the inlet and the cold outlet constant and varying the hot outlet pressure to change the cold mass fraction. By controlling the cold mass fraction in this manner, the plug located at the hot outlet does not move, resulting in a constant geometry. The recovery temperature, static pressure, and mass flow rates were measured at the three sensor blocks for the case with an inlet pressure of 353 kPa. To eliminate any transient effects in the temperature measurements, the measurements were recorded 10 minutes after the vortex tube ac hived steady state at each mass flow fraction. The vortex tube, inlet pipe and vortex generator were machined from aluminum, where as the outlet pipes were machined from stainless steel and the remainder of the vortex tube setup was machined from Delrin.

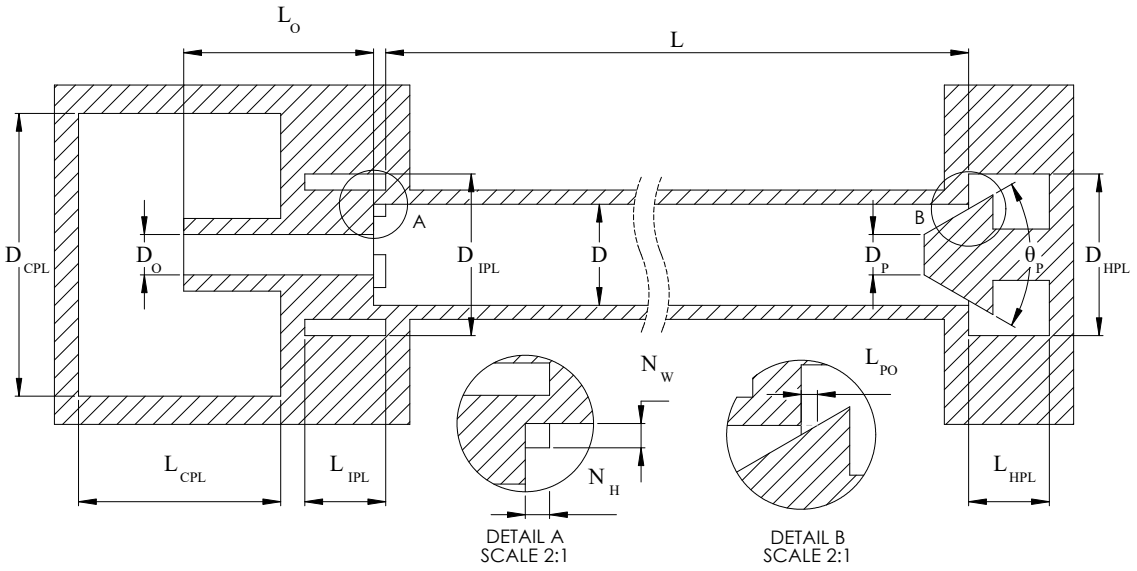

Figure 4.2: Sectioned drawing of the Ranque-Hilsch vortex tube used in this research, showing the relevant dimensions (given in table 4.1), including the hot and cold plenums

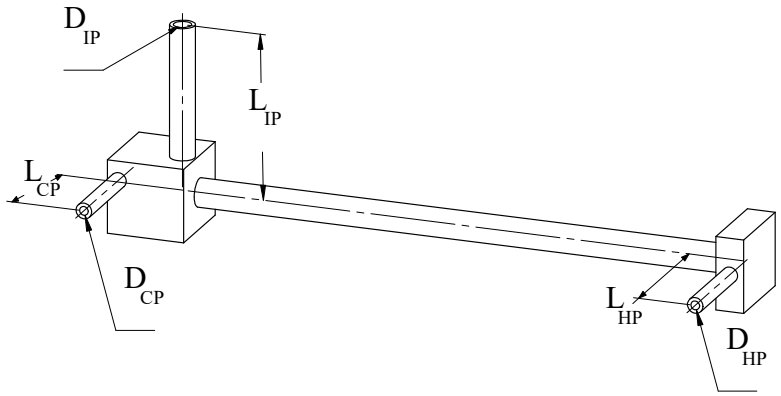

Figure 4.3: Perspective drawing of the Ranque-Hilsch vortex tube used in this research; the visible tube ends correspond to the sensor block and measurement locations, and dimensions are given in table 4.1

L	313.06 [mm]
D	12.52 [mm]
Aspect Ratio	25
N_W	1.50 [mm]
N_H	1.50 [mm]
Number of Nozzles	4
D_O	5.00 [mm]
L_O	22.00 [mm]
D_P	5.00 [mm]
θ_P	60 [°]
L_{PO}	2.00 [mm]
D_{IPL}	19.45 [mm]
L_{IPL}	8.50 [mm]
D_{CPL}	35.00 [mm]
L_{CPL}	25.00 [mm]
D_{HPL}	19.45 [mm]
L_{HPL}	8.18 [mm]
D_{IP}	9.92 [mm]
L_{IP}	96.65 [mm]
D_{CP}	5.00 [mm]
L_{CP}	76.70 [mm]
D_{HP}	5.00 [mm]
L_{HP}	76.70 [mm]

Table 4.1: Relevant geometric properties of the Ranque-Hilsch vortex tube used in this research, as defined in Figs. 4.2 and 4.3

4.3 CFD Model setup

In the following sections, several different CFD models are described and evaluated; their common features are recorded here for conciseness. In all cases, air is used as the working fluid, which is modelled using the ideal gas equation of state with constant heat capacities. The vortex generated within the tube creates a strong radial pressure gradient, and the ideal gas model is required to model the highly compressible flow, and predict temperature separation. The relevant properties are dynamic viscosity $\mu = 1.831 \times 10^{-5}\,\mathrm{kg\,m^{-1}\,s^{-1}}$, thermal conductivity $k = 2.61 \times 10^{-2}\,\mathrm{W\,m^{-1}\,K^{-1}}$ and heat capacity $c_p = 1004.4\,\mathrm{J\,kg^{-1}\,K^{-1}}$. ANSYS® CFX, Releases 19.0, 19.1, and 19.2 were used to solve the governing equations of mass, momentum, and energy, which are provided in the CFX Solver Theory Guide [33]. Importantly, the viscous dissipation term has been switched on for all simulations reported in this study. The SAS SST turbulence model was selected for this problem, as it behaves like the classical two-equation models (such as the k-ε or k-ω models) in regions where the flow is steady, but has the capability to capture large-scale turbulent structures like Large Eddy Simulations, while adopting Reynolds-Averaged Navier-Stokes (RANS) formulation in regions of steady flow [34]. High resolution advection schemes were used for all transport variables, and the second order backward Euler time-stepping scheme was used.

At the inlet, the total temperature was set based on the experimental value, and the turbulence intensity was set to 5%. The enthalpy and turbulent transport quantities at the outlets are obtained implicitly from the solution. No-slip and adiabatic conditions were applied to all solid boundaries, including the VT walls, and the plenum interior surfaces. Automatic (enhanced) wall treatments [33] were used to capture the influence of turbulent boundary layers.

The computational grids were generated using two softwares: the blockMesh tool available from the OpenFOAM library [35] was used to produce the structured grid throughout the VT and exit plenums, while the ANSYS Meshing tool® [36] was used to produce a hexahedral-dominant mesh for the inlet tube and shroud.

Ranque-Hilsch flow contains a strong vortex with relatively high angular velocities, which naturally extend through the immediate exits into the downstream geometry, until it decays or is halted by some other means. This strong vortex naturally forms a significant radial pressure

gradient, which might not be accurately characterized by the constant pressure or mass flow BCs that are imposed at the boundaries of many CFD studies of the RHVT. Therefore, in cases where the downstream geometry has been truncated to the exits (shown in model A of Fig. 4.5), a radial equilibrium BC has been applied [33] to allow a more natural variation of the boundary pressure profile in the presence of strong swirl.

4.4 Grid Independence

A grid independence study was conducted to verify that the present results are accurate solutions to the governing equations of mass, momentum, and energy. Model B (shown in Fig. 4.5) was selected for the grid convergence study. As it will be seen, the M-P-M BC configuration produces the best agreement with experimental results, and has therefore been used in this study. The experimental trial we have selected to simulate has an inlet mass flow rate $\dot{m}_{\mathrm{i}} = 6.076\,\mathrm{g\,s^{-1}}$, an inlet total temperature $T_{\mathrm{i,total}} = 297\,\mathrm{K}$, an absolute cold exit static pressure is $P_{\mathrm{c}} = 101\,\mathrm{kPa}$ and a hot exit mass flow rate is $\dot{m}_{\mathrm{h}} = 2.51\,\mathrm{g\,s^{-1}}$.

To determine grid independence, four grids were generated, and a time-step size of 1.6×10^{-5} s was selected for the simulations. Starting from the coarsest grid, finer grids were generated by multiplying the number of nodes along each edge by a global factor without adjusting the mesh controls such that the mesh structure is maintained. In each case convergence was achieved when the root-mean-square residuals for mass, momentum, energy and turbulence equations remained under 5×10^{-6} while the mean values of the quantities of interest did not change within 1% for a period of 1000 or more time-steps. Values reported in the remainder of this work have been time-averaged over at least 0.016 s to average out the small step-to-step variations such that an accurate comparison can be made with the experimental data. As seen in table 4.2, grid-independence was achieved when at least 523054 grid cells were used. Mesh 3 (shown in Fig. 4.4, containing 1434680 elements) has been chosen to represent model A for the remainder of this work.

Mesh Label	Cell Count	T_c [K]	T_h [K]
Experiment	-	284.6	312.9
Mesh 1	295842	286.5	312.3
Mesh 2	523054	286.5	312.0
Mesh 3	1434680	285.9	313.0
Mesh 4	2735832	286	313.3

Table 4.2: Grid convergence of CFD calculations of the Ranque-Hilsch vortex tube with a cold mass fraction of 0.5869 based on total temperatures measured and computed at the hot and cold exits.

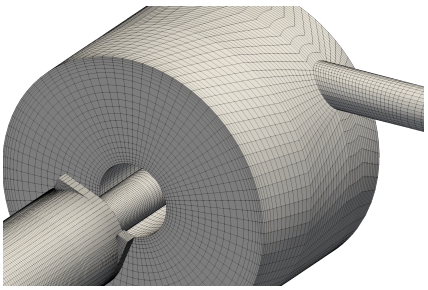

(a) Inlet mesh detail

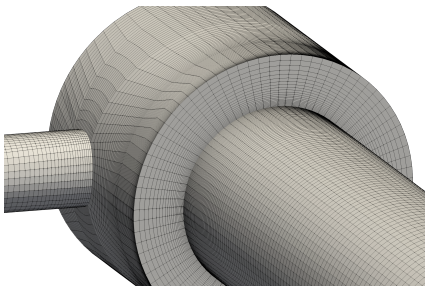

(b) Hot exit detail

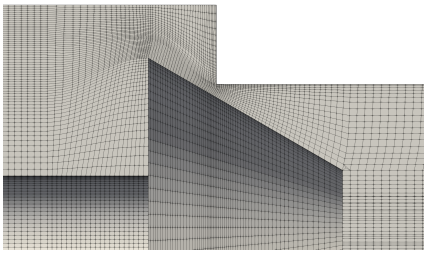

(c) Cut-away view of the mesh along the $\theta = 0$ plane, around the hot plug

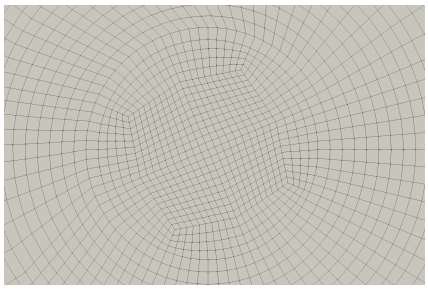

(d) Close-up of the o-grid structure containing the tube axis at the cold plenum

Figure 4.4: Selected views of the computational mesh used in CFD calculations of the RHVT, containing 1434680 cells

4.5 Energy Transfer Analysis

Previous researchers have used the solution fields from CFD studies to evaluate the energy transfer from the cold stream to the hot stream using the following technique. In a time-averaged CFD solution a streamsurface separates the hot and cold fluid streams, which we call the stagnation streamsurface. Similarly, axisymetric CFD calculations contain a stagnation streamline separating the hot and cold streams. Logically, the energy transferred across the stagnation streamsurface is equal to the energy gained or lost by the hot and cold fluid streams, respectively. Aljuwayhel et al. [9] were the first to compute the energy transfer due to heat

conduction, circumferential shear work, and axial shear work using the formulas

$$\frac{\partial \dot{Q}}{\partial s} = -2\pi k_{\text{eff}} r \frac{\partial T}{\partial n} \tag{4.5}$$

$$\frac{\partial \dot{W}_\theta}{\partial s} = -2\pi \mu_{\text{eff}} r v_\theta r \frac{\partial}{\partial n}\left(\frac{v_\theta}{r}\right) \tag{4.6}$$

$$\frac{\partial \dot{W}_z}{\partial s} = -2\pi \mu_{\text{eff}} v_z r \frac{\partial v_z}{\partial n} \tag{4.7}$$

where s is a streamline co-ordinate, n is the normal vector pointing towards the hot stream, $\mu_{\text{eff}} = \mu_{\text{eddy}} + \mu$ is the effective viscosity, $k_{\text{eff}} = c_p \mu_{\text{eddy}} / Pr_{\text{t}} + k$ is the effective thermal conductivity, and $Pr_{\text{t}} = 0.9$ is the turbulent Prandtl number.

In the CFD results analyzed in this work, the stagnation streamsurface always intersects the hot exit cone, and we identify streamlines on this surface using the following technique. First a line is drawn on a given θ-plane from the leading edge of the hot exit cone to the rear of the hot exit cone (where the working section of the vortex tube meets the hot plenum). Post-processing software is then used to identify the point of minimum absolute axial velocity on this line. A stagnation streamline is traced backward to the inlet from this point. A discrete representation of the stagnation streamline can then be written to file, alongside all the relevant quantities and gradients required to compute the energy transfers. The data file may be post-processed using Python to compute equations 4.5 - 4.7 and their integrals to find the local and total energy transfers across the stagnation streamline, respectively. Unfortunately, a complete representation of the streamsurface cannot be obtained; only single streamlines can be traced, which leaves the normal vectors along the 3D streamline undefined. We remedy the problem by assuming that the stagnation streamsurface is axisymmetric, and therefore the normal vectors contain no component in the circumferential direction, which closes the problem.

4.6 Impact of CFD Model Boundary Types and Boundary Locations

The RHVT has a single inlet (upstream of the vortex generator) and two distinct outlets; while the total mass flow rate through the outlets must balance with the inlet, the cold mass fraction

is dictated by the fluid dynamics within the tube. When modelling the RHVT using CFD, the mass flow rate and pressures cannot be enforced simultaneously at the inlet or outlets, therefore the analyst must choose whether to apply a pressure BC or a mass flow BC at each of the boundaries.

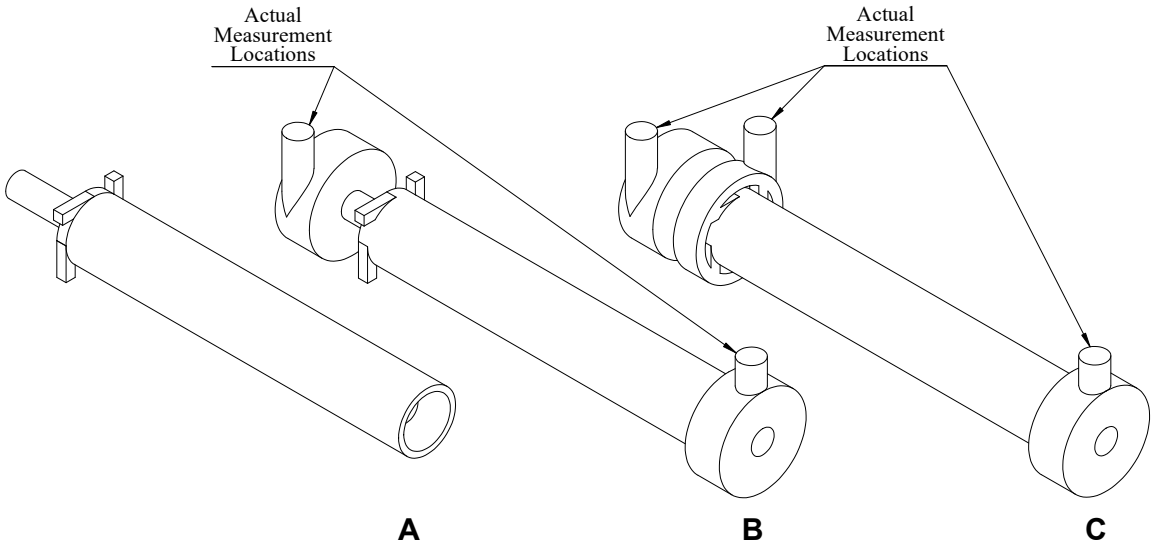

Figure 4.5: Diagrams showing the different CFD domain extents of models A, B, and C of the Ranque-Hilsch vortex tube. Note that these diagrams are for illustrative purposes only, and their geometric proportions do not correspond to their true dimensions shown in figures 4.2 and 4.3

Three different RHVT models were studied in the present work, as shown in Fig. 4.5. Model A represents a typical 3D domain of the RHVT, with four tangential inlets, and the exit boundaries located at the entrance to the hot and cold plenums. Model B is similar, but the outlet plenums are included in the CFD domain. Importantly, the exit boundaries of model B and C correspond exactly to the location of the sensor blocks in the experiment. Model C includes both plenums and the inlet shroud. As it will be seen, models B and C predict nearly the same values at the VT exits when the inlet mass flow is considered, but only model C allows for an accurate prediction of the inlet pressure.

Here, we remind the reader of our notation to concisely refer to each BC combination; the template ⟨inlet BC⟩-⟨cold outlet BC⟩-⟨hot outlet BC⟩ describes the BCs used in a RHVT

simulation. We use P to denote a pressure BC, and M to denote a mass flow BC. For example the M-P-M configuration indicates the inlet mass flow, cold exit pressure, and hot exit mass flow have been fixed.

In this study we investigate the differences between the M-P-M, M-M-P, M-P-P, and P-P-P BC configurations on models A, B, and C in Fig. 4.5. Ideally, each of these BC combinations should yield the same solution field, but in practice the influence of model inaccuracies (discussed below), cause uncontrolled quantities to drift from their experimental values. For example, in the M-M-P configuration, the cold exit pressure is uncontrolled, and, as it will be seen, does not match the experimental value at the end of a grid and time-step independence calculation. In each case the SAS SST turbulence model has been used.

In many experiments the outlet quantities of the VT are measured at locations downstream of the outlets. Yet many CFD studies based on these experiments used models similar to model A, and have applied pressure or mass flow BCs from the experiment to those locations. In doing this, they have neglected the influence of the downstream flow passage on the results. Here we aim to test that assumption by comparing models A, B, and C. In model A, pressure BCs have been applied using the radial equilibrium BC [33], such that the predicted pressure profile along the boundary is better suited to a swirling flow at the exit. We will specifically highlight the difference between applying pressure BCs measured in the sensor blocks in model A1, and a more realistic approximation of the pressure BCs in model A2, where the hot exit pressure is assumed to be equal to the pressure recorded at the plenum wall, and the cold exit pressure is computed as $p_{\mathrm{c\,A2}} = p_{\mathrm{c\,pl\,exp}} - (p_{\mathrm{c\,pl\,CFD\,B}} - p_{\mathrm{c\,tube\,CFD\,B}})$, where $p_{\mathrm{c\,pl}}$ is the static pressure measured inside the plenum, and $p_{\mathrm{c\,tube\,CFD\,B}}$ is the pressure observed at the cold exit boundary location of model A2 inside model B. In models B and C, uniform static pressure BCs have been applied at the outlets.

We have not investigated P-M-P or P-P-M configurations, as it makes little sense to control the mass flow at one of the outlet boundaries while the total mass flow rate would be unconstrained. The P-M-M configuration is unstable in CFX, and it has not been used in a CFD model of the RHVT to our knowledge, so we have not tested it here.

4.6.1 Discussion of Model Influences

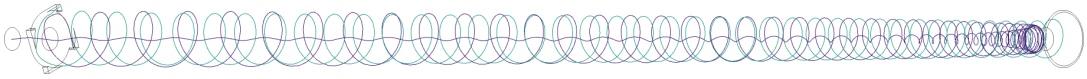

Figure 4.6: 3D helical streamlines passing through the RHVT; lighter streamline proceeds to the hot exit, and the darker streamline proceeds to the cold exit

Fig. 4.6 is a representative flow field within the RHVT, showing the common reverse flow structure; air entering the tube swirls about the tube axis while moving along its axis, eventually leaving the annular hot exit or retreating to the cold exit.

In all simulations reported in this work, the flow recirculation region crossing the cold exit boundary seen in refs. [11, 12, 14] have not been observed. We attribute this to the accuracy of the radial equilibrium BC; the aforementioned studies applied unrealistic uniform static pressure boundary conditions.

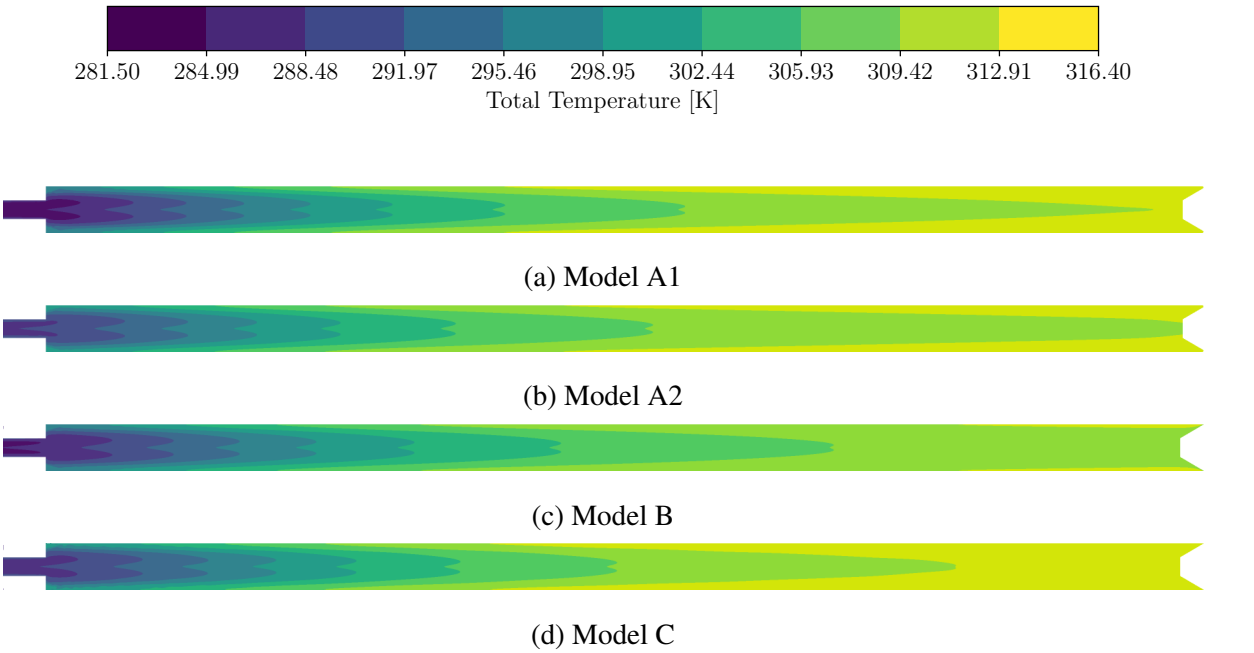

(a) Model A1

(b) Model A2

(c) Model B

(d) Model C

Figure 4.7: Total temperature contours of the working section of the Ranque-Hilsch vortex tube for a cold mass fraction of 0.5869 and different model approximations

Fig. 4.7 shows temperature contour plots for models A1, A2, B, and C. The similarity between these plots shows the temperature distribution inside the vortex tube is largely similar.

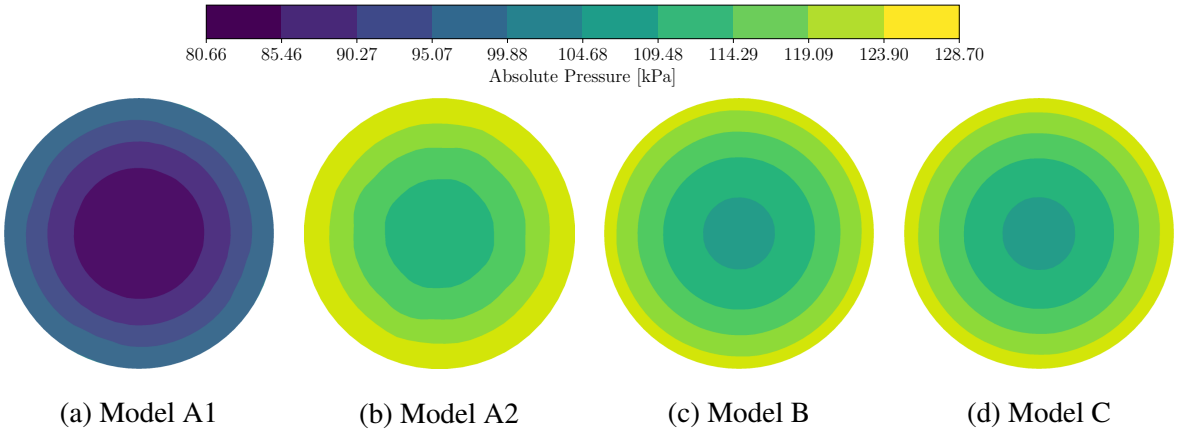

(a) Model A1 (b) Model A2 (c) Model B (d) Model C

Figure 4.8: Cold exit tube absolute pressure contours in the Ranque-Hilsch vortex tube reported where the cold exit pressure has been specified, located at the cold exit of model A, and the corresponding locations within models B and C

The pressure contours shown in Fig. 4.8 show that there is a significant difference between model A1 and the other models, since the pressure of the downstream sensor block has been applied at the VT cold exit. Furthermore, the strong radial pressure gradients in models B and C confirm that a uniform static BC applied at the cold exit is not adequate.

Table 4.3: Influence of BC configurations for model A1. Greyed cells are fixed to experimental boundary values.

	Inlet		Cold Outlet			Hot Outlet	
Configuration	$\dot{m}_i$ [g s^{-1}]	p_i [kPa]	λ	p_c [kPa]	T_c [K]	p_h [kPa]	T_h [K]
Experiment	6.076	355.4	0.5869	100.7	284.6	177.2	312.9
M-P-M	6.076	311.7	0.5869	100.7	286.6	137.9	317.0
M-M-P	6.076	329.3	0.5869	139.2	289.8	177.2	312.5
M-P-P	6.076	328.8	0.3314	100.7	296.9	177.2	331.5
P-P-P	7.194	355.4	0.3467	100.7	278.2	177.2	310.3

Table 4.4: Influence of BC configurations on Model A2. Greyed cells are fixed to boundary values.

	Inlet		Cold Outlet			Hot Outlet	
Configuration	$\dot{m}_i$ [g s^{-1}]	p_i [kPa]	λ	p_c [kPa]	T_c [K]	p_h [kPa]	T_h [K]
Experiment	6.076	355.4	0.5869	129.3	284.6	188.3	312.9
M-P-M	6.076	321.7	0.5869	129.3	288.1	161.6	315.0
M-M-P	6.076	334.9	0.5869	151.8	290.5	188.3	311.5
M-P-P	6.076	334.4	0.9024	129.3	296.2	188.3	326.9
P-P-P	9.000	355.4	0.5800	129.3	285.0	188.3	318.8

Table 4.5: Influence of BC configurations for model B. Greyed cells are fixed to experimental boundary values.

	Inlet		Cold Outlet			Hot Outlet	
Configuration	$\dot{m}_i$ [g s^{-1}]	p_i [kPa]	λ	p_c [kPa]	T_c [K]	p_h [kPa]	T_h [K]
Experiment	6.076	355.4	0.5869	100.7	284.6	177.2	312.9
M-P-M	6.076	324.6	0.5869	100.7	287.9	149.2	315.0
M-M-P	6.076	337.4	0.5869	136.8	290.2	177.2	313.0
M-P-P	6.076	334.8	0.7298	100.7	292.0	177.2	319.7
P-P-P	6.643	355.4	0.6747	100.7	290.0	177.2	318.4

	Inlet		Cold Outlet			Hot Outlet	
Configuration	$\dot{m}_i$ [g s^{-1}]	p_i [kPa]	λ	p_c [kPa]	T_c [K]	p_h [kPa]	T_h [K]
Experiment	6.076	355.4	0.5869	100.7	284.6	177.2	312.9
M-P-M	6.076	393.7	0.5869	100.7	287.8	150.2	316.4
M-M-P	6.076	403.0	0.5869	134.8	290.1	177.2	312.2
M-P-P	6.076	401.0	0.7224	100.7	291.4	177.2	318.8
P-P-P	5.464	355.4	0.7976	100.7	293.9	177.2	319.9

Table 4.6: Influence of BC configurations for model C. Greyed cells are fixed to experimental boundary values.

The simulation results for models A1, A2, B, and C are given in tables 4.3, 4.4, 4.5, and 4.6 respectively. For the M-P-M and M-M-P BC configurations, similar outlet temperatures have been predicted for models A1, A2, B, and C, while the inlet pressure in model C is elevated due to the pressure drop through the shroud. When comparing the M-P-M to M-M-P results, small variations in the inlet pressure can be observed.

While temperature separation is reasonably predicted by all BC configurations, the M-P-P and P-P-P BC configurations fail to predict the correct mass flow split, even while the appropriate outlet pressures have been fixed. Furthermore, we observe that the M-P-M and M-M-P cases differ because when the pressure is enforced at one exit, it remains unconstrained at the opposite exit and inlet.

Overall, it is clear that the presence of the inlet shroud (contrasting models B and C) only impacts the predictions of the upstream pressure, validating the implicit assumption from previous papers that four uniform property inlets is a sufficient inlet condition for modelling the RHVT.

4.6.2 Sources of Discrepancy

The results in tables 4.3, 4.4, 4.5, and 4.6 give important insight into the use of CFD to model Ranque-Hilsch flow. Clearly, no combination of BC configuration and domain model is capable of predicting all measured experimental quantities. Since geometric and grid resolution

errors are minimal, the only possible sources of error are are material property approximations, modeling simplifications, inaccurate BCs, or experimental uncertainties.

In our CFD study we have assumed a perfect gas model, with constant viscosity and thermal conductivity. Dutta et al. [37] has challenged this assumption, by comparing the results of a NIST real gas model with the ideal gas model, showing that the real gas model for air offers only a slight improvement over the ideal gas model at temperatures near atmospheric temperature, wherein constant specific heats were used. Liu et al. [38] have assumed a variable heat capacity as a polynomial function of temperature, and found good agreement with experimental data, although no comparison was made to an equivalent simulation without variable heat capacity. Ouadha et al. [20] have studied numerically the effects of comparing a simulation using constant thermophysical properties to properties modelled as a polynomial function of temperature. They found that both constant and variable properties are capable of predicting the bulk temperature separation, but the internal flow field is significantly different between the two cases.

Some modelling approximations are also present; chief among which is turbulence model. The RHVT has been simulated using a variety of turbulence models, and several papers have compared their relative accuracy. Dutta et al. [39] used an axisymetric CFD model to evaluate several RANS models, and conclude that the k-ε model is the most accurate, despite its' simplicity. Baghdad et al. [19] used a 1/4 VT model to compare several RANS two-equation models and the Reynolds Stress Model (RSM). All of the models over-predicted temperature separation, but the RSM model yielded the most accurate predictions. Meanwhile, Liu and Liu [38] have used a 3D VT model, comparing several two-equation models with the RSM, and concluded that the RSM model is the most accurate. Niknam et al. [40] also used a 3D VT model to compare the relative performance of several two-equation turbulence models, against the Spalart and Allmaras model and a three-equation model developed by Walters and Cokljat [41] using a root-mean-square error approach. The three-equation model was the most accurate, yielding the lowest root-mean-square error of any of the models. Niknam et al. attributes the increased accuracy of the three equation model to its ability to capture viscous heating inside the VT. In contrast to previous authors, the k-ε model was the least accurate overall. Chýlek et al. [42] also compared several RANS models against the RSM model using a 3D

domain. They also found that the standard k-ε model yielded the most accurate results. The literature offers no consensus on which models are best suited to model the RHVT, and there is little discussion as to why some models outperform others. We explore the influences of different turbulence models in section 4.7.

Additionally, we have assumed that Stokes' hypothesis is valid. This has been assumed in all computational studies we are aware of, however it's omission is suspect; both Cramer [43] and Emmanuel [44] agree that the bulk viscosity becomes relevant when acoustic effects are present within the flow. At the same time Kurosaka [45] found a strong link between the strength of an acoustic signal and the magnitude of temperature separation, indicating that CFD simulations should consider acoustic effects and the significance of the bulk viscosity.

While several CFD studies including Bianco et al. [46], Zhang et al. [22], and Farouk and Farouk [47] have observed large-scale unsteady flow structures in the RHVT, the solution fields in this report were always observed to be steady, which suggests that acoustic effects do not drive temperature separation, if they participate at all.

4.7 Turbulence Modelling

In this section, we focus on comparing the impact of four different turbulence models on the local and total energy separation inside the RHVT: k-ε, k-ω, k-ω SST, and SAS SST. The full details of these models including transport equations and model coefficients are given in the CFX theory guide [33]. Here we analyze the circumferential velocity, axial velocity, static temperature, and turbulent eddy viscosity solution fields of CFD simulations of model B, the M-P-M BC configuration, and using the experimental input data with a cold mass fraction of 0.5869. For this study we used a mesh containing 3026688 elements to produce results capable of resolving the local energy transfers near the inlet of the VT.

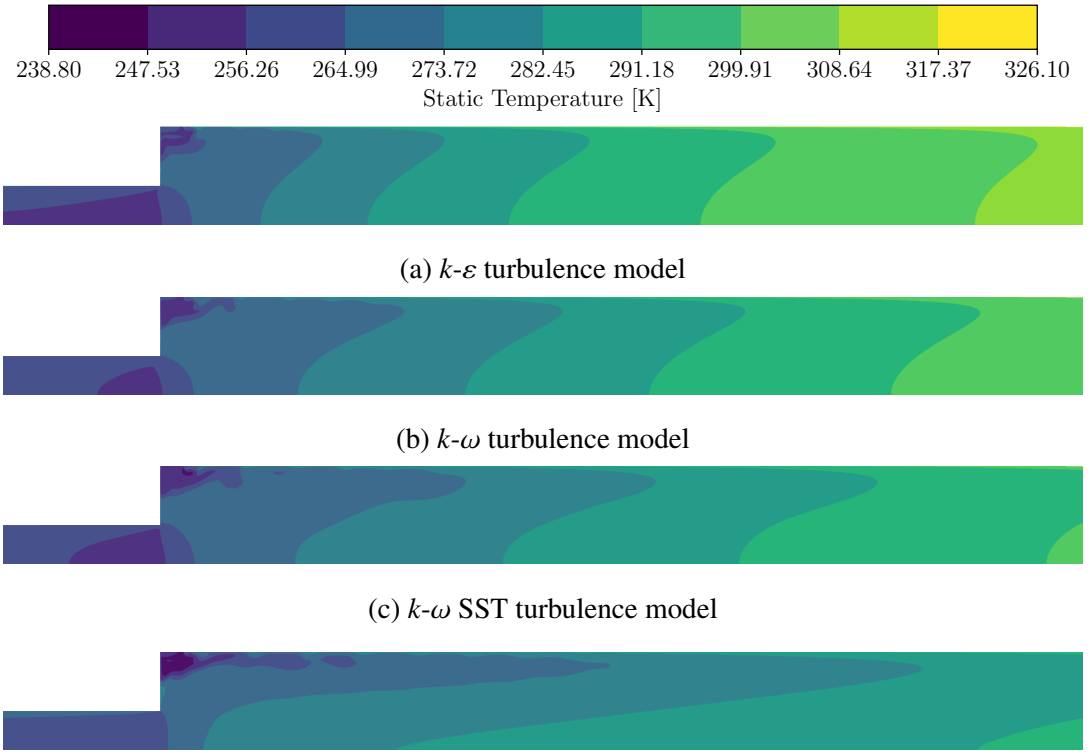

(a) k-ε turbulence model

(b) k-ω turbulence model

(c) k-ω SST turbulence model

(d) SAS SST turbulence model

Figure 4.9: Static temperature profile comparisons for different turbulence models used to simulate the Ranque-Hilsch vortex tube for a cold mass fraction of 0.5869

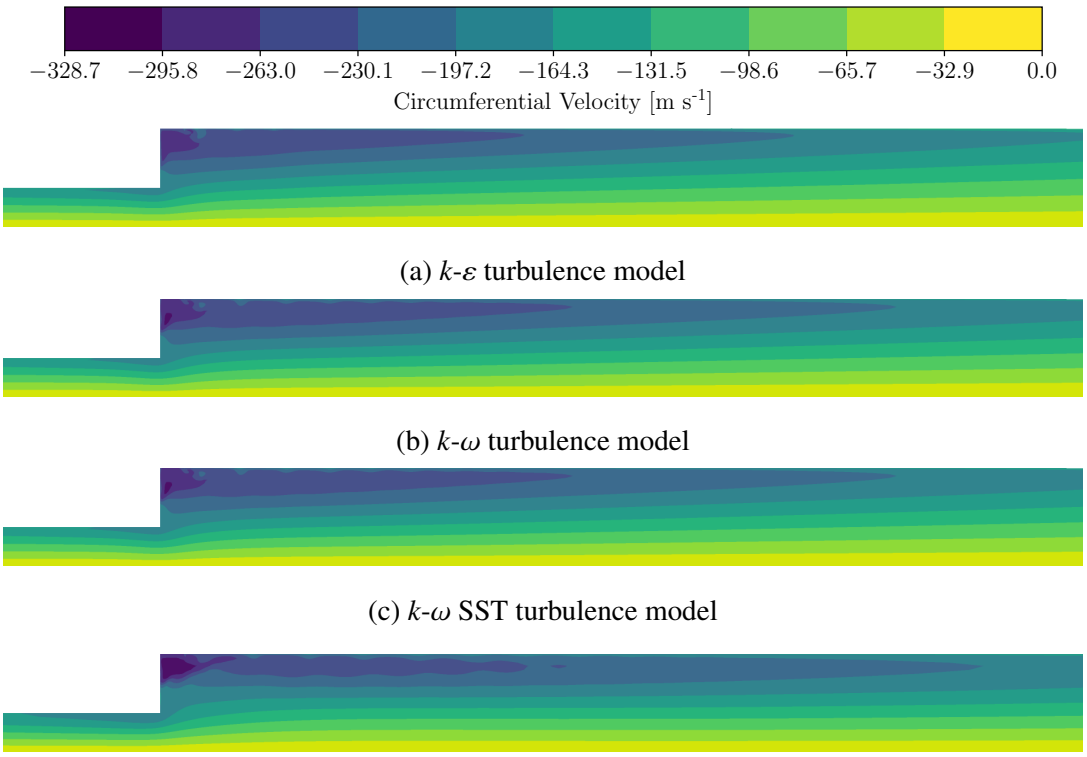

(a) k-ε turbulence model

(b) k-ω turbulence model

(c) k-ω SST turbulence model

(d) SAS SST turbulence model

Figure 4.10: Circumferential velocity profile comparisons for different turbulence models used to simulate the Ranque-Hilsch vortex tube for a cold mass fraction of 0.5869

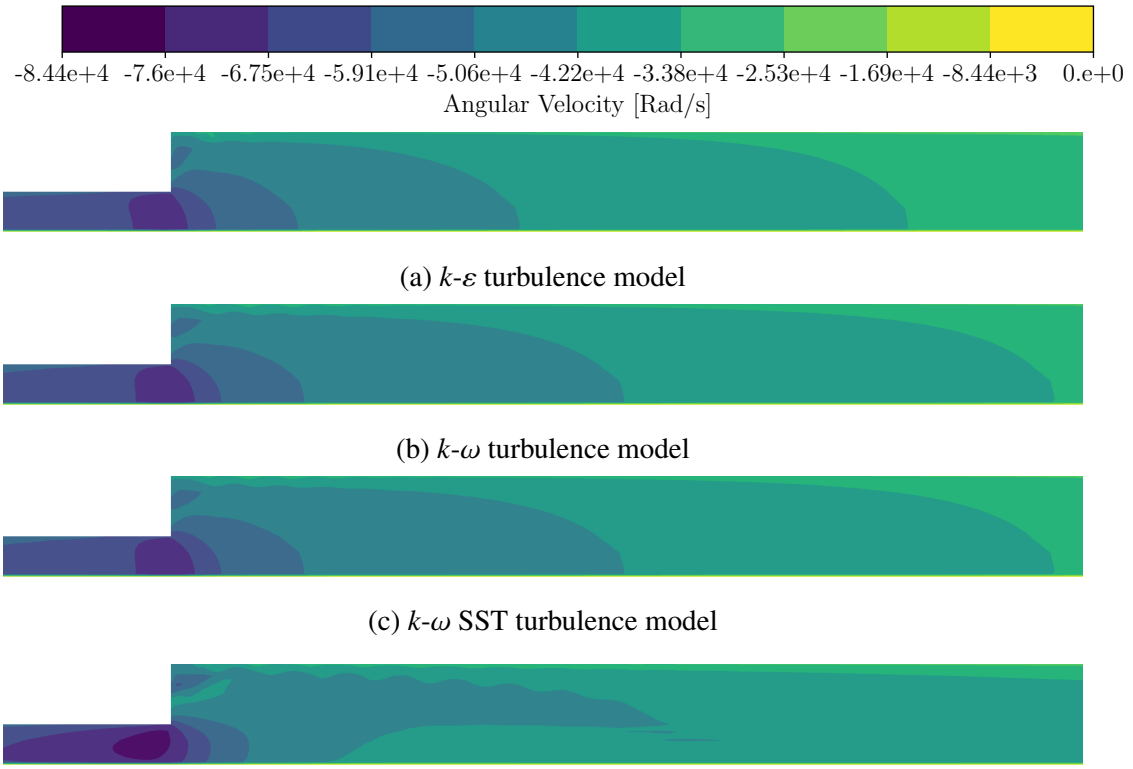

(a) k-ε turbulence model

(b) k-ω turbulence model

(c) k-ω SST turbulence model

(d) SAS SST turbulence model

Figure 4.11: Angular velocity profile comparisons for different turbulence models used to simulate the Ranque-Hilsch vortex tube for a cold mass fraction of 0.5869

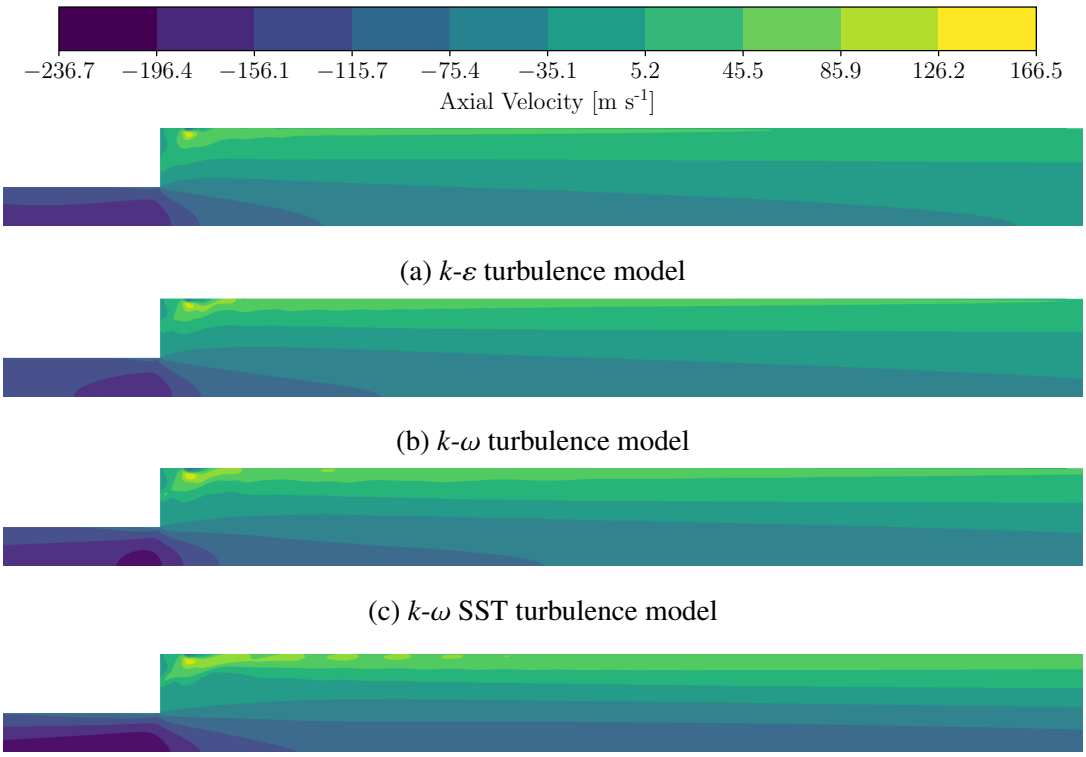

(a) k-ε turbulence model

(b) k-ω turbulence model

(c) k-ω SST turbulence model

(d) SAS SST turbulence model

Figure 4.12: Axial velocity profile comparisons for different turbulence models used to simulate the Ranque-Hilsch vortex tube for a cold mass fraction of 0.5869

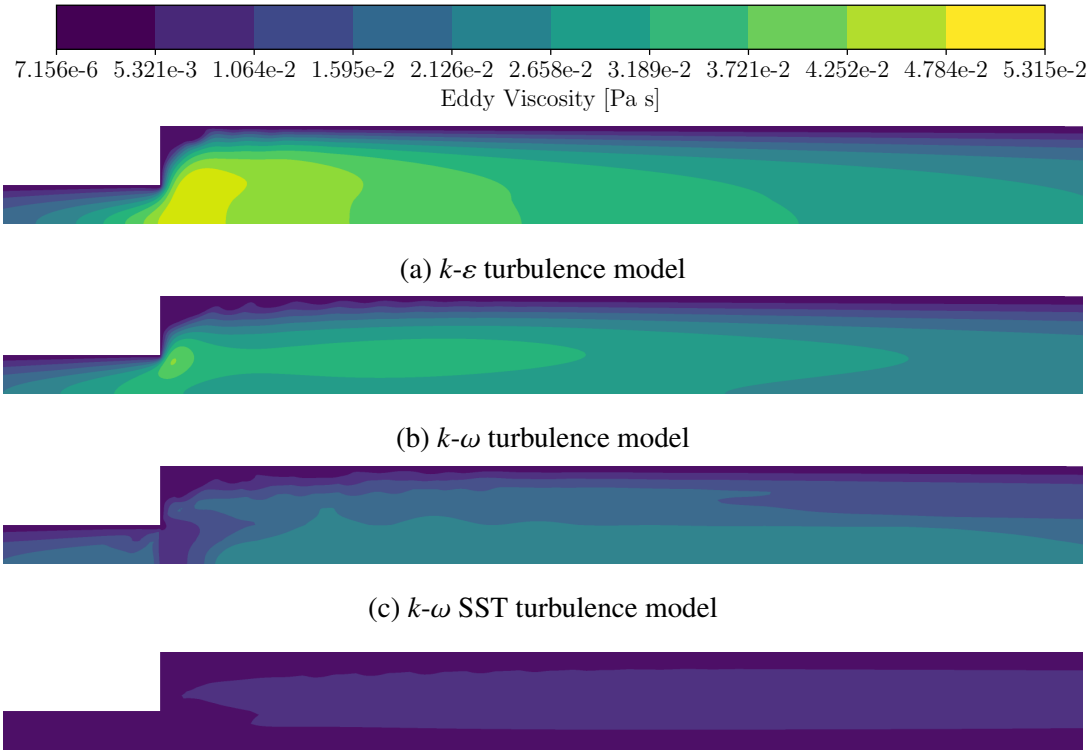

(a) k-ε turbulence model

(b) k-ω turbulence model

(c) k-ω SST turbulence model

(d) SAS SST turbulence model

Figure 4.13: Eddy Viscosity profile comparisons for different turbulence models used to simulate the Ranque-Hilsch vortex tube for a cold mass fraction of 0.5869

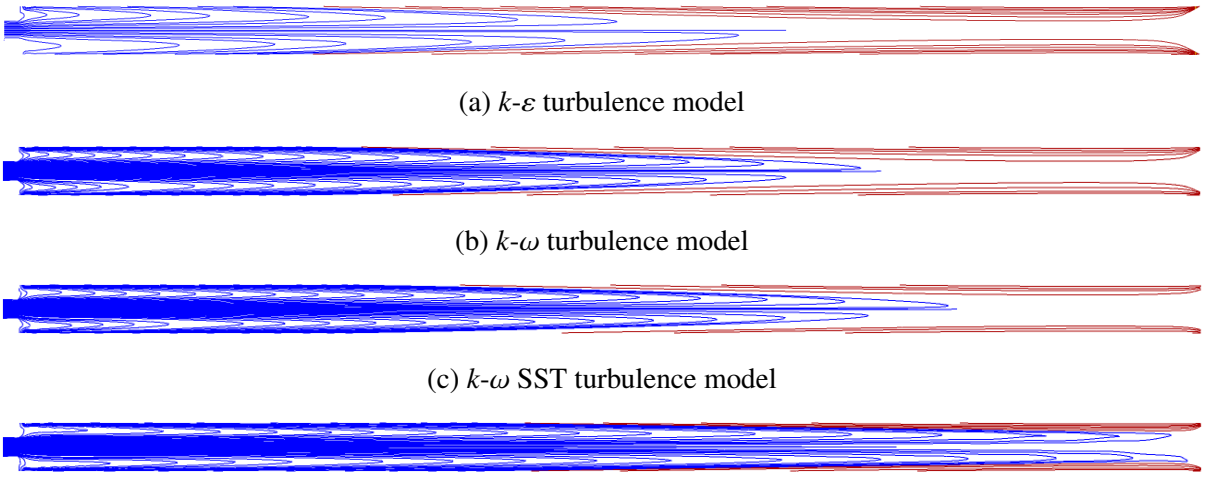

(a) k-ε turbulence model

(b) k-ω turbulence model

(c) k-ω SST turbulence model

(d) SAS SST turbulence model

Figure 4.14: Streamline comparisons for different turbulence models used to simulate the Ranque-Hilsch vortex tube for a cold mass fraction of 0.5869. Blue streamlines leave the cold exit, and red streamlines leave the hot exit

Table 4.7: Hot and cold exit temperatures, and energy transfers across the stagnation streamlines, extracted from the results of 3D CFD simulations of the Ranque-Hilsch Vortex Tube using different turbulence models.

Model	T_c [K]	T_h [K]	$\dot{Q}$ [W]	$\dot{W}_\theta$ [W]	$\dot{W}_z$ [W]	$\dot{E}_{tot}$ [W]
Experiment	284.6	312.9	-	-	-	-
k-ε	276.5	316.1	-53.09	148.96	-27.03	68.84
k-ω	277.0	326.0	-49.88	146.66	-26.33	70.44
k-ω SST	279.0	322.2	-61.15	150.72	-25.35	64.22
SAS SST	285.6	313.2	-43.60	122.40	-24.84	53.96

Each of the quantities of interest are displayed in Figs. 4.9-4.13, and the streamlines are shown in Fig. 4.14. With the exception of the turbulent eddy viscosity, all other quantities of interest show minimal dependence on the turbulence model, including the flow structure. In contrast, each turbulence model produces a unique distribution of the turbulent eddy viscosity, which, together with the other quantities, substantially impacts the location of the stagnation point. A detailed discussion of the formulation of each turbulence model and it's impact on the

eddy viscosity distribution is beyond the scope of this work, but we emphasize here that the temperature separation exhibits a strong dependence on the model selected, as shown in table 4.7. The models, which are listed in descending order according to their overall temperature separation, have a negative correlations with the length of their recirculation regions shown in Fig. 4.14, and their maximum eddy viscosities seen in Fig. 4.13. These facts together suggest the presence of a mechanism which elongates the recirculation region in the presence of a lower eddy viscosities, thereby increasing the interfacial surface area between the hot and cold fluid streams, and by extension, the overall energy separation.

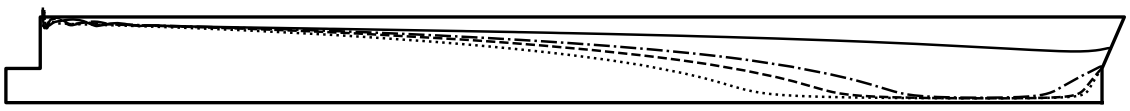

Figure 4.15: Representative 3D stagnation streamlines of the k-ε (dotted), k-ω (dashed), k-ω SST (dash-dotted), and SAS SST (solid) simulations which have been 'unwound' from the tube axis. The tube aspect ratio (L/D) has been decreased by a factor of 4 to emphasize the differences in streamline position.

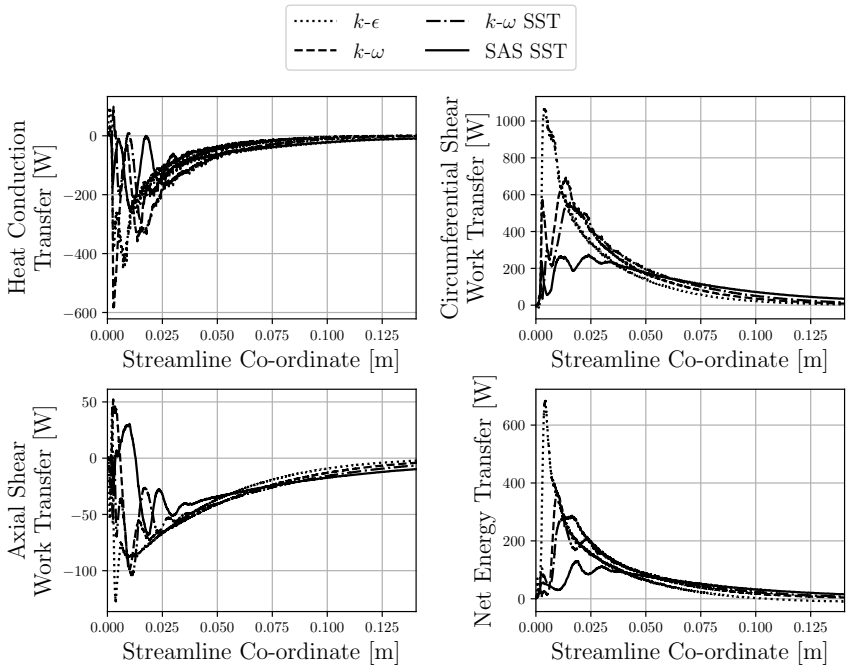

Figure 4.16: Plot of local energy transfers across the streamlines shown in figure 4.15 for the k-ε (dotted), k-ω (dashed), k-ω SST (dash-dotted), and SAS SST (solid) turbulence models. The horizontal axis on each plot has been truncated to 45% of the characteristic streamline length to emphasize the variations observed near the inlet. All energy transfers continue to decay towards the hot exit cone.

Fig. 4.15 shows the differing stagnation streamlines produced by the different turbulence models, while Fig. 4.16 shows the local energy transfers across the same streamlines. While the streamlines differ significantly towards the rear of the tube, they follow very similar trajectories near the inlet — where the greatest magnitudes in energy separation are observed. Since the velocity and temperature distributions yielded by each of the models are similar, the differences in energy transfer must be attributed to the differences in turbulent eddy viscosity. The flow near the inlet of the vortex tube is not symmetric about the tube axis due to the presence of four distinct inlet nozzles, and consequently drives the local oscillatory patterns in the energy transfer plots. Oscillations aside, the shear work transfer clearly dominates the other two modes of energy transfer in each of the models, and is mainly responsible for the energy separation. In addition, the models with the regions of higher eddy viscosity also contain greater maxima in their shear work transfer curves, suggesting more turbulent flows exhibit

higher energy separation. Note that an infinite number of stagnation streamlines exist in the stagnation streamsurface, however they all trace similar paths through the domain, and their energy transfer profiles are largely similar to the representative streamlines and their energy transfers shown in figures 4.15 and 4.16.

While these distributions are certainly interesting in their own right, their conflicting answers are not encouraging for analysts. For example, those studying gas separation in the vortex tube may be highly interested in where the regions of highest mixing will occur. A similar computational study using the same turbulence models will almost certainly return four completely different answers.

4.8 Axisymetric Approximation

Many CFD studies also assume that the vortex tube domain may be approximated as axisymetric, such that a 2D model can be used to save computational resources. In these CFD studies, the inlet is modelled as a boundary patch on the outer radius of the tube near the cold exit, and the swirl inside the tube is generated by setting an appreciable circumferential velocity component at the inlet, and the inlet velocity vector forms an angle ϕ with respect to the radial unit vector. Skye et al. [11] have estimated this inlet angle from the geometry of the vortex generator. In this method, a ray in the axial plane is drawn from the midpoint of the nozzle entrance along the nozzle direction, as illustrated in Fig. 4.17a. The intersections of this ray with the tube and the perpendicular radius form a right-angled triangle with the tube center. The injection angle ϕ is adjacent to the side parallel to the ray. Several other researchers [9, 48, 49] appear to have followed the same procedure to find the inlet angle, but the description is not as detailed. Other publications contain no reference for how this angle has been computed. In 3D simulations of the vortex tube, such as those detailed in section 4.6, the solution fields often become axisymetric at roughly $z = L/10$, while the flow close to the inlets exhibits strong circumferential variations. In this section we show two different approximations of the inlet angle ϕ for axisymmetric domains, and analyze the overall accuracy of the axisymmetric assumption by comparing the results to equivalent 3D CFD calculations.

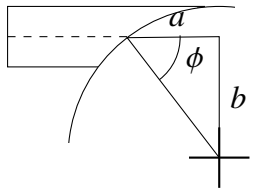

(a) Inlet angle estimation of Skye et al. computes the inlet angle geometrically using the triangle formed from the intersection of a line extending from the midpoint of the channel width along the channel length and a perpendicular radius

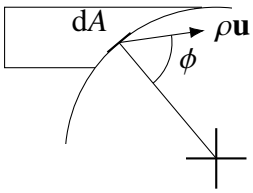

(b) A momentum-based inlet angle estimation uses the results from a converged 3D simulation of the Ranque-Hilsch vortex tube to evaluate equation 4.8 to ensure the resulting inlet angle of the 2D simulation captures the influence of local velocity deviations within the inlet channels.

Figure 4.17: Schematics showing graphically the calculation of the fluid injection angles used for 2D axisymetric CFD simulations of the Ranque-Hilsch vortex tube in this study

As an alternative to Skye et al.'s method for computing the inlet angle, we propose another method for computing the inlet angle to the axisymetric domain. Consider a differential area element $\mathrm{d}A$ on the cylindrical surface defined by $r = D/2$ and $0 < z < N_H$ (c.f. Fig. 4.2). The momentum flux through this element is $\rho\mathbf{u}$ (illustrated in Fig. 4.17b) where ρ is the local fluid density and $\mathbf{u}$ is the local velocity. Using these definitions a momentum-weighted average cosine of the injection angle may be computed using the formula

$$\cos(\phi) = \frac{\int_A \rho\mathbf{u}\cdot\hat{\theta}\,\mathrm{d}A}{\int_A \rho\|\mathbf{u}\|\,\mathrm{d}A} = \frac{\int_A \rho u_\theta\,\mathrm{d}A}{\int_A \rho\|\mathbf{u}\|\,\mathrm{d}A} \tag{4.8}$$

where $\hat{\theta}$ is a unit vector in the circumferential direction. Equation 4.8 may only be computed from the solution fields of a 3D CFD computation which includes the inlet channels (e.g. Model A). Using the method of Skye et al., the injection angle for the VT studied in this work is found to be 61.7°. Processing the results of the M-P-M simulations of models B and C given in section 4.6 using equation 4.8, we compute the momentum-averaged inlet angles to be 69.5° and 68.0°, respectively.

In this section we will compare axisymmetric CFD results using both the momentum-

weighted inlet angle and Skye's inlet angle against results from model A, model B, and a modified version of model A, called a 'Ribbon Inlet', wherein the inlets have been trimmed, and the width of the inlet boundary shown in Fig. 4.18 is computed such that the equivalent circumferential area of the tube occupied by the inlet nozzles at the tube radius in Fig. 4.2 is preserved; yielding a width of 0.686 mm.

The axisymetric domain is shown in Fig. 4.18, and has a wedge angle of 1°. Axisymetric meshes were generated using OpenFOAM's blockMesh tool [35]. A grid convergence study was conducted, and the results are shown in table 4.8. The mesh used for the axisymetric simulations contains 19327 elements, and is depicted in Fig. 4.19. Similar to the previous section, where 3D simulations have been run for comparison, we have used a mesh containing 3026688 elements to produce results capable of resolving the local energy transfers near the inlet of the VT. For each of the following simulations, we have used the M-P-M BC configuration, where the cold exit static pressure boundary condition has been set to the experimentally measured value at the sensor block downstream of the cold exit.

Mesh Label	Cell Count	T_c [K]	T_h [K]
Experiment	-	284.6	312.9
Mesh 1	5220	287.1	316.6
Mesh 2	9352	287.1	316.3
Mesh 3	19327	287.1	316.6
Mesh 4	42566	287.3	316.3

Table 4.8: Grid convergence of CFD calculations of the axisymetric model of the RHVT based on total temperatures measured and computed at the hot and cold exits.

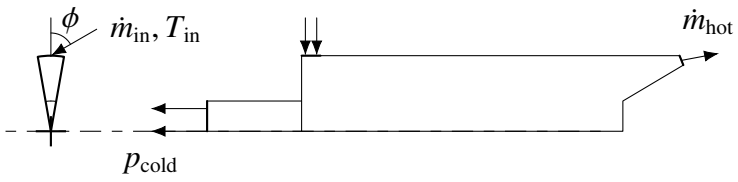

Figure 4.18: An axisymetric model of the Ranque-Hilsch vortex tube used in CFD calculations with a single inlet, cold and hot exits. Periodic boundary conditions are applied on opposite faces of the wedge shown in the left image. Labelled quantities are the boundary conditions applied in the present study

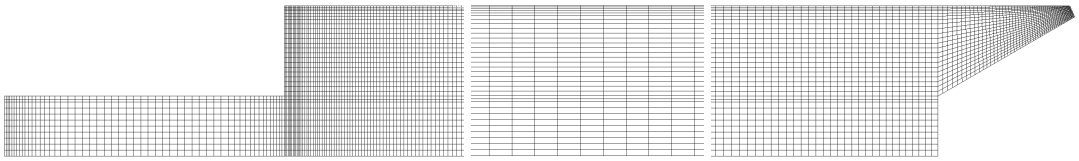

Figure 4.19: Axisymetric mesh of the Ranque-Hilsch vortex tube containing 19327 elements

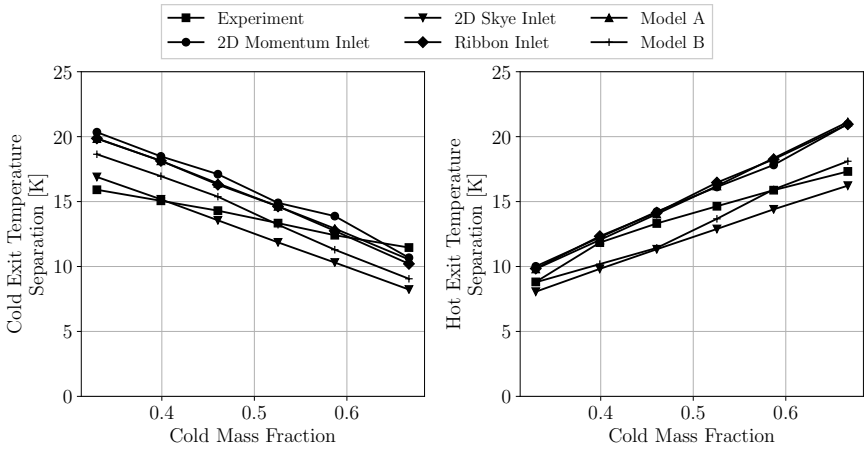

Figure 4.20: Plots showing the variation in cold and hot temperature separation as a function of cold mass fraction of experimental and CFD results obtained from a Ranque-Hilsch vortex tube

Fig. 4.20 plots the total temperature separation at both exits against the cold mass fraction. All of the computational models correctly capture the general trends of the data; increasing the cold mass fraction is accompanied by a decrease in the cold exit temperature separation, and an increase in hot exit temperature separation. While the cold exit temperature separation shows

nearly linear trends, the difference in slope is distinct. This difference could be attributed to any of the discrepancies discussed in section 4.6.2. Notably, the results of models A and B are very similar, confirming that a truncated vortex tube model is likely sufficient for studying energy separation. Furthermore, while no flow reversal has been observed in any of the simulations in this work, it is possible flow reversal could occur when $\lambda < 0.2$, which has not been captured in the experimental data set.

Turning to the axisymetric results, it is clear that simulations using the geometric injection angle definition of Skye et al. under-predict the experimental temperature separation. When contrasted with the results using the momentum-weighted inlet angle, we can conclude that the geometric prediction is too small; when the flow in the nozzles reaches the vortex tube radius, the existing vortex deflects the flow in the nozzles in the circumferential direction, which increases the swirl velocity beyond what would be expected if the flow were to proceed parallel to the nozzle until it had 'fully entered' the domain. The momentum-weighted inlet angle can be considered a viable alternative to the geometric inlet angle.

In addition, the close agreement between the results of the axisymmetric domain using the momentum-weighted inlet angle and the ribbon inlet model suggest that the flow is hydrodynamically stable, or at least that any evolution in the flow field caused by any circumferential disturbances do not substantially impact the energy separation process. Furthermore, the ribbon inlet model and model A predict similar results, indicating that the flow asymmetries in the vicinity of the inlet produced by the nozzles does not affect the overall temperature separation.

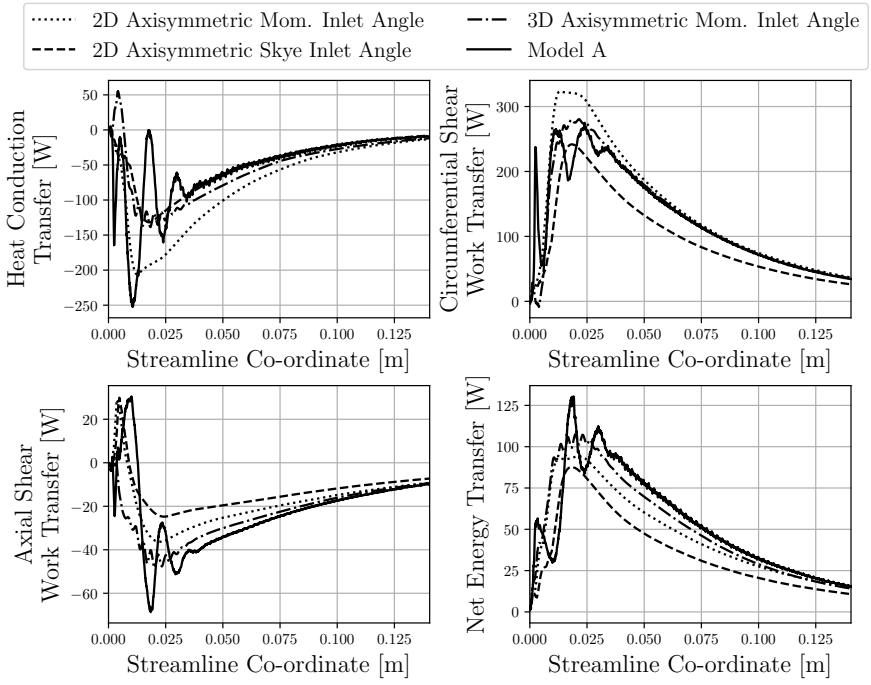

Figure 4.21: Energy transfer to the hot stream along a streamline via different modes in the Ranque-Hilsch vortex tube with a cold mass fraction of 0.5869. The horizontal axis on each plot has been truncated to 45% of the characteristic streamline length to emphasize the variations observed near the inlet. All energy transfers continue to decay towards the hot exit cone.

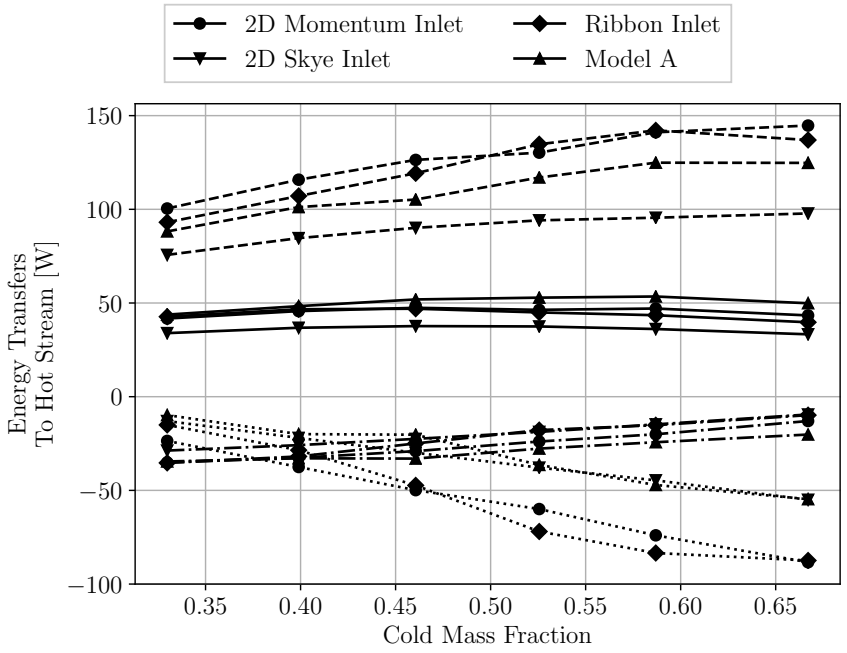

Figure 4.22: Net energy exchanges from each mode of energy transfer have been computed by integrating equations 4.5 - 4.6 along the stagnation streamline. The heat transfer (dotted lines), circumferential shear work transfer (dashed lines), axial shear work transfer (dash-dotted lines), and net energy transfer (solid lines), are plotted as a function of cold mass fraction.

Fig. 4.21 shows the local energy transfers across the stagnation surfaces for a single cold mass fraction, while Fig. 4.22 shows the variation of total energy transfers with cold mass fraction.

In general, the energy transfers across the stagnation streamline reach their largest magnitudes near the inlet, and decay towards the stagnation point on the surface of the hot exit plug. Circumferential work transfer is the dominant energy transfer mode, while heat transfers in the opposite direction, degrading temperature separation. The energy transfers computed in Fig. 4.21 are similar to those found by other researchers who have evaluated energy transfers from axisymmetric solutions [9, 50, 51, 52].

4.9 Summary

In this work, we performed several CFD studies to test the efficacy of various boundary condition assumptions of CFD models of the Ranque-Hilsch vortex tube. The vortex tube domain requires three distinct boundaries: an inlet, a cold exit, and a hot exit. Several combinations of pressure and mass-flow constrained boundary conditions are possible. We have computed CFD simulations using the M-P-M, M-M-P, M-P-P, and P-P-P BC configurations, and found that these configurations predict markedly different temperature separations. Moreover, the M-P-P and P-P-P configurations yielded incorrect predictions of the mass flow split.

In addition to the different combinations of boundary condition combinations, we studied the influence of the exit plenums, which are frequently used in experiments to collect the flow exiting the RHVT, before their properties are measured downstream. We used three vortex tube models: a simple model with nozzle inlets and boundaries which exclude the plenums from the domain, a model which includes the plenums in the CFD domain such that the exit boundary conditions correspond to the physical measurement locations in the experiment, and a model which includes both the exit plenums and an inlet shroud inside the CFD domain. Considering the M-P-M and M-M-P BC configurations, we found that the presence of the exit plenums and inlet shroud has a very minimal impact on temperature separation. When the inlet shroud was excluded, the predicted inlet pressures were 21 kPa to 44 kPa lower than the expected inlet pressures, while simulations including the shroud over-predicted the inlet pressure by about 50 kPa.

Next, we studied the influence of four turbulence models on RHVT flow: k-ε, k-ω, k-ω SST, and SAS SST. The SAS SST model was the most accurate, predicting the cold exit temperature separation within 2 K. While the velocity and temperature fields were largely similar, each turbulence model yielded a unique eddy viscosity distribution, and a different stagnation streamline. Consequently, the local energy transfers across the stagnation streamline take on unique profiles, and the aggregate difference is reflected in the overall temperature separation. It was also noted that the axial position of the stagnation point in the flow correlated negatively with the average eddy viscosity in the domain, suggesting that recirculation regions elongate in response to reduced circumferential shear, thereby providing a larger area for energy to transfer

between the streams, and (at least partially) recovering some energy separation.

Furthermore, we have studied the axisymetric approximation by conducting a series of CFD simulations on axisymetric domains and comparing with 3D simulation and experimental results. We propose a new method to compute the injection angle for a axisymetric VT domains, based on a momentum-weighted average of the flow angle computed from the results of a preliminary 3D simulation. We found that the axisymetric simulations using the momentum-weighted injection angle over-predicted the 3D CFD simulation results for a range of cold mass fractions, while simulations using the injection angle definition proposed by Skye significantly under-predicted temperature separation. We therefore recommend the momentum-weighted computation of the injection angle whenever preliminary CFD results are available.

Finally, we take this opportunity to recognize the progress made in the collective understanding of the RHVT in recent years, afforded by the wide availability of reliable CFD codes, and access to increased computational power. The simulation results presented in this work, alongside many others in the reference list below, were run using widely-available, generic CFD codes with common two-equation (or variant thereof) turbulence models, and standard material properties. In the vast majority of cases, the temperature separations predicted using these methods agree, within reasonable experimental and computational uncertainties, with the observations of comparable experiments. Furthermore, multiple independent CFD studies following the work of Aljuwayhel [9], have accounted for all the mechanisms of energy transfer across the critical stagnation streamsurface, demonstrating that circumferential shear work is the dominant energy transfer mechanism from the cold to hot fluid streams inside the RHVT. Given the robustness of these studies, we claim the dominant energy transfer mechanisms in the RHVT are known, and statements to the contrary, as have been made in recent review papers, are no longer appropriate.

Bibliography

[1] N. Dukhan, M. Cress, and M. R. Cosley, “Cooling and heating system for an equipment enclosure using a vortex tube,” 11 2000.

[2] T. Farouk, B. Farouk, and A. Gutsol, “Simulation of gas species and temperature separa-

tion in the counter-flow Ranque-Hilsch vortex tube using the large eddy simulation technique," *International Journal of Heat and Mass Transfer*, vol. 52, no. 13-14, pp. 3320–3333, 2009.

[3] B. Zhang and X. Guo, "Prospective applications of Ranque–Hilsch vortex tubes to sustainable energy utilization and energy efficiency improvement with energy and mass separation," *Renewable and Sustainable Energy Reviews*, vol. 89, pp. 135–150, 2018.

[4] H. R. Thakare, A. Monde, and A. D. Parekh, "Experimental, computational and optimization studies of temperature separation and flow physics of vortex tube: A review," *Renewable and Sustainable Energy Reviews*, vol. 52, pp. 1043–1071, 2015.

[5] J. Lagrandeur, S. Poncet, and M. Sorin, "Review of predictive models for the design of counterflow vortex tubes working with perfect gas," *International Journal of Thermal Sciences*, vol. 142, no. August 2019, pp. 188–204, 2019.

[6] W. Fröhlingsdorf and H. Unger, "Numerical investigations of the compressible flow and the energy separation in the Ranque-Hilsch vortex tube," *International Journal of Heat and Mass Transfer*, vol. 42, no. 3, pp. 415–422, 1998.

[7] H. H. Bruun, "Experimental Investigation of the Energy Separation in Vortex Tubes," *Journal of Mechanical Engineering Science*, vol. 11, pp. 567–582, 12 1969.

[8] J. J. Keyes Jr, "An experimental study of gas dynamics in high velocity vortex flow," in *Proceedings of the Heat Transfer and Fluid Mechanics Institute.*, pp. 31–46, 1960.

[9] N. F. Aljuwayhel, G. F. Nellis, and S. A. Klein, "Parametric and internal study of the vortex tube using a CFD model," *International Journal of Refrigeration*, vol. 28, no. 3, pp. 442–450, 2005.

[10] R. Shamsoddini and A. H. Nezhad, "Numerical analysis of the effects of nozzles number on the flow and power of cooling of a vortex tube," *International Journal of Refrigeration*, vol. 33, no. 4, pp. 774–782, 2010.

[11] H. M. Skye, G. F. Nellis, and S. A. Klein, "Comparison of CFD analysis to empirical data in a commercial vortex tube," *International Journal of Refrigeration*, vol. 29, no. 1, pp. 71–80, 2006.

[12] H. A. Kandil and S. T. Abdelghany, "Computational investigation of different effects on the performance of the Ranque-Hilsch vortex tube," *Energy*, vol. 84, pp. 207–218, 2015.

[13] S. T. Abdelghany and H. A. Kandil, "Effect of Geometrical Parameters on the Coefficient of Performance of the Ranque-Hilsch Vortex Tube," *Open Access Library Journal*, vol. 05, no. 02, pp. 1–17, 2018.

[14] N. J. Dyck and A. G. Straatman, "Energy Transfer Mechanisms in the Ranque-Hilsch Vortex Tube," in *2018 Canadian Society for Mechanical Engineering (CSME) International Congress*, (Toronto), 2018.

[15] H. R. Thakare and A. D. Parekh, "Experimental investigation & CFD analysis of Ranque—Hilsch vortex tube," *Energy*, vol. 133, pp. 284–298, 2017.

[16] S. E. Rafiee and M. B. M. Sadeghiazad, "Three-dimensional computational prediction of vortex separation phenomenon inside the Ranque-Hilsch vortex tube," *Aviation*, vol. 20, no. 1, pp. 21–31, 2016.

[17] K. Dincer, S. Baskaya, and B. Z. Uysal, "Experimental investigation of the effects of length to diameter ratio and nozzle number on the performance of counter flow Ranque-Hilsch vortex tubes," *Heat and Mass Transfer*, vol. 44, no. 3, pp. 367–373, 2008.

[18] K. Dincer, S. Baskaya, B. Z. Uysal, and I. Ucgul, "Experimental investigation of the performance of a Ranque-Hilsch vortex tube with regard to a plug located at the hot outlet," *International Journal of Refrigeration*, vol. 32, no. 1, pp. 87–94, 2009.

[19] M. Baghdad, A. Ouadha, O. Imine, and Y. Addad, "Numerical study of energy separation in a vortex tube with different RANS models," *International Journal of Thermal Sciences*, vol. 50, pp. 2377–2385, 12 2011.

[20] A. Ouadha, M. Baghdad, and Y. Addad, "Effects of variable thermophysical properties on flow and energy separation in a vortex tube," *International Journal of Refrigeration*, vol. 36, no. 8, pp. 2426–2437, 2013.

[21] M. Baghdad, A. Ouadha, and Y. Addad, "Effects of kinetic energy and conductive solid walls on the flow and energy separation within a vortex tube," *International Journal of Ambient Energy*, pp. 1–17, 11 2018.

[22] B. Zhang, X. Guo, and Z. Yang, "Analysis on the fluid flow in vortex tube with vortex periodical oscillation characteristics," *International Journal of Heat and Mass Transfer*, vol. 103, pp. 1166–1175, 2016.

[23] A. Celik, M. Yilmaz, M. Kaya, and S. Karagoz, "The experimental investigation and thermodynamic analysis of vortex tubes," *Heat and Mass Transfer*, vol. 53, no. 2, pp. 395–405, 2016.

[24] A. Kumar, Vivekanand, and S. Subudhi, "Cooling and dehumidification using vortex tube," *Applied Thermal Engineering*, vol. 122, pp. 181–193, 2017.

[25] V. Kırmacı, "Exergy analysis and performance of a counter flow Ranque-Hilsch vortex tube having various nozzle numbers at different inlet pressures of oxygen and air," *International Journal of Refrigeration*, vol. 32, no. 7, pp. 1626–1633, 2009.

[26] Y. Xue, M. Arjomandi, and R. Kelso, "A critical review of temperature separation in a vortex tube," *Experimental Thermal and Fluid Science*, vol. 46, no. 8, pp. 175–182, 2010.

[27] B. Ahlborn and S. Groves, "Secondary flow in a vortex tube," *Fluid Dynamics Research*, vol. 21, pp. 73–86, 1997.

[28] B. Ahlborn, J. Camire, and J. U. Keller, "Low-pressure vortex tubes," *Journal of Physics D: Applied Physics*, vol. 29, no. 6, pp. 1469–1472, 1999.

[29] A. J. Reynolds, "A note on vortex-tube flows," *Journal of Fluid Mechanics*, vol. 14, pp. 18–20, 9 1962.

[30] R. Hilsch, "The use of the expansion of gases in a centrifugal field as cooling process," *Review of Scientific Instruments*, vol. 18, no. 2, pp. 108–113, 1947.

[31] E. R. G. Eckert and R. M. J. Drake, *Analysis of Heat and Mass Transfer*. McGraw-Hill, 1st ed., 1972.

[32] M. J. Parker and A. G. Straatman, "Experimental Study on the Impact of Pressure Ratio on Temperature Drop in a Ranque-Hilsch Vortex Tube," *In Preparation*, 2020.

[33] ANSYS Inc., "CFX Theory Guide," 2019.

[34] F. Menter and Y. Egorov, "A Scale Adaptive Simulation Model using Two-Equation Models," in *43rd AIAA Aerospace Sciences Meeting and Exhibit*, (Reston, Virigina), American Institute of Aeronautics and Astronautics, 1 2005.

[35] OpenFOAMGroup, "blockMesh," 2000.

[36] ANSYS Inc., "Meshing User's Guide," 2019.

[37] T. Dutta, K. Sinhamahapatra, and S. Bandyopadhyay, "Numerical investigation of gas species and energy separation in the Ranque–Hilsch vortex tube using real gas model," *International Journal of Refrigeration*, vol. 34, pp. 2118–2128, 12 2011.

[38] X. Liu and Z. Liu, "Investigation of the energy separation effect and flow mechanism inside a vortex tube," *Applied Thermal Engineering*, vol. 67, no. 1-2, pp. 494–506, 2014.

[39] T. Dutta, K. P. Sinhamahapatra, and S. S. Bandyopdhyay, "Comparison of different turbulence models in predicting the temperature separation in a Ranque-Hilsch vortex tube," *International Journal of Refrigeration*, vol. 33, no. 4, pp. 783–792, 2010.

[40] P. H. Niknam, H. R. Mortaheb, and B. Mokhtarani, "Numerical investigation of a Ranque–Hilsch vortex tube using a three-equation turbulence model," *Chemical Engineering Communications*, vol. 204, p. 327–336, 2017.

[41] D. K. Walters and D. Cokljat, "A Three-Equation Eddy-Viscosity Model for Reynolds-Averaged Navier–Stokes Simulations of Transitional Flow," *Journal of Fluids Engineering*, vol. 130, 12 2008.

[42] R. Chýlek, L. Šnajdárek, and J. Pospíšil, "Vortex Tube: A Comparison of Experimental and CFD Analysis Featuring Different RANS Models," *MATEC Web of Conferences*, vol. 168, pp. 1–13, 2018.

[43] M. S. Cramer, "Numerical estimates for the bulk viscosity of ideal gases," *Physics of Fluids*, vol. 24, p. 066102, 6 2012.

[44] G. Emanuel, "Bulk viscosity in the Navier–Stokes equations," *International Journal of Engineering Science*, vol. 36, pp. 1313–1323, 9 1998.

[45] Kurosaka M, "Acoustic streaming in swirling flow and the Ranque-Hilsch (vortex-tube) effect," *Journal of Fluid Mechanics*, vol. 124, no. 1982, pp. 139–172, 1982.

[46] V. Bianco, A. Khait, A. Noskov, and V. Alekhin, "A comparison of the application of RSM and LES turbulence models in the numerical simulation of thermal and flow patterns in a double-circuit Ranque-Hilsch vortex tube," *Applied Thermal Engineering*, vol. 106, pp. 1244–1256, 2016.

[47] T. Farouk and B. Farouk, "Large eddy simulations of the flow field and temperature separation in the Ranque-Hilsch vortex tube," *International Journal of Heat and Mass Transfer*, vol. 50, no. 23-24, pp. 4724–4735, 2007.

[48] S. Eiamsa-Ard and P. Promvonge, "Numerical simulation of flow field and temperature separation in a vortex tube," *International Communications in Heat and Mass Transfer*, vol. 35, no. 8, pp. 937–947, 2008.

[49] S. Eiamsa-ard and P. Promvonge, "Review of Ranque-Hilsch effects in vortex tubes," *Renewable and Sustainable Energy Reviews*, vol. 12, no. 7, pp. 1822–1842, 2008.

[50] U. Behera, P. J. Paul, K. Dinesh, and S. Jacob, "Numerical investigations on flow behaviour and energy separation in Ranque-Hilsch vortex tube," *International Journal of Heat and Mass Transfer*, vol. 51, no. 25-26, pp. 6077–6089, 2008.

[51] T. Dutta, K. P. Sinhamahapatra, and S. S. Bandyopadhyay, "CFD Analysis of Energy Separation in Ranque-Hilsch Vortex Tube at Cryogenic Temperature," *Journal of Fluids*, vol. 2013, pp. 1–14, 2013.

[52] R. Shamsoddini and B. Abolpour, "A geometric model for a vortex tube based on numerical analysis to reduce the effect of nozzle number," *International Journal of Refrigeration*, vol. 94, pp. 49–58, 10 2018.

Chapter 5

Summary

The Ranque-Hilsch Vortex Tube (RHVT) has been the subject of intense scientific study since 1947. Despite the large number of papers published covering parametric and analytic studies, the true nature of the temperature separation phenomenon has not been satisfactorily exposed. The works in this thesis collectively represent an effort to understand and model Ranque-Hilsch flow, by generalizing a simplified model of operation, introducing a new solution whose flow structure resembles Ranque-Hilsch flow, and offering some clarification on various Computational Fluid Dynamics (CFD) modelling approximations of the RHVT.

5.1 Summary and Contributions

The contributions in this thesis are spread across three manuscripts.

5.1.1 The Rotating Duct Problem

In chapter 4, the rotating duct studied by Polihronov and Straatman [1] was revisited, with the express intention of generalizing the solution to include the effects of the in-frame radial momentum. This led to a different set of expressions describing the velocity, static temperature, and pressure profiles within the duct, which were shown to be an improvement over the predictions made by Polihronov and Straatman when compared to CFD results over a range of parameters. Next, the analysis was further generalized to include ducts whose cross-sectional

area varied along the duct length, and whose path may be arbitrary. Finally, the choked flow condition was discussed, and it was demonstrated that this condition is a natural generalization of the choked flow condition in stationary ducts. This work includes three novel contributions.

- The generalized results including the influence of the in-plane radial momentum are a clear improvement on the results of Polihronov and Straatman, while still confirming that the general trends in temperature reduction are similar.

- While the analysis of the flow through a straight, constant cross-section duct was found to be largely the same as Lieblein's [2], the generalizations to ducts whose cross-sectional area varies along their length, and whose path can be arbitrary in three dimensions, is new. Importantly, it was demonstrated that the flow speed along the duct path (and consequently the temperature, density, and pressure), are functions of the radius only. This knowledge could simplify the design of turbomachines involving compressible, radial flows.

- Finally, the choked flow limitations in rotating compressible flows are discussed here for the first time. Knowledge of these conditions should also prove useful to designers of turbomachinery.

While these contributions are valuable, the work ultimately contains less convincing arguments for the work transfer theory than those put forward by Allahverdyan and Fauve [3], who showed viscous shear is the dominant energy transfer mechanism in a spiralling, compressible flow. However, the rotating duct analysis (and consequently the extensions of the present work), find purchase in describing of a new device, described in section 5.2.1.

5.1.2 Exact Solutions of the Navier-Stokes Equations

In chapter 3, the original method for finding exact solutions to the Navier-Stokes equations presented by Wang [4] has been extended to find solutions in three dimensions. New solutions include 3D generalizations of well known Navier-Stokes solutions including Kovasznay flow [5], as well as new generalizations of the Burger's vortex, and a novel swirling flow solution.

5.1.3 Numerical Analysis of the RHVT

In chapter 4, three CFD studies were carried out with the intention of assessing common assumptions about RHVT which are often implicit in other computational studies in the literature.

First, the influences of different boundary locations were tested. Three different models were used in the computations: one model where the hot and cold boundaries are placed at the 'immediate' exits and the inlet nozzles are the entrance of the domain, a second model where the CFD domain includes the downstream hot and cold plenums, and a third model where both the plenums and the inlet shroud upstream of the vortex generator are included. In addition, different combinations of mass, and pressure boundary conditions were tested at different exits. It was found that temperature separation changes significantly with different boundary conditions, and that boundary condition configurations which have a fixed inlet mass flow are the most reliable. Furthermore, the influence of the shroud is not relevant when the inlet mass flow is fixed, as only the upstream pressure is changed as a result.

Next, the influence of different turbulence models was tested. The SAS SST model produced the most accurate results. Curiously, the eddy viscosity distributions were markedly different across turbulence models, with the k-ε containing the highest values, and the SAS SST containing the lowest. While the flow structure remained similar across the turbulence models, the position of the stagnation point changed substantially, with the k-ε model containing the shortest stagnation streamlines, while the stagnation streamlines in the SAS SST model extended all the way to the hot exit cone.

Finally, the influence of the axisymmetric approximation was studied by comparing axisymmmetric CFD results to 3D CFD results. A new momentum-based method for computing the required injection angle for axisymmetric computations was proposed. It was found that the axisymmetric approximation is adequate for predicting temperature separation, and that the momentum-based method of determining the injection angle is comparable to the original geometric method.

This manuscript contains many small discoveries to improve computational modelling of the RHVT:

- The truncated VT model where with boundaries at the 'immediate exits' and inlet nozzles

shown in figure 1.1 has been validated, and the mass flow inlet, with a single mass flow outlet boundary condition fixed is recommended to fix the resulting cold mass fraction.

- The influence of turbulence model on the internal flow structure has been revealed, and a trend showing longer stagnation streamlines correlating with smaller eddy viscosities has been documented for the first time, suggesting a natural lengthening of the recirculation region to accomodate energy transfer in these cases.

- A new method for computing the injection inlet angle is proposed and shown to be comparable to the earlier geometric method when 3D CFD results are available.

- Analyzing the energy transfer modes in many of these cases has shown again that circumferential shear work transfer is the dominant energy transfer mechanism in the RHVT.

5.2 Future Work

5.2.1 The Rotating Duct Problem

Polihronov and Straatman [1] originally studied the model of compressible fluid moving through a rotating duct to provide an analogue to the work transfer mechanism in the RHVT. During their initial investigation, however, it became clear that the example studied could provide a more efficient means of cooling than the RHVT. The advantage is clear; while the energy transferred via circumferential shear work in the RHVT ultimately increases the temperature of the hot stream, the fluid in the rotating duct transfers its energy to the walls of the duct, working to increase or maintain the angular momentum of the system. In reality, a rotating duct with a pressure tank affixed to the outer radius would be imbalanced, and the process would be transient as the cooling would decay as the pressure tank discharges. A much better design has been conceived by Polihronov and Straatman [6], wherein a circular shroud around the edge of a spinning disk is charged with supply air. The air moves down radial holes in the disc (spaced evenly around the circumference to balance the device naturally), and exhausts at the axis. The energy transferred to the disk is either sapped by parasitic forces, or can be harnessed for useful work such as aiding the compression of the upstream flow. This device

was invented very recently and there many potential applications to explore, including coolers for electrical cabinets, snow making, and even power generation.

5.2.2 Exact Solutions of the Navier-Stokes Equations

An obvious starting point for future work is the final analytical solution developed in chapter 3. The streamlines bear a strong resemblance to the Ranque-Hilsch flow seen in chapter 1, and the streamfunction has other valuable properties which are not present together in any other known solution:

- the flow field is fully 3D in cylindrical coordinates,
- it captures the axial stagnation point,
- viscosity effects are included,
- and it is continuous everywhere and there are no divisions between different flow regions.

While these flow characteristics are desirable, there are still some shortcomings which need to be addressed before it can be applied to predict temperature separation:

- The flow field is incompressible; as discussed in chapter 1, compressibility is a necessary condition for cooling in the RHVT. Linderstrøm-Lang [7] noted that the omission of density changes does not introduce significant errors in flow structure of an inherently compressible flow. Maicke et al. [8] arrived at a similar conclusion in their study of swirling, recirculating flows. So while the solution flow structure may be a fair approximation of Ranque-Hilsch flows, the volume dilation term, $\boldsymbol{\nabla} \cdot \mathbf{u}$, is still 0, and another approximation is necessary to include the influence of compressiblity in the energy equation (c.f. equation 1.14).
- There is little control over the boundary conditions; the solution only contains 2 free parameters, which may not be enough to characterize the range of parameters influencing Ranque-Hilsch flow. There is little hope in finding a solution which captures the complex variations produced by the asymmetry of the inlet nozzles. Lewellen [9] argued such

swirling flows would always have trouble matching boundary conditions to realistic flow problems.

- Like the simplified flow structure models developed by other researchers, the solution is derived assuming a constant viscosity. Thus, the best approximation to be made is to assign an equivalent turbulent eddy viscosity to the entire domain. This appears problematic considering the wild variations in eddy viscosity observed in section 4.7. On the other hand, Fröhlingsdorf and Unger [10] obtained surprisingly good agreement with the internal flow measurements of Bruun [11] using a constant viscosity in their numerical simulations, so there could be scenarios where this approach is viable.

Beyond applications to the RHVT, there is potential to extract additional interesting solutions:

- In this work only steady solutions were considered. The extension to unsteady flows should be straightforward, and will yield interesting results.
- Other co-ordinate systems, including spherical, toroidal, and prolate spheroidal co-ordinate systems have not been thoroughly explored for solutions and may yield solutions which describe physically interesting flows.
- Kerr and Dold [12] analyzed a multi-cellular stagnation point flow in cartesian co-ordinates using a method similar to Wang's [4]. It may be possible to adapt the present technique to obtain solutions similar to Kerr and Dold's in cylindrical or spherical co-ordinate systems using a variation of the present technique. Such a solution may help to describe the axisymmetric vortex breakdown phenomenon.

5.2.3 Numerical Analysis of the RHVT

One key area where numerical studies will prove useful is in the investigation of Behera et al.'s claim [13]; suggesting that energy separation is maximized when the tube is just long enough to contain the stagnation point. It seems natural that energy separation would remain constant if the length of the tube is extended past the naturally occuring location of the stagnation point, but this needs to be validated numerically, and (ideally) experimentally.

A well-thought-out direct numerical simulation of the full RHVT would certainly provide valuable insight into the energy separation mechanisms at play. Aside from the organizational and monetary barriers associated with conducting such a simulation, the core problem is in the ability to accurately estimate the size of the smallest eddys *a priori* such that the grid may be appropriately sized. While a sound understanding of the turbulence in compressible flows will certainly help, the process may still be iterative, and other problems may arise from the storage and processing of such a large amount of data.

Bibliography

[1] J. G. Polihronov and A. G. Straatman, "Thermodynamics of Angular Propulsion in Fluids," *Physical Review Letters*, vol. 109, p. 54504, 8 2012.

[2] S. Lieblein, "Theoretical and experimental analysis of one-dimensional compressible flow in a rotating radial-inlet impeller channel," Tech. Rep. October, 1952.

[3] A. E. Allahverdyan and S. Fauve, "Modeling gasodynamic vortex cooling," *Physical Review Fluids*, vol. 2, p. 084102, 8 2017.

[4] C.-Y. Wang, "On a Class of Exact Solutions of the Navier-Stokes Equations," *Journal of Applied Mechanics*, vol. 33, pp. 696–698, 9 1966.

[5] L. I. G. Kovasznay, "Laminar flow behind a two-dimensional grid," *Proc. Camb. Phil. Soc.*, vol. 44, no. May, pp. 58–62, 1948.

[6] J. Polihronov and A. G. Straatman, "Mechanism for enhanced energy extraction and cooling pressurized gas," 2013.

[7] C. U. Linderstrøm-Lang, "The three-dimensional distributions of tangential velocity and total-temperature in vortex tubes," *Journal of Fluid Mechanics*, vol. 45, no. 1, pp. 161–187, 1971.

[8] B. A. Maicke, O. M. Cecil, and J. Majdalani, "On the compressible bidirectional vortex in

a cyclonically driven Trkalian flow field," *Journal of Fluid Mechanics*, vol. 823, pp. 755–786, 2017.

[9] W. S. Lewellen, "A solution for three-dimensional vortex flows with strong circulation," *Journal of Fluid Mechanics*, vol. 14, no. 3, pp. 420–432, 1962.

[10] W. Fröhlingsdorf and H. Unger, "Numerical investigations of the compressible flow and the energy separation in the Ranque-Hilsch vortex tube," *International Journal of Heat and Mass Transfer*, vol. 42, no. 3, pp. 415–422, 1998.

[11] H. H. Bruun, "Experimental Investigation of the Energy Separation in Vortex Tubes," *Journal of Mechanical Engineering Science*, vol. 11, pp. 567–582, 12 1969.

[12] O. S. Kerr and J. W. Dold, "Periodic steady vortices in a stagnation-point flow," *Journal of Fluid Mechanics*, vol. 276, pp. 307–325, 10 1994.

[13] U. Behera, P. J. Paul, S. Kasthurirengan, R. Karunanithi, S. N. Ram, K. Dinesh, and S. Jacob, "CFD analysis and experimental investigations towards optimizing the parameters of Ranque-Hilsch vortex tube," *International Journal of Heat and Mass Transfer*, vol. 48, no. 10, pp. 1961–1973, 2005.

Nolan J. Dyck

Education

2015-2020 **Doctor of Philosophy**
Western University
Thesis: Temperature Separation Mechanisms in the Ranque-Hilsch Vortex Tube

2012-2014 **Master of Engineering Science**
Western University
Thesis: Digital Generation and Radiation in Spherical-Void-Phase Porous Media
http://ir.lib.uwo.ca/etd/2506

2007-2012 **Bachelor of Applied Science, Honours Mechanical Engineering**
University of Waterloo

Research Experience

2015- **Research Assistant**
Western University

- Investigated temperature separation mechanisms in the Ranque-Hilsch vortex tube (RHVT), focusing on the impact of shear work transfer
- Simulated flow inside the RHVT using commercial computational fluid dynamics software ANSYS CFX, focusing on the importance of accurate boundary condition modelling
- Worked alongside a Master's student conducting experiments on the RHVT to accurately match computational fluid dynamics simulation results to experimental results
- Developed an extended solution technique for the Navier-Stokes equations, and applied the technique to find an exact solution describing a 3D swirling flow similar to Ranque-Hilsch flow

2012-2014 **Research Assistant**
Western University

- Developed a new procedure using discrete element modelling software YADE to model physically realistic representations of spherical-void-phase porous media
- Used the digital porous media samples in computational fluid dynamics simulations to find transport properties including permeability and interfacial heat transfer coefficients
- Implemented a Monte-Carlo radiative heat transfer model into a FORTRAN conjugate computational fluid dynamics code capable of solving multi-physics problems involving fluid flow as well as convection, conduction and radiation heat transfer in domains involving fluid, porous, and solid regions

Peer-Reviewed Publications

N. J. Dyck, M. J. Parker, and A. G. Straatman, "The Impact of Boundary Condition and Model Parameters on CFD Simulations of the Ranque-Hilsch Vortex Tube," *International Journal of Heat and Mass Transfer*, Revised. Submission No. HMT-S-20-01797

N. J. Dyck and A. G. Straatman, "Exact Solutions to the Three-Dimensional Navier–Stokes Equations Using the Extended Beltrami Method," *Journal of Applied Mechanics*, vol. 87, no. 1, 2020. DOI: 10.1115/1.4044927

N. J. Dyck and A. G. Straatman, "Compressible and Choked Flows in Rotating Passages," *Open Journal of Fluid Dynamics*, vol. 09, no. 01, pp. 1–21, 2019. DOI: 10.4236/ojfd.2019.91001

M. Elhalwagy, N. Dyck, and A. G. Straatman, "A Multi-Level Approach for Simulation of Storage and Respiration of Produce," *Applied Sciences*, vol. 9, no. 6, pp. 1–20, 2019. DOI: 10.3390/app9061052

N. J. Dyck and A. G. Straatman, "Radiative property characterization of spherical void phase graphitic foam," *International Journal of Heat and Mass Transfer*, vol. 92, pp. 1201–1204, 2016. DOI: 10.1016/j.ijheatmasstransfer.2015.09.065

N. J. Dyck and A. G. Straatman, "A new approach to digital generation of spherical void phase porous media microstructures," *International Journal of Heat and Mass Transfer*, vol. 81, pp. 470–477, 2015. DOI: 10.1016/j.ijheatmasstransfer.2014.10.017

Conference Articles and Abstracts

(Abstract, Presented) N. Dyck and A. Straatman, "An extension to the extended Beltrami solution method and solutions to the 3D Navier-Stokes equations," in *Bulletin of the American Physical Society*, (Seattle), American Physical Society, 2019

(Abstract, Presented) N. J. Dyck and A. G. Straatman, "An Exact Solution to the 3D Navier-Stokes and Applications to the Ranque-Hilsch Vortex Tube," in *Proceedings of The Joint Canadian Society for Mechanical Engineering and CFD Society of Canada International Congress 2019*, (London), 2019

(Article, Presented) N. J. Dyck and A. G. Straatman, "Energy Transfer Mechanisms in the Ranque-Hilsch Vortex Tube," in *2018 Canadian Society for Mechanical Engineering (CSME) International Congress*, (Toronto), 2018

(Article, Presented) N. J. Dyck and A. G. Straatman, "Rotating compressible flow in a straight duct," in *The 25th Annual Conference of the CFD Society of Canada*, (Windsor), 2017

(Article) A. G. Straatman, A. Kalopsis, and N. J. Dyck, "Generation of simple extended porous surface expression from results of pore-level conjugate heat transfer in spherical-void-phase porous blocks," in *The Sixth International Conference on Porous Media and Its Applications in Science, Engineering and Industry*, (Waikoloa), 2016

(Article, Presented) N. J. Dyck and A. G. Straatman, "A New Approach to Digital Generation of Porous Media Microstructures," in *The 22nd Annual Conference of the CFD Society of Canada*, (Toronto), 2014

Awards

2017-2019 **PGS D Scholarship**
Natural Sciences and Engineering Research Council (NSERC)
Competitive national scholarship awarded based on research ability
Award value over 2 years: $42000 CAD

2018 **Graduate Student Teaching Assistant Award**
Western University Society of Graduate Students
University-wide competition; awarded based on written nominations from nine students for effective instruction in *Thermodynamics I*
Award value: $500 CAD

2016-2017 **Ontario Graduate Scholarship**
The Government of Ontario and Western University
Competitive provincial scholarship awarded based on research potential
Award value over 1 year: $15000 CAD

2013-2014 **Ontario Graduate Scholarship**
The Government of Ontario and Western University
Competitive provincial scholarship awarded based on research potential
Award value over 1 year: $15000 CAD

Teaching Experience

2012-2018 **Lead Teaching Assistant - Thermodynamics I**
Western University
Occasional lecturing, lead tutorials, distributed workload between five TAs, devised grading schemes for assignments, handled grading disputes, supervised laboratory sessions, graded assignments and tests.

2016-2019 **Teaching Assistant - Internal Combustion Engines**
Western University
Supervised laboratory sessions, graded assignments and tests.

2013-2014 **Lead Teaching Assistant - Finite Element Methods**
Western University
Distributed workload between five TAs, devised grading schemes for assignments, handled grading disputes, supervised laboratory sessions, graded assignments and tests.